UNIVERSITÀ
DEGLI STUDI
FIRENZE

DOTTORATO DI RICERCA IN SCIENZE BIOMEDICHE

CICLO XXXVIII

COORDINATORE Prof Fabrizio Chiti

Tesi di dottorato

Linking the impact of mutations of the Extracellular Domain of Myelin Protein Zero to the etiopathogenesis of Charcot-Marie-Tooth disease

Settore Scientifico Disciplinare BIOS-07/A

Dottorando
Dott. Teresa Grande

Supervisore
Prof. Francesco Bemporad
Co-supervisori
Prof. Fabrizio Chiti
Prof.ssa Roberta Cascella

Anno accademico 2025-2026

INDEX

Abstract

Myelin Protein Zero (MPZ) is the primary adhesive protein of the peripheral nervous system (PNS) myelin sheath, where its extracellular domain (MPZex) mediates homophilic interactions essential for compacting myelin lamellae. Mutations in the MPZ gene are a leading cause of Charcot-Marie-Tooth (CMT) disease, the most common inherited neuropathy, but give rise to a remarkably heterogeneous spectrum of clinical phenotypes, from severe, early-onset demyelinating forms (CMT1B, DSS) to milder, late-onset axonal variants (CMT2I/J). This diversity is thought to reflect distinct molecular pathomechanisms, yet a quantitative framework directly linking the biophysical defects of a given mutation to its clinical outcome has been lacking. The primary objective of this thesis is to establish such a framework by systematically investigating the molecular consequences of pathogenic point mutations in MPZex, thereby decoding the complex genotype-phenotype correlations in MPZ-related neuropathies.

The first part of this thesis provides a comprehensive biophysical characterization of the novel D134V mutation, identified in a patient with severe, childhood-onset CMT1B. Using a suite of spectroscopic, stability, and functional assays, we demonstrate that the D134V mutant, while retaining a globally folded β-sheet architecture, exhibits significant local conformational perturbations and appears markedly destabilized against thermal and acidic stress. This structural fragility predisposes the mutant to aggregation and translates into a failure of its biological function, with fluorescence-based assays revealing a dramatic (~80%) reduction in homophilic (MPZ-MPZ) binding affinity. This combination of structural instability, aggregation propensity, and severe loss of adhesive function could provide a direct molecular explanation for the severe demyelinating phenotype.

The investigation was then expanded to a comparative analysis of a broader panel of eight pathogenic MPZex variants associated with a wide range of clinical severities. This analysis revealed that each mutation imparts a unique biophysical signature creating a spectrum of molecular defects in stability and aggregation kinetics. The homophilic adhesion assay proved to be a powerful functional

discriminator, revealing a clear dichotomy: one group of mutants displayed a severe impairment of self-association, whereas a second group retained near-wild-type binding capacity. These findings reveal a possible correlation, demonstrating that variants causing a profound loss of homophilic adhesion are predominantly associated with severe, early-onset demyelinating phenotypes, thus suggesting that the direct failure of myelin compaction is a primary driver of the most severe forms of the disease.

Finally, the complex, multi-parameter dataset was integrated using Principal Component Analysis (PCA) to establish a quantitative, structure-based framework for decoding MPZ neuropathies. The PCA clustered the variants into distinct groups based on their integrated biophysical signatures, creating a "pathogenic landscape" where each mutant's position reflects its molecular defect profile and strongly correlates with its clinical outcome. Variants associated with severe, early-onset demyelinating phenotypes localized extreme positions in this landscape, reflecting profound instability and a catastrophic loss of adhesive function. Conversely, variants linked to milder, late-onset axonal neuropathies were located closer to the wild-type, consistent with more subtle defects. This work, therefore, establishes a robust framework that not only elucidates the molecular principles governing the clinical heterogeneity of MPZ-related neuropathies but also holds promise for predicting the severity of newly identified variants and for informing the development of tailored, mechanism-based therapeutic strategies for CMT.

Abbreviations

ATF4, Activating transcription factor 4; ATF6, Activating transcription factor 6; CD, Circular dichroism; CHN, Congenital Hypomyelinating Neuropathy; CHOP, C/EBP homologous protein; CMAP, Compound muscle action potential; CMT, Charcot–Marie–Tooth disease; CMT1B, Demyelinating CMT type 1B; CMT2I, Axonal CMT type 2I; CMT2J, Axonal CMT type 2J; CNS, Central nervous system; COM, Center of mass; CSP, chemical shift perturbations; DLS, Dynamic light scattering; DSF, Differential scanning fluorimetry; ER, Endoplasmic reticulum; ERAD, Endoplasmic reticulum-associated degradation; FTIR, Fourier transform infrared; GJB1, Gap junction beta-1 (connexin 32); GndHCl, Guanidine hydrochloride; HSQC, Heteronuclear single-quantum correlation; IBs, Inclusion bodies; IEX, Ion-exchange chromatography; Ig, Immunoglobulin; IgCAM, Immunoglobulin cell adhesion molecule; IMAC, Immobilized metal affinity chromatography; IPL, Intraperiod line; IPTG, Isopropyl β-D-1-thiogalactopyranoside; IRE1, Inositol-requiring enzyme 1; K_{sv}, Stern–Volmer constant; LS, Light Scattering; MAG, Myelin-associated glycoprotein; MBP, Myelin basic protein; MDL, Major dense line; MFN2, Mitofusin 2; MPZ, Myelin protein zero; NaCl, Sodium chloride; NCVs, median nerve conduction velocities; Ni-NTA, Nickel–nitrilotriacetic acid; NMR, Nuclear magnetic resonance; NRG1-III, Neuregulin 1 type III; NTA, Nitrilotriacetic acid; P2, Peripheral myelin protein 2 (FABP8); PBS, Phosphate-buffered saline; PERK, PKR-like ER kinase; PKC, Protein kinase C; PMP22, Peripheral myelin protein 22; PMP22ex; Second extracellular domain of PMP22; PNS, Peripheral nervous system; PRX, Periaxin; RACK1, Receptor for activated C kinase 1; SCs, Schwann cells; SEC-MALS, Size exclusion chromatography - multi-angle light scattering; SLIs, Schmidt–Lanterman incisures; TM, Transmembrane; Tris-HCl, Tris(hydroxymethyl)aminomethane hydrochloride; UPR, Unfolded protein response; XBP1, X-box binding protein 1

1. Introduction

1.1 The Peripheral Nervous System (PNS)

The nervous system of vertebrates is divided into two parts: the central nervous system (CNS), which comprises the brain and spinal cord, and the PNS, which encompasses cranial nerves, spinal nerves, and autonomic nerve plexuses.

The PNS sends sensory information from areas outside the body to the CNS and transmits motor commands from the CNS to various organs, such as muscles and glands. The PNS is divided into the somatic and autonomic nervous domains. The somatic system comprises the sensory system, which controls sensory perception and provides information about the surrounding environment[1], and the motor system, which controls voluntary and involuntary movements[2]. The autonomic nervous system regulates involuntary processes and comprises sympathetic, parasympathetic, and enteric nervous systems.

The sympathetic and parasympathetic divisions are often described as the 'fight or flight' and 'rest and relax' systems, respectively activating in stressful and calm situations[3] (Figure 1).

The enteric division is a complex nervous system that is intrinsic to the gastrointestinal tract. It is able to operate independently, which is why it is often referred to as the second brain[4].

Structurally, peripheral nerves are bundles of axons ensheathed by connective tissue layers (endoneurium, perineurium, epineurium) and associated glia. Schwann cells and other support cells provide trophic support and enable conduction.

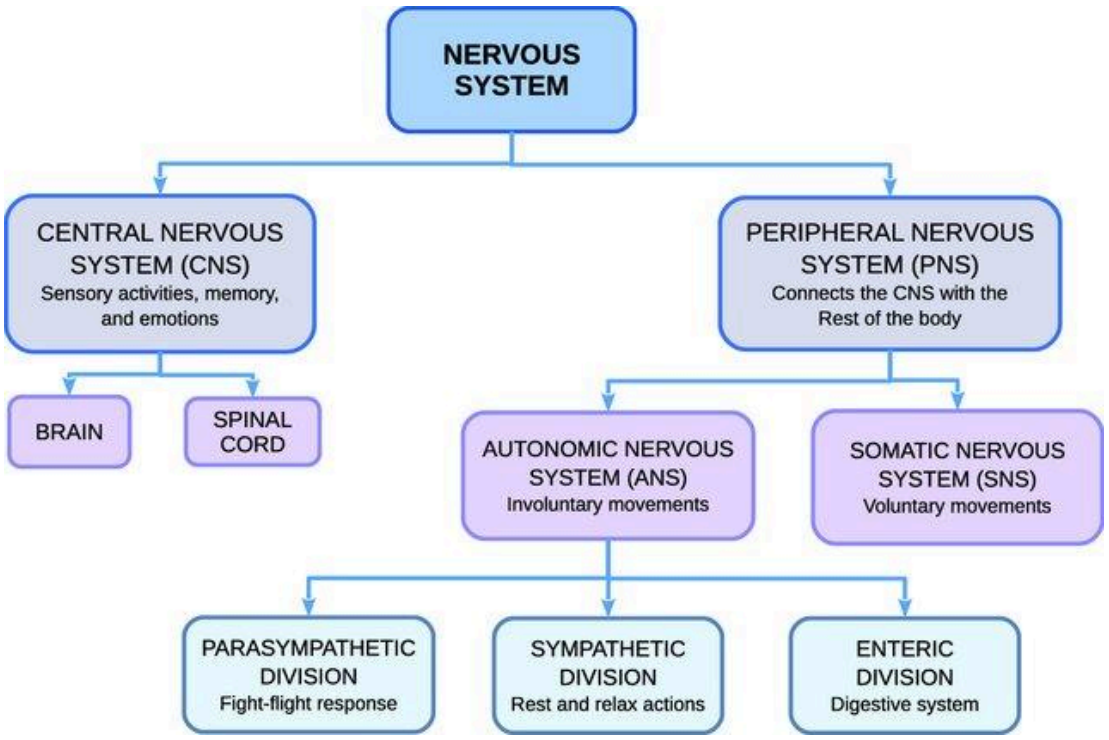

Figure 1. Overview of the vertebrate nervous system[5] .

1.1.1 Anatomy and Physiology of the PNS

Peripheral nerves arise as dorsal and ventral roots from the spinal cord and as cranial nerves from the brainstem. The PNS includes 12 pairs of cranial nerves and 31 pairs of spinal nerves, each containing motor and sensory fibers. Somatic sensory neuron cell bodies lie in dorsal root ganglia (or cranial sensory ganglia) outside the CNS. In contrast, motor neuron cell bodies reside in the CNS (ventral horn), but their axons travel peripherally in nerves[6]. Autonomic fibers form synapses in peripheral ganglia: in particular, sympathetic preganglionic fibers from the thoracolumbar spinal cord synapse in sympathetic chain ganglia or prevertebral ganglia, while parasympathetic preganglionic fibers from the brainstem or sacral cord synapse in terminal ganglia. Enteric neurons (derived from neural crest) form extensive networks within the gut wall. Thus, the PNS provides both afferent (sensory) and efferent (motor/autonomic) pathways that link the CNS with muscles, glands, and sensory organs.

Physiologically, PNS fibers transmit electrical signals via action potentials along with axons. Myelinated axons conduct impulses rapidly by saltatory conduction, while unmyelinated fibers conduct more slowly. This rapid conduction is due to

the insulating myelin sheath and nodal anatomy, which allow the depolarization to "jump" between nodes of Ranvier[7]. Functionally, the PNS exerts its function through two primary pathways. The sensory (afferent) pathway transmits information from a vast array of peripheral receptors—including mechanoreceptors for touch and pressure, nociceptors for pain, and thermoreceptors for temperature—towards the CNS. The motor (efferent) pathway carries instructional signals away from the CNS to peripheral effector organs, initiating skeletal muscle contraction (somatic) or modulating the activity of smooth muscle, cardiac muscle, and glands (autonomic). The PNS also influences development and plasticity in peripheral tissues, and PNS glia interact with immune cells and extracellular matrix to maintain tissue homeostasis[6,8].

1.1.2 Neurons and Glial Cells

The PNS contains two principal cell types: neurons, the electrically excitable cells specialized for signal transmission, and glial cells, which provide fullsupport and protection. Peripheral neurons vary widely in morphology and function. Recent single-cell transcriptomic studies have revealed even greater heterogeneity among peripheral neurons, including novel subtypes in sensory and autonomic ganglia, which reflects the complex tasks of the PNS[9].

Somatic sensory neurons are typically pseudounipolar, with a single axon that bifurcates into peripheral and central branches; their cell bodies are located in the dorsal root ganglia or cranial ganglia. Somatic motor neurons (lower motor neurons) are multipolar, with cell bodies in the ventral horn of the spinal cord or motor nuclei of the brainstem and axons projecting into peripheral nerves to innervate skeletal muscle. Autonomic neurons include preganglionic cells (in the CNS) and postganglionic multipolar neurons (in peripheral sympathetic or parasympathetic ganglia) that innervate smooth muscle, cardiac muscle, and glands. Enteric neurons form two plexuses in the gut wall and have diverse phenotypes specialized for local control of motility and secretion.

In the PNS, the principal glial cells are Schwann cells (SCs), which serve multiple roles and have two distinct phenotypes[8]: Remak cells encircle multiple axons of <1 μm diameter, while myelinating Schwann cells wrap larger axons in many

membrane turns. Both types support axons metabolically and physically, but only myelinating Schwann cells produce the high-resistance insulation required for saltatory conduction[8].

Myelinating Schwann cells associate in a 1:1 relationship with a single, large-caliber axon (typically >1 μm in diameter) and wrap it in a thick, lipid-rich myelin sheath. This is fundamental for the rapid, saltatory conduction required for time-sensitive signals, such as motor commands to muscles and proprioceptive feedback from joints.

Non-myelinating Schwann cells employ a resource-efficient strategy designed for maintenance and support rather than speed. A single Remak cell associates with multiple small-caliber axons (typically <1 μm in diameter), enveloping them in individual troughs within its cytoplasm. This composite structure, comprising one Remak cell and its cohort of ensheathed axons, is termed a Remak bundle. This arrangement provides crucial metabolic support to the small axons. It electrically insulates them from one another, preventing signal crosstalk between adjacent fibers that convey slow-conducting information, such as pain, temperature, and autonomic signals.

In addition to Schwann cells, other peripheral glia include satellite glial cells and enteric glia. Satellite glia form a tight capsule around neuronal cell bodies in sensory and autonomic ganglia[6]. They regulate the microenvironment of neuronal somata, providing metabolic support, buffering ions and neurotransmitters, and mediating responses to injury. Enteric glia in the gut wall have roles analogous to astrocytes, maintaining the function of enteric neurons.

1.1.3 Myelin formation in the PNS

The formation and development of myelin sheaths in the nervous system is referred to as myelination, or myelinogenesis. Indeed, the myelin sheath is a highly specialized, multilamellar extension of the glial plasma membrane that wraps around axons, providing electrical insulation and significantly enhancing the speed and efficiency of nerve impulse conduction. In vertebrates, myelin evolved approximately 500 million years ago as an energy-efficient strategy to increase conduction velocity without proportionally enlarging axonal diameter, a

crucial step in the evolution of complex motor and sensory systems[10,11]. In the PNS, myelin is produced exclusively by Schwann cells, which ensheathe large-diameter axons in a 1:1 relationship. Each Schwann cell forms a single internodal segment, wrapping its membrane concentrically around the axon to form a compact sheath composed of dozens of tightly apposed membrane layers [12,13]. Between adjacent internodes lie short, unmyelinated gaps known as nodes of Ranvier, approximately one micrometer in length, which contain dense clusters of voltage-gated sodium and potassium channels. These nodes, together with the myelinated internodes, form the structural basis for saltatory conduction, where action potentials "jump" from node to node, allowing impulses to propagate at velocities up to 150 m/s—compared to only 0.5–10 m/s in unmyelinated fibers [11,14].

During development, immature Schwann cells derived from the neural crest undergo a sequence of differentiation events tightly regulated by reciprocal axon–glial signalling. One of the most crucial processes, known as radial sorting, enables these cells to segregate large-caliber axons (>1 μm) destined for myelination from smaller ones that remain unmyelinated within Remak bundles, where non-myelinating Schwann cells provide trophic and metabolic support[15,16]. The axon itself provides instructive cues that control the initiation and extent of myelination, most notably via Neuregulin-1 type III (NRG1-III), a transmembrane signaling protein acting as a molecular rheostat. The surface density of NRG1-III on axons dictates Schwann cell differentiation, the establishment of the 1:1 relationship, and ultimately the thickness of the myelin sheath. Once this signaling threshold is reached, the Schwann cell extends and wraps its membrane around the axon in a spiraling fashion, gradually extruding cytoplasm to form a compact, multilamellar structure with specialized domains. The resulting architecture, which accounts for roughly 70–85% lipid by dry weight, provides both electrical insulation and structural stability[12].

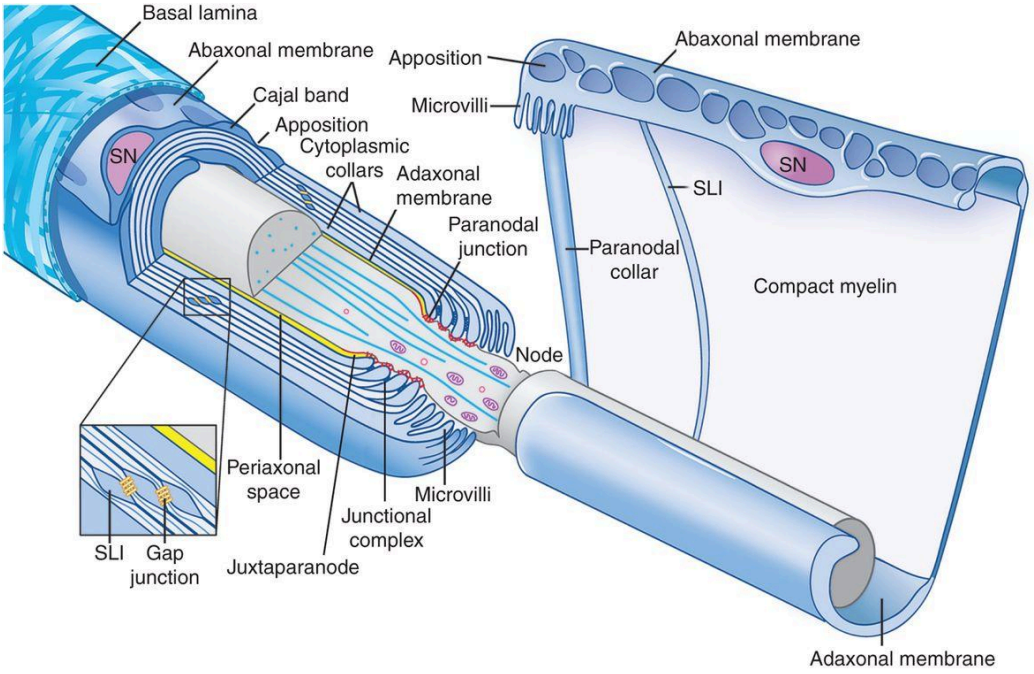

Figure 2. Schematic representation of myelinating Schwann cells wrapped around an axon. The left panel shows a longitudinal cross-section of a Schwann cell forming successive wraps of myelin around the axon, with basal lamina and abaxonal membrane; the right panel shows the unwrapped form of the same Schwann cell, illustrating internal compartments such as Cajal bands, appositions, paranodal loops, SLI, and the periaxonal space. Figure adapted from[17]

Compact myelin is not homogeneous; instead, it contains specialized cytoplasmic compartments that maintain the metabolic and structural integrity of the sheath. Schmidt–Lanterman incisures (SLIs) form radial cytoplasmic channels across the compact layers, allowing communication between the adaxonal and abaxonal cytoplasm[12]. The abaxonal collar—the outermost cytoplasmic region of the Schwann cell containing the nucleus—is organized into longitudinal Cajal bands, which facilitate intracellular transport of nutrients and vesicles along the internode[18] (figure 2). Experimental disruption of Cajal bands leads to impaired Schwann cell elongation and decreased conduction velocity, underscoring their importance in maintaining internodal integrity and electrical performance[17,19]. At both ends of each myelin segment, Schwann cell microvilli project toward the axolemma, anchoring the myelin sheath and contributing to the formation of heminodes, which subsequently mature into fully functional nodes of Ranvier[20]. Furthermore, the entire Schwann cell and its myelin sheath are encased in a basal lamina, a specialized extracellular matrix that supports cell adhesion, guides

axonal growth, and contributes to myelin maintenance through integrin and dystroglycan signaling[18,21].

Myelination in the PNS differs from that in the CNS in both structural and functional aspects. While a single oligodendrocyte in the CNS myelinates multiple axons, each Schwann cell in the PNS myelinates only one axonal segment. Additionally, peripheral myelin exhibits unique cytoplasmic features, such as Cajal bands and Schmidt–Lanterman incisures, which are absent from CNS myelin, reflecting the distinct cellular architecture and dynamic requirements of peripheral nerves. Functionally, the segmental organization of internodes and nodes constitutes a high-fidelity biological design for long-distance electrical transmission: action potentials initiated at one node of Ranvier generate passive currents that travel rapidly through the low-capacitance internode to depolarize the next node, thereby regenerating the signal at full amplitude. This architecture maximizes both conduction velocity and metabolic efficiency by localizing ion exchange to nodal regions while minimizing energy expenditure across internodes[11].

Beyond its insulation and electrical roles, PNS myelin provides mechanical and metabolic support, essential for axonal survival. Schwann cells supply trophic factors and maintain axonal homeostasis through reciprocal signaling mechanisms, and the myelin sheath itself acts as a barrier that preserves the microenvironment of the nerve fiber. Importantly, unlike the CNS, the PNS retains a substantial regenerative capacity. Following injury, myelinating Schwann cells dedifferentiate into a repair phenotype that clears myelin debris, secretes growth-promoting factors, and forms bands of Büngner, longitudinal cellular structures that guide regenerating axons back to their targets[13]. This capacity for dedifferentiation and remyelination underscores the remarkable plasticity of Schwann cells, highlighting the PNS as an exceptional model for studying glial regeneration and repair. Understanding the cellular and molecular regulation of myelination in the PNS is thus essential not only for basic neurobiology but also for the development of therapeutic strategies for demyelinating neuropathies such as Charcot–Marie–Tooth disease (CMT).

1.2 The PNS Myelin Sheath: Structure and Composition

The myelin sheath has a unique lamellar architecture and a distinct proteolipid composition that sets it apart from all other cellular membranes. The sheath consists of coiled lipid bilayers interleaved with specific myelin proteins, resulting in a tightly packed, highly insulating structure.

1.2.1 Lamellar Architecture of Myelin

PNS myelin wraps around an axon in a tight and highly ordered, repeating lamellar structure. This structure is composed of two central regions: compact myelin and non-compact myelin[22].

The compacted membranes are defined by alternating major dense lines (MDLs) and intraperiod lines (IPLs) and are clearly visible by electron microscopy. MDL is approximately 2–3 nm wide and is formed by the tight apposition and fusion of the inner, cytoplasmic leaflets of the Schwann cell membrane. The lighter, wider line IPL, measuring about 4 nm, represents the close apposition of the outer, extracellular surfaces of the membrane[23].

Non-compact myelin comprises specialized domains, including the SLIs and the nodes of Ranvier.

SLIs are small, cone-shaped channels of cytoplasm that traverse the compact myelin at scattered intervals. These incisures spiral through the myelin layers, creating a continuous cytoplasmic connection between the main Schwann cell body (abaxonal cytoplasm) and the thin layer of cytoplasm adjacent to the axon (adaxonal cytoplasm). SLIs are believed to be crucial for the transport of metabolites and other molecules across the thick myelin sheath, thus playing a vital role in the metabolic maintenance, growth, and overall health of the myelin and the axon it supports[24,25]. These structures are stabilized by adherens junctions, which contain proteins such as E-cadherin and catenins[26].

The myelin sheath is segmented, with each segment, or internode, being produced by a single Schwann cell. The gaps between these internodes are the nodes of Ranvier, which are short, unmyelinated regions of the axon approximately 1 μm in length. At these nodes, the axonal membrane is exposed to the extracellular environment and is densely populated with voltage-gated sodium and potassium

channels[16]. This specific molecular architecture is fundamental to saltatory conduction, as it enables the action potential to be regenerated at each node, allowing it to "leap" from one node to the next, dramatically increasingnerve conduction velocity.

1.2.2 Protein and Lipid Composition

PNS myelin has an exceptionally high lipid content and a distinct protein repertoire. By dry weight, myelin is approximately 70–80% lipid and 20–30% protein, a significantly higher lipid-to-protein ratio than typical cellular membranes (~50/50)[27]. This high lipid content is essential for creating a hydrophobic barrier that minimizes ion leakage.

Lipid Composition

The lipidome of myelin is characterized by a high proportion of cholesterol and specific glycolipids, which are crucial for the formation of its compact, multilayered structure. The three major lipid classes are cholesterol (~40%), phospholipids (~40%), and glycolipids (~20%).

Cholesterol is a critical structural component of myelin. Its rigid, planar structure inserts into the lipid bilayer, increasing packing density and reducing the membrane's permeability to water and ions. Cholesterol is an essential factor for myelination in the PNS playing a regulatory role for the proper trafficking of Myelin Protein Zero (MPZ) from the ER to the growing myelin sheath, a step that is vital for myelin compaction[28].

Galactocerebrosides are the most abundant glycolipids in PNS myelin and are a hallmark of this specialized membrane[29]. Galactocerebrosides and their derivatives (sulfatides) are indispensable for the insulator function of the myelin sheath. Their absence, as demonstrated in genetic mouse models, leads to a functional breakdown of the myelin lipid bilayer, severely impairing its packing and increasing its fluidity and permeability[30]. This ultimately results in the loss of saltatory conduction and a severe dysmyelinating phenotype.

Protein Composition

While less abundant than lipids, myelin proteins are essential for the adhesion and compaction of the membrane layers and for maintaining the long-term integrity of

both myelin and axon. A few abundant proteins dominate PNS myelin. The immunoglobulin-domain protein MPZ is the single most abundant myelin protein in the PNS, constituting roughly 40–45% of total myelin protein[17]. MPZ mediates adhesion of the extracellular leaflets at the major dense line, acting as a homophilic cell-adhesion molecule between adjacent layers of compact myelin[31]. Since MPZ is the subject of this thesis, it will be discussed in detail below in Chapters 1.3, 1.4. Myelin basic protein (MBP) is the next most abundant component (on the order of ~15–20% of total protein), and together with MPZ's cytoplasmic tail helps glue together the inner (cytoplasmic) faces of the myelin membrane[17]. Immunoblot and proteomic analyses confirm that MPZ, MBP, and also peripheral myelin protein 2 (P2) are strongly enriched in purified PNS myelin, whereas non-myelin markers are depleted. For example, a mass-spectrometry study found MPZ to be about 44% of PNS myelin protein, MBP about 18%, and periaxin (PRX) about 15%[32]. Other compact-myelin proteins include PMP22, a small hydrophobic tetraspan glycoprotein (roughly a few percent of protein), and P2 (FABP8), a fatty-acid-binding protein implicated in lipid transport; both are less abundant than MPZ or MBP but contribute to membrane stability.

In the non-compact compartments of Schwann cell myelin, the major protein is PRX. PRX has two isoforms (large and small) that share an N-terminal PDZ domain important for dimerization[33,34]. Periaxin accounts for roughly 15–16% of PNS myelin protein, making it the single most abundant protein in non-compact regions[31,35]. Its long cytoplasmic tail (in the large isoform) helps organize Cajal bands and abaxonal appositions via interactions with dystroglycan and related proteins. Other non-compact myelin proteins include gap-junction connexins (e.g. Cx32, Cx29) which form interlamellar channels for ions and small metabolites, and myelin-associated glycoprotein (MAG), a minor IgCAM localized to the adaxonal (periaxonal) surface that mediates axon–glia adhesion[36].

The following chapters will focus on MPZ, which is the central protein in the present PhD work.

1.3 MPZ

MPZ (Figure 3) is the major "adhesive" protein of PNS myelin, responsible for gluing together the myelin lamellae in compact myelin[37,38]. In the absence of MPZ, myelin fails to achieve normal compaction: homozygous MPZ-knockout mice develop severe dysmyelination with unstable, redundant myelin wraps and neuropathic deficit[39]. The following sections detail its molecular structure and the mechanisms by which MPZ promotes myelin sheath compaction through homophilic and heterophilic interactions.

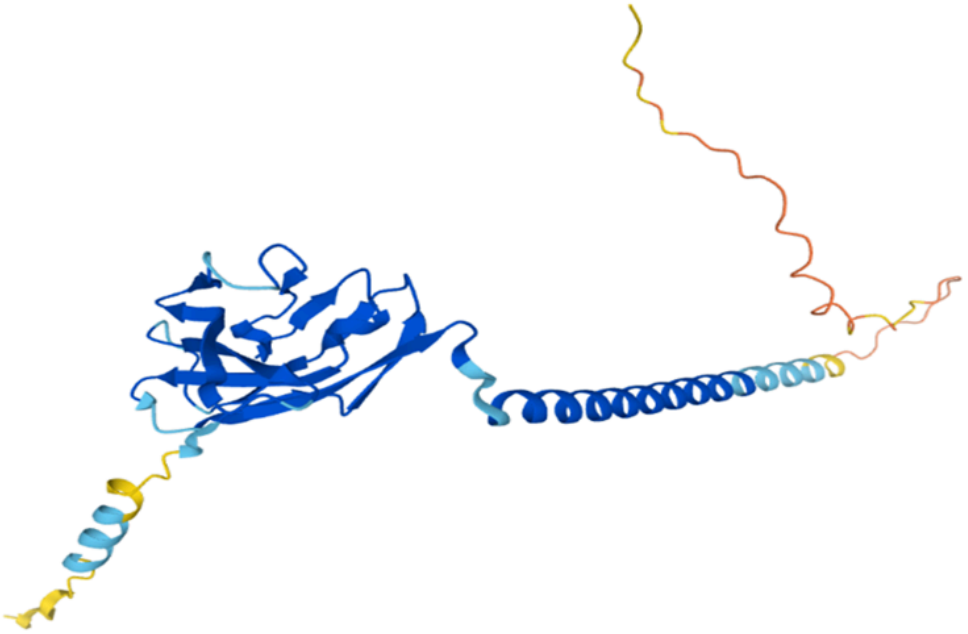

Figure 3. Structural model of MPZ. The three-dimensional conformation of the extracellular immunoglobulin-like domain is based on the crystal structure retrieved from the Protein Data Bank (PDB ID: 3OAI)

1.3.1 Molecular Structure of MPZ

MPZ is a type I transmembrane protein composed of three domains (Figure 4): an N-terminal extracellular domain (~120 amino acids) with an immunoglobulin-like (Ig) fold, a single transmembrane (TM) helix (~25–30 amino acids), and a C-terminal cytoplasmic tail (~70 amino acids), devoid of structure. MPZ is synthesized as a precursor with a signal peptide (~30 residues) that is cleaved upon insertion into the endoplasmic reticulum (ER) membrane, yielding the mature 218–amino acid protein[40]. The extracellular domain of MPZ (MPZ_{ex}) is globular and adopts the immunoglobulin superfamily V-set structure (a

β-sandwich composed of ~10 β-strands)[27,41]. High-resolution X-ray crystallography of the MPZ_{ex} domain, first solved for rat MPZ at 1.9 Å, confirmed this Ig-like β-sandwich architecture and provided clues to MPZ's adhesive interface[38]. Notably, two MPZ Ig domains can interact head-to-head in an antiparallel fashion, aligning β-strands from each molecule to form a continuous β-sheet across the interface[38,40]. This crystallographic dimer was hypothesized to represent the trans interaction between MPZ molecules on apposed myelin membranes, a homophilic adhesion complex[37,38]. The MPZ_{ex} contains a single conserved N-glycosylation site at Asn^122, which carries an unusual HNK-1 carbohydrate epitope (a sulfated glucuronic acid–containing glycan common in nervous system glycoproteins)[40,42,43]. This N-linked glycan is thought to project from the Ig domain and may help orient or space the MPZ molecules for optimal adhesive binding; indeed, proper glycosylation of MPZ is required for normal myelin compaction and mutations affecting the glycosylation site cause dysmyelination[44].

The single-pass transmembrane domain of MPZ is a hydrophobic α-helix that not only anchors MPZ in the myelin membrane but also contributes to MPZ–MPZ associations within the membrane plane. The TM helix contains a "glycine zipper" motif (a GxxxGxxxG sequence, in human MPZ residues 159–167) that is conserved and known to facilitate helix–helix packing. Biochemical and biophysical studies have shown that the MPZ transmembrane domains can dimerize in the lipid bilayer, potentially forming MPZ cis-dimers (i.e. within the same membrane)[45]. In particular, Plotkowski et al. (2007)[45] demonstrated by mutagenesis that the glycine zipper promotes MPZ TM–TM dimerization, suggesting that MPZ may assemble laterally into dimers or oligomers in the myelin membrane. Such lateral oligomerization could strengthen the adhesive complex by aligning multiple MPZ molecules.

The cytoplasmic tail of MPZ ($P0_{ct}$) is a ~69–70 amino acid, highly basic domain that resides on the inner (cytoplasmic) face of the myelin sheath. Its amino acid composition includes numerous residues lysine, arginine, and histidine giving the human MPZ tail a positively charged net charge, enabling the tail to bind to acidic lipid headgroups in the inner leaflet of the Schwann cell membrane[41]. Structurally,

the MPZ tail is intrinsically disordered in solution (lacking fixed secondary structure), but it undergoes a conformational change upon membrane binding. Biophysical studies using circular dichroism and X-ray diffraction show that $P0_{ct}$, when associated with negatively charged lipid vesicles, adopts a more ordered structure (enriched in α-helix) and can even induce stacking of lipid bilayers in vitro[41]. Several post-translational modifications modulate the MPZ tail's membrane-associating function. One key modification is palmitoylation: a conserved cysteine near the junction of the TM and cytosolic domains (Cys^182 in human MPZ) is reversibly S-acylated with palmitate (S-palmitoylation)[46,47]. Palmitoylation anchors the tail more firmly to the membrane and is required for full adhesive function of MPZ, as mutations affecting the palmitoylation site abolish MPZ's ability to maintain compact myelin, leading to unstable membranes[48]. Additionally, the MPZ cytoplasmic domain contains multiple consensus sites for phosphorylation by protein kinases. Phosphorylation of the MPZ tail (notably by protein kinase C and Ca^{2+}/calmodulin-dependent kinase II) occurs in myelin and in Schwann cells, and this modification can regulate MPZ's adhesive interactions. In vitro mapping identified a major phosphorylation site at Ser^34 of the tail (in rodents)[49]. Functional studies revealed that preventing normal MPZ tail phosphorylation – for example, by certain tail mutations – impairs myelin formation, whereas mimicking constitutive phosphorylation can enhance adhesion[50]. In fact, MPZ requires an adaptor protein (RACK1) that tethers conventional PKCα to the MPZ tail, enabling PKC to phosphorylate MPZ during myelination[51]. Disruption of this MPZ–RACK1–PKC complex (e.g. in the Mpz^{R98C} mutant mouse) leads to hypomyelination[51,52]. Thus, dynamic phosphorylation of the tail appears to modulate how tightly the cytoplasmic surfaces are apposed, possibly as a mechanism to fine-tune myelin wrapping or to signal the Schwann cell during myelin maturation. In summary, the MPZ molecule can be viewed as having a "dual-anchor" design: the extracellular Ig-like domain anchors adjacent membranes together via homophilic binding, while the cytoplasmic tail anchors to membrane lipids and contributes to intracellular membrane compaction. The single TM helix connects these domains and also mediates lateral associations and interactions with other myelin proteins. We next consider how these structural features enable MPZ to drive myelin sheath formation through homophilic and heterophilic adhesion mechanisms.

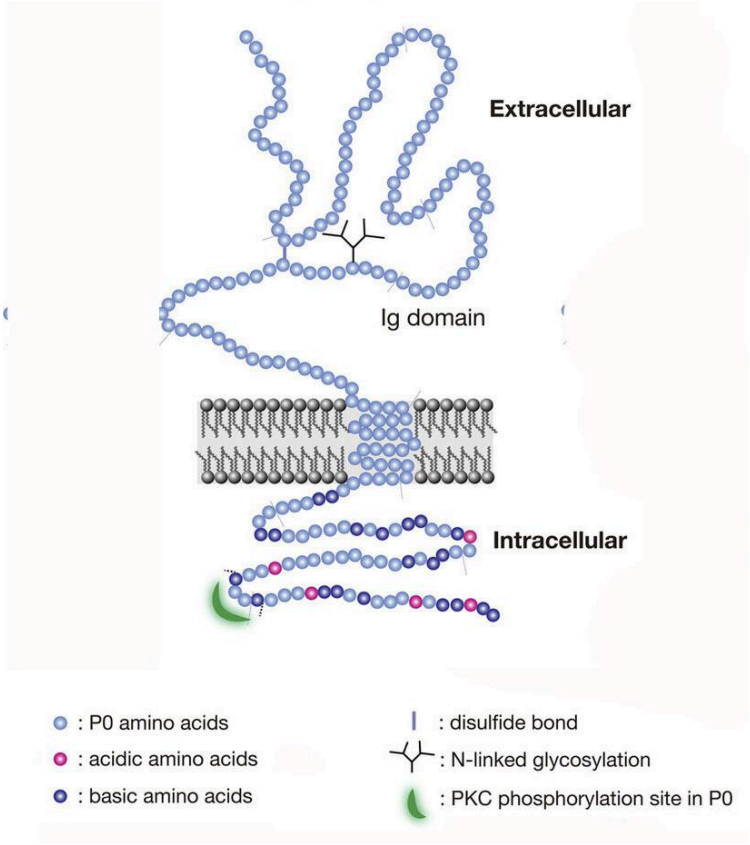

Figure 4. Schematic domain organization of the MPZ. The protein comprises an extracellular immunoglobulin (Ig)-like domain responsible for homophilic adhesion between apposing myelin membranes, a single transmembrane helix anchoring MPZ in the membrane, and a basic cytoplasmic tail (C-terminal) involved in membrane apposition and compaction. Figure adapted from [53]

1.3.2 MPZ and Myelin Sheath Formation: Homophilic and Heterophilic Adhesion

During peripheral myelination, MPZ molecules are strategically positioned in the extracytosolic space between each wrap of the Schwann cell membrane. As a myelin internode matures, MPZ accumulates at the interface of the closing extracellular gap and engages in extensive homophilic adhesion with MPZ molecules on the apposed membrane. The end result of this process is the formation of the PNS myelin IPL, where the extracellular faces of two Schwann cell membrane layers are tightly "zipped" together. This arrangement is the foundation of the "zipper-like" framework model proposed by Raasakka et al.[54] based on cryo-electron microscopy (EM), for which other structural models and electron microscopy provide compelling evidence (Figure 5).

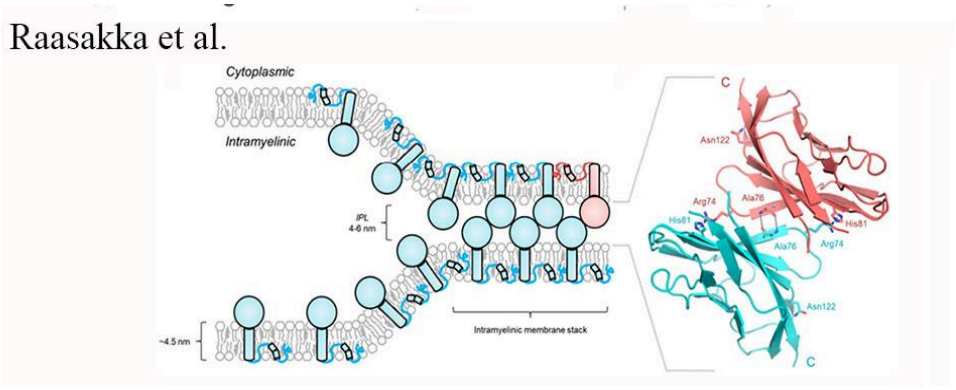

Figure 5 The "Zipper-Like" Framework (Raasakka et al.): Derived from cryo-EM of full-length MPZ, this model suggests that adhesion is mediated by a translational array of antiparallel trans-dimers, without the formation of larger cis-oligomers.

Cryo-EM of full-length MPZ reconstituted in lipid bilayers has visualized a regular, quasi-crystalline array of MPZ Ig domains bridging two adjacent membranes. In these reconstructions, MPZ forms an inter-membrane zipper: monomers from each membrane pair up across the gap, and many such pairs assemble into a two-dimensional lattice of alternating MPZ molecules from opposite sides. The measured spacing between the two apposed membrane surfaces is ~5 nm (50 ± 10 Å), which matches the periodicity of the native myelin IPL. Notably, the interacting MPZ Ig domains do not directly insert into the opposing membrane; instead, two rows of Ig domains meet in the center of the gap, consistent with a homophilic binding mechanism (each MPZ binds its counterpart, rather than binding to a different partner on the opposite side)[41]. This homophilic MPZ–MPZ interaction is characterized by low affinity, with a dissociation constant (K_d) estimated in the millimolar range (~2-10 $*10^{-3}$ M)[38]. While weak at the level of a single binding interface (as is typical for cell-adhesion proteins), the collective strength from the multitude of MPZ molecules on a myelin wrap provides robust adhesion. Indeed, the zipper-like lattice ensures that a large surface area of membrane is bonded by MPZ, generating a strong adhesive force that holds the myelin layers together under mechanical stress.

Crystallographic and mutational data further support the homophilic adhesion model. The X-ray crystal packing of the MPZ Ig domain (rat MPZ) revealed the symmetric dimer interface described earlier, in which each Ig domain contributes

with a β-strand that pairs with its partner's strand to form an antiparallel β-sheet. This dimer aligns the C-termini of the Ig domains such that they would be positioned near the membrane surfaces, perfectly oriented for the contiguous transmembrane helices to span into the respective bilayers. When two such dimers from opposite sides cluster, they create a tetrameric complex (often conceptualized as a dimer of dimers) that bridges the two membranes. This tetramer is considered a fundamental building block in competing adhesion models, although its final arrangement is debated, leading to proposals like the stacked octamer model[55] or alternative tetrameric assemblies [56] (figure 6).

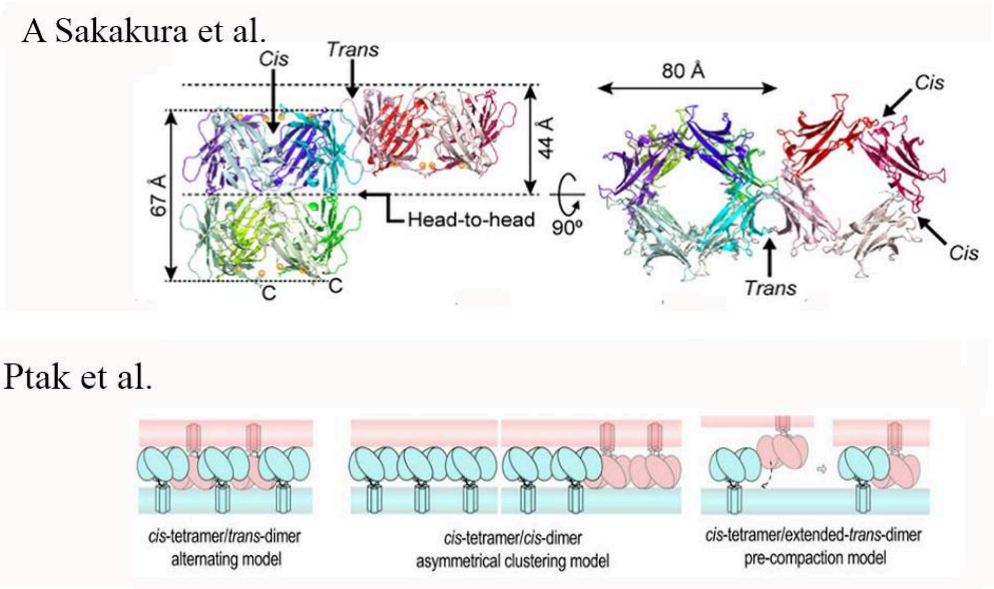

Figure 6. The "Stacked-Rings Octamer" Model (Sakakura et al.): Based on crystallography and a "nanomyelin" assay, the adhesive unit is proposed to be an 8-mer, formed by the head-to-head stacking of two tetramers which are assembled via cis interactions. **Alternative Tetramer-Based Models (Ptak et al.):** This work establishes the cis-tetramer as the fundamental building block but experimentally refutes the canonical trans-dimer interaction (left). It proposes new arrangements, such as asymmetrical cis-clustering on the same membrane (center) or a pre-compaction state mediated by a novel, extended trans interface (right).

In myelin, MPZ is so densely packed that essentially every Ig domain finds a partner across the gap. Mutations in the MPZ Ig domain that disrupt its folding or surface properties frequently abolish this homophilic adhesion and cause demyelinating neuropathies. For example, a single amino acid substitution in the Ig interface (such as a charged residue replacing a neutral one) can prevent the MPZ molecules from correctly pairing, leading to uncompacted myelin and clinical neuropathy[57]. A notable case is the heterozygous MPZ mutation

His52Pro, which affects the Ig domain and is known to cause a dominantly inherited demyelinating neuropathy (Charcot-Marie-Tooth disease type 2J, or CMT2J)[58]; structural studies indicate this mutation alters the Ig dimerization interface and thereby weakens adhesion. These genotype–phenotype correlations reinforce the central importance of MPZ's homophilic binding in myelin sheath formation.

While MPZ's trans-interaction (between opposing membranes) is the cornerstone of myelin compaction, its cis-interactions (within the same membrane) also contribute to the architecture. As mentioned, MPZ's transmembrane segment can mediate lateral dimerization through the glycine zipper motif. It has been proposed that MPZ first forms cis-dimers in each membrane, which then engage in trans-dimerization to create the tetrameric adhesive unit[45,59]. This stepwise assembly could help align MPZ molecules in register between layers. Supporting this idea, chemical cross-linking and biochemical studies have detected MPZ dimers in myelin membranes, and altering the TM glycine motif impairs MPZ's adhesive function without preventing its surface expression. Moreover, MPZ's cytoplasmic tail, by virtue of binding to membrane lipids, may promote a quasi-regular lattice arrangement of MPZ on the cytosolic face. As the tails attach to the inner leaflet and gain structure, they could cluster MPZ molecules and "zip" together adjacent inner leaflets (in cooperation with MBP). In fact, experiments show that the MPZ tail can induce ordered stacking of membranes (producing a measurable repeat distance by X-ray diffraction) when present at high concentration[41]. In myelinating cells, the MPZ tail likely works in tandem with MBP to achieve maximal cytoplasmic compaction: Schwann cells lacking MBP and P2 protein still form a basic compact myelin, presumably because P0; can partially fulfill the stacking role, but the myelin is not as stable long-term without MBP/P2[60]. Thus, homophilic adhesion via the extracellular domains brings the membranes together, and interactions involving the transmembrane and cytoplasmic domains help stabilize and tighten the assembly laterally and cytoplasmically.

In addition to homophilic self-adhesion, MPZ participates in heterophilic interactions that modulate myelin assembly. The most significant is the interaction between MPZ and peripheral myelin protein 22 (PMP22), which is the second-most abundant protein of PNS myelin. PMP22 is a tetraspan membrane

protein, and like MPZ it is crucial for myelin stability[61]. For years it was hypothesized that PMP22 might physically associate with MPZ in the compact myelin membrane, given that both co-localize in the intraperiod line and both have adhesion-related roles[54]. Recent research has confirmed that MPZ and PMP22 form a specific complex within the myelin membrane: Pashkova et al. (2024) showed that MPZ and PMP22 directly interact via their transmembrane domains, and that this interaction is disrupted by a known PMP22 mutation (A67T) that causes a mild neuropathy. Notably, the A67T mutation in PMP22 lies in the predicted interface for MPZ–PMP22 binding, and its presence abolishes the MPZ–PMP22 association without affecting PMP22's membrane localization. This indicates that the MPZ–PMP22 heterophilic interaction has a functional role: when it is lost, myelin stability is compromised, leading to neuropathic changes. The precise biological role of the MPZ–PMP22 complex has not yet been completely understood. Such interaction might help organize lipid microdomains (both MPZ and PMP22 are known to partition into cholesterol/sphingolipid-rich myelin rafts)[54], or it might provide an additional adhesive or signaling linkage within compact myelin. Interestingly, optimal reconstitution of PMP22 into artificial membranes requires the presence of specific lipids (like sphingomyelin) that are also present when MPZ is incorporated, hinting at co-operative behavior. Heteromeric MPZ–PMP22 complexes could contribute to the architecture or resilience of compact myelin beyond what homophilic MPZ interactions alone achieve.

Aside from PMP22, MPZ's interactions are largely homophilic, but MPZ does have other heterophilic partners in a broader context. For example, within the Schwann cell, the MPZ cytoplasmic tail binds to the scaffolding protein RACK1 (as noted earlier), linking MPZ to intracellular signaling pathways that influence myelination[51]. Moreover, during myelin development, trans-interactions between glial and axonal cell-adhesion molecules (such as MAG on the glial side and axonal ligands) occur at non-compact regions. However, MPZ is excluded from those non-compact regions (paranodes, incisures) and concentrates only in compact myelin. This compartmentalization ensures that MPZ homophilic binding is not interfered with by other adhesion systems. MPZ thus acts as a dedicated, specialized adhesion molecule for the compact myelin compartment.

Experimental models strongly support MPZ's roles described above. In X-ray crystallography and cryo-EM studies, we have seen direct visualization of MPZ's adhesive interfaces[38]. In genetic models, Mpz-knockout mice completely lack compact myelin and exhibit tremors and nerve conduction block, mirroring a severe congenital neuropathy[62]. Transgenic mice expressing certain human MPZ mutations (for instance, the deadly S63del or R98C mutations) develop demyelinating neuropathies, faithfully replicating the human disease and highlighting the mutation's effect on MPZ function[57]. Conversely, overexpression of wild-type MPZ in mice causes hypermyelination but also occasional myelin abnormalities, indicating that an optimal level of MPZ is required (excess MPZ can be detrimental, possibly by forming too much adhesion or aggregating)[63]. These models highlight that MPZ's adhesive activity must be finely balanced. Finally, biochemical assays such as lipid vesicle aggregation or cell adhesion assays have allowed dissection of MPZ domains: for example, isolated MPZ Ig domains will self-associate and cause vesicle clumping (simulating the extracellular adhesion)[59], and synthetic peptides of the MPZ tail can induce membrane stacking (simulating cytoplasmic apposition)[41]. Such experiments confirm that each part of MPZ contributes to membrane binding or stacking in line with its in vivo role.

1.4 Charcot-Marie-Tooth Disease and MPZ-Related Neuropathies

1.4.1 Clinical features and classification of CMTs

CMT disease is the most common inherited peripheral neuropathy, encompassing a group of hereditary motor and sensory polyneuropathies[64,65]. It is a chronic, length-dependent disorder leading to slowly progressive distal muscle weakness and atrophy, most prominently in the feet, often resulting in high-arched *pes cavus* deformities, and later the hands[66,67]. Deep-tendon reflexes are typically reduced or absent, and mild sensory loss is common. Symptoms usually begin in the first or second decade of life, although milder forms may present later.

CMT has traditionally been divided by neurophysiology into demyelinating (CMT1) versus axonal forms (CMT2)[64,65]. In demyelinating CMT, median nerve conduction velocities (NCVs) are uniformly slow (often <35–38 m/s), reflecting defective Schwann cell/myelin function[65,68,69]. In CMT2, NCVs are near normal

(>45 m/s), but compound muscle action potentials are reduced, indicating primary axon degeneration. An intermediate category, sometimes called dominant-intermediate CMT, has NCVs between these ranges. Inheritance patterns also help classify CMT: autosomal dominant forms are most common, accounting for most CMT1 and CMT2 cases, followed by X-linked forms (e.g. GJB1-related CMTX1) and rare autosomal recessive forms[65]. Over 100 genes have been implicated in CMT, table 1 summarizes the CMT classification. Overall, mutations in PMP22, MPZ, GJB1, MFN2 account for the great majority of diagnosed case:

- CMT1A – the most common form (≈50% of cases), due to a 1.5-Mb duplication of chromosome 17 (PMP22) causing a uniform demyelinating neuropathy[70,71];
- CMT1B – caused by point mutations in the MPZ gene, leading to a demyelinating neuropathy[72];
- CMT2A – the most frequent axonal subtype, caused by mutations in the mitofusin-2 gene MFN2[73,74];
- CMTX1 – an X-linked demyelinating form due to connexin-32 defects[75,76];
- Other rare forms include recessive CMT4 variants and dominantly inherited forms such as CMT1C, CMT1D, etc.

CMT	*Locus*	*Gene*	*Product*	*OMIM*
CMT1A	17p11.2	*PMP22*	Peripheral myelin protein 22	118220
CMT1B	1q22	*MPZ*	Myelin protein zero	118200
CMT1C	16p13.1–p12.3	*SIMPLE/LITAF*	SIMPLE	601098
CMT1D	10q21.1–q22.1	*EGR2*	Early growth response protein 2	607678
CMT1E	17p11.2	*PMP22*	Peripheral myelin protein 22	118220
CMT1F	8p21	*NEFL*	Neurofilament triplet L protein	607684
CMT2A	1p36	*MFN2*	Mitofusin 2	118210
CMT2B	3q21	*RAB7*	Ras-related protein Rab-7	600882
CMT2B1	1q21.2	*LMNA*	Lamin A/C	605588
CMT2B2	19q13.3	*Unknown*	Unknown	605589
CMT2C	12q23–q24	*Unknown*	Unknown	606071
CMT2D	7p15	*GARS*	Glycyl-tRNA synthetase	601472
CMT2E/F1	8p21	*NEFL*	Neurofilament triplet L protein	607684
CMT2F	7q11–q21	*HSPB1*	Heat-shock protein B1	606595
CMT2G	12q12–q13	*Unknown*	Unknown	608591
CMT2H	8q21.3	*Unknown*	Unknown	607731
CMT2I	1q22	*MPZ*	Myelin protein zero	118200
CMT2J	1q22	*MPZ*	Myelin protein zero	118200
CMT2K	8q13–q21.1	*GDAP1*	Ganglioside-induced differentiation protein 1	214400
CMT2L	12q24	*HSPB8*	Heat shock protein B8	608673
CMT4A	8q13–q21.1	*GDAP1*	Ganglioside-induced differentiation protein 1	214400
CMT4B1	11q22	*MTMR2*	Myotubularin-related protein 2	601382
CMT4B2	11p15	*SBF2/MTMR13*	SET binding factor 2	604563
CMT4C	5q32	*SH3TC2*	SH3TC2	601596
CMT4D	8q24.3	*NDRG1*	NDRG1 protein	601455
CMT4E	10q21.1–q22.1	*EGR2*	Early growth response protein 2	607678
CMT4F	19q13.1–q13.2	*PRX*	Periaxin	145900
CMT4G	10q23.3	*Unknown*	Unknown	605285
CMT4H	12p11.21–q13.11	*FGD4*	FRABIN	609311
CMT4J	6q21	*FIG4*	FIG4	611228
DI-CMTA	10q24.1–q25.1	*Unknown*	Unknown	606483
DI-CMTB	19p12–13.2	*DNM2*	Dynamin 2	606482
DI-CMTC	1p35	*YARS*	Tyrosyl-tRNA synthetase	608323
DI-CMTD	1q22	*MPZ*	Myelin protein zero	607791
CMTX	Xq13.1	*GJB1*	Gap junction β-1 protein, connexin 32	302800

Table 1 CMT Classification, reprinted from (Szigeti e Lupski, 2009)[77]

1.4.2 MPZ and the Pathogenesis of Charcot-Marie-Tooth

The MPZ gene gives rise to a remarkably broad and heterogeneous spectrum of inherited peripheral neuropathies that account for roughly 5–10% of CMT overall (second after PMP22 in demyelinating forms) and about 6% of CMT cases in some cohorts[78] (Figure 7). This clinical diversity is a cardinal feature of MPZ-related disease, where pathogenic variants within a single gene can precipitate conditions ranging from severe, congenital failures of myelination to mild, late-onset axonal degeneration that may not manifest until the fourth or fifth decade of life. MPZ-related neuropathies are more accurately stratified into at least three distinct, albeit sometimes overlapping, clinical subgroups based on age of onset, electrophysiological characteristics, and the underlying pathological process. This stratification provides a crucial clinical framework for understanding the distinct molecular pathomechanisms that drive the disease in different patient populations.

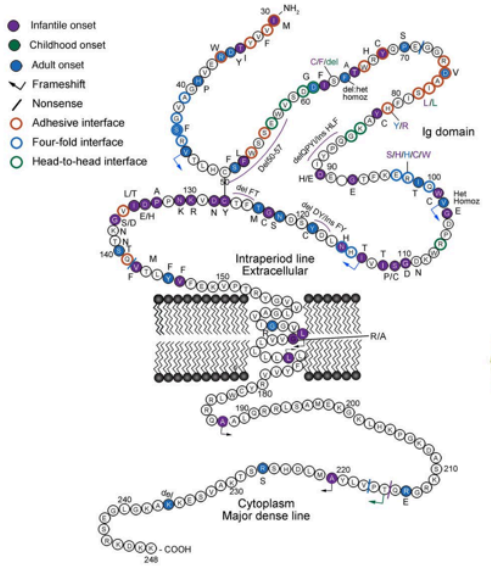

Figure 7 Mutations in the MPZ gene associated with inherited neuropathies[79].

Severe Early-Onset Demyelinating Neuropathy

The most severe presentation of MPZ-related neuropathy manifests in infancy, typically with an onset before five years of age. This group encompasses phenotypes historically classified as Dejerine-Sottas Syndrome (DSS) and Congenital Hypomyelinating Neuropathy (CHN), which are characterized by profound motor delays, hypotonia, and severe weakness from a very early age[77,80]. Electrophysiological studies are a key diagnostic hallmark, revealing profoundly NCVs, often falling below 15 m/s and in some cases being unrecordable. Pathologically, nerve biopsies show severe dysmyelination (i.e. formation of defective myelin) or hypomyelination (i.e. insufficient myelin production), with thinly myelinated or completely unmyelinated large-caliber axons and prominent "onion bulb" formations, which consist of concentric layers of supernumerary Schwann cell processes surrounding axons in a failed attempt at remyelination[81,82]. Patients in this group often experience a more rapid disease progression and accumulate significant disability, frequently requiring walking aids or wheelchairs for ambulation during childhood or adolescence.

Childhood-Onset Demyelinating Neuropathy (Classic CMT1B)

This intermediate phenotype aligns more closely with the "classic" presentation of CMT, with a more gradual onset of symptoms during the first two decades of life. Affected individuals typically present with slowly progressive, length-dependent distal muscle weakness and atrophy, primarily affecting the feet and lower legs and later the hands.Sensory loss, particularly for vibration and proprioception, is also a common feature. Electrophysiologically, this form is characterized by uniformly slow NCVs in the demyelinating range, typically between 15 and 30 m/s, which is slower than normal but generally faster than the severe infantile-onset group[83,84]. The pathology in this subgroup suggests that Schwann cells are capable of forming a mature, albeit structurally abnormal or unstable, myelin sheath. The disease process is one of chronic demyelination and remyelination, leading to a slow but progressive decline in peripheral nerve function over many years. The clinical course is generally less severe than the infantile-onset form, with most patients remaining ambulatory throughout their lives, although many require the use of ankle-foot orthoses to manage foot drop.

Adult-Onset Axonal Neuropathy (CMT2I/J)

CMT2J (also called late-onset CMT1B) are adult-onset neuropathies with a unique phenotype among MPZ mutations, displaying axonal, rather than demyelinating, neuropathy characteristics.

In these cases, symptoms typically do not appear until the third, fourth, or even later decades of life. The clinical manifestation is one of a distal axonal polyneuropathy, with weakness and sensory loss similar in distribution to other forms of CMT but often milder in severity. The key distinguishing feature is the electrophysiology: NCVs are normal or only mildly reduced (typically >45 m/s), while compound muscle action potential (CMAP) amplitudes are significantly reduced[20,85,86]. This pattern indicates a primary degeneration of the axon itself, rather than a primary defect in the myelin sheath. This suggests that developmental myelination proceeds largely unimpeded, and the myelin sheath is formed correctly. Some patients with this form of the disease may also present with atypical features not commonly seen in other CMT subtypes, such as sensorineural hearing loss or pupillary abnormalities like Adie's pupil.

1.4.3 Molecular Pathogenesis

The remarkable clinical heterogeneity observed in MPZ-related neuropathies is not arbitrary but is instead a direct reflection of distinct underlying molecular pathomechanisms. The specific location and biochemical consequence of a given mutation within the MPZ protein dictates how its function is disrupted, thereby initiating a specific cellular cascade that leads to one of the characteristic clinical phenotypes. Decades of research using cell culture systems, preclinical animal models, and structural biology have converged on a unifying framework that categorizes these pathogenic mechanisms into a triad of dysfunction. The first, and often most severe, is a toxic gain-of-function mechanism driven by protein misfolding and the chronic activation of the unfolded protein response (UPR). The second involves a structural failure, where mutations disrupt the protein's essential adhesive functions, leading to improperly compacted and unstable myelin. The third is a dosage-dependent mechanism, or haploinsufficiency, where

a simple reduction in the quantity of functional protein is unable to maintain myelin on the long-term . Understanding this triad is fundamental, as it not only provides a rational basis for the observed genotype-phenotype correlations but also illuminates distinct molecular targets for the development of rational, mechanism-based therapeutic strategies.

Gain-of-Function Toxicity: Protein Misfolding and the Unfolded Protein Response (UPR)

The most severe, early-onset forms of CMT1B and DSS are frequently caused by toxic gain-of-function mechanisms initiated by the production of a misfolded and aggregation-prone MPZ protein[87]. Missense mutations located within the structural core of the MPZ Ig-like domain can severely disrupt its tertiary structure, preventing the protein from folding correctly within the ER of the Schwann cell. Unable to pass the cell's stringent protein quality control checkpoints, this aberrant protein is retained and accumulates within the ER lumen, triggering a state of chronic ER stress[88].

To cope with this proteotoxic stress, the Schwann cell mounts a complex signaling network known as the UPR. The UPR is an adaptive program designed to restore ER homeostasis by attenuating protein synthesis, upregulating chaperone proteins to assist in folding, and enhancing the degradation of misfolded proteins through a process called ER-associated degradation (ERAD)[87]. The UPR is orchestrated by three transmembrane ER stress sensors: PERK, IRE1, and ATF6[87]. Figure 8 summarizes the UPR in demyelinating CMT.

The PERK Pathway

Upon sensing an accumulation of unfolded proteins, the PKR-like ER kinase (PERK) dimerizes and autophosphorylates[89]. Activated PERK then phosphorylates the eukaryotic translation initiation factor 2 alpha. This phosphorylation leads to a global attenuation of protein translation, thereby reducing the protein load entering the ER[89,90]. Paradoxically, phosphorylation selectively enhances the translation of certain mRNAs, most notably that of Activating Transcription Factor 4 (ATF4), a transcription factor that upregulates genes involved in amino acid metabolism, antioxidant responses, and, crucially, apoptosis[91–93]. A key pro-apoptotic target of ATF4 is the transcription factor

C/EBP homologous protein (CHOP). While transient UPR activation is protective, the chronic and unresolved ER stress caused by intractable mutant MPZ leads to sustained high levels of CHOP, which ultimately drives the Schwann cell towards apoptosis[94,95].

The IRE1 Pathway

Inositol-requiring enzyme 1 (IRE1) is another ER stress sensor that, upon activation, exhibits an endoribonuclease activity with its charactering function of the unconventional splicing of the X-box binding protein 1 (XBP1) mRNA[96,97] . This splicing event produces a potent transcription factor, XBP1s, which migrates to the nucleus and activates the expression of genes encoding ER chaperones (like BiP/GRP78) and components of the ERAD machinery. This arm of the UPR represents a primary adaptive response aimed at clearing the misfolded protein burden and expanding the ER's folding capacity[98].

The ATF6 Pathway

Activating Transcription Factor 6 (ATF6) is a transmembrane protein that, in response to ER stress, translocates from the ER to the Golgi apparatus where is cleaved by proteases, releasing its cytosolic N-terminal domain[99]. This fragment then travels to the nucleus, where it functions as a transcription factor to upregulate the expression of ER chaperones and other UPR-related genes.

In the context of severe MPZ mutations, this initially protective UPR becomes a primary driver of pathology. The continuous production of a mutated MPZ protein that cannot be correctly folded or efficiently cleared leads to chronic, unrelenting UPR activation in myelinating Schwann cells[57,87,95]. Sustained signaling through the PERK–eIF2α–ATF4–CHOP axis is particularly cytotoxic in this setting: prolonged CHOP expression biases Schwann cells toward an apoptotic/dysfunctional fate rather than recovery, resulting in failure of proper myelination and a profound hypomyelination.

Examples of this mechanism are provided by the p.Ser63del and p.Arg98Cys mutations. Preclinical mouse models expressing these specific mutants faithfully replicate the human disease, exhibiting severe, early-onset demyelinating neuropathy. Schwann cells in these mice show massive accumulation of the mutant MPZ protein within a distended ER, accompanied by the robust activation

of all three UPR pathways. Genetic ablation of Chop in the P0S63del mouse model provides eliminates this key pro-apoptotic effector dramatically rescues motor function and substantially reduces demyelination[95]. This finding establishes that in these severe cases, it is not merely the absence of functional MPZ, but the toxic cellular response to the mutant protein that is the principal driver of the disease.

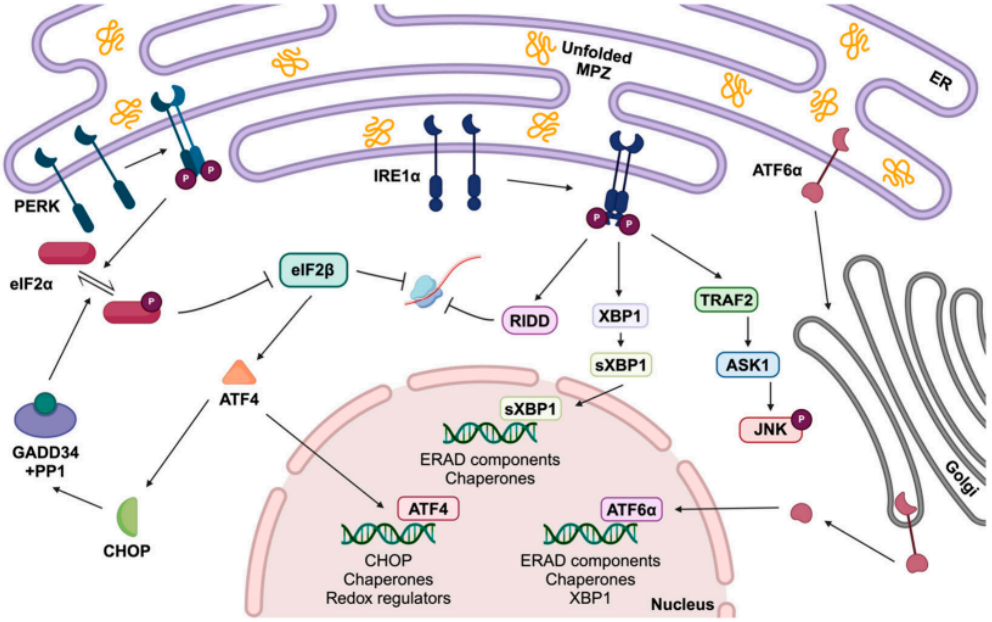

Figure 8 UPR in demyelinating CMT caused by Unfolded MPZ[100]

Disruption of Adhesive Function: Impaired Myelin Compaction

A second, distinct pathogenic mechanism arises from mutations that do not cause gross protein misfolding or ER retention but instead subtly disrupt the homophilic adhesion, i.e. exquisite structural interfaces required for MPZ's primary function As the most abundant protein in the PNS myelin sheath, MPZ acts as the principal "molecular glue," zipping adjacent layers of the Schwann cell membrane together to form the compact myelin structure. This adhesion is mediated by the homophilic binding of the extracellular Ig-like domains of MPZ molecules residing on opposing membrane surfaces, which forms the electron-dense IPL visible in electron micrographs

The precise molecular architecture of this adhesive interface is an area of active structural research, with several models proposed to explain how MPZ molecules organize to generate the robust adhesive force required for myelin compaction. These models are based on a combination of X-ray crystallography, cryo-electron microscopy, and solution-state biophysical studies. As discussed above, a key concept within this framework is the distinction between cis-interactions, which occur between MPZ molecules within the plane of a single membrane, and trans-interactions, which bridge two apposing membranes.

Regardless of the precise configuration, the integrity of these specific protein-protein interfaces is of paramount importance for strong adhesion. Pathogenic mutations located on the surface of the Ig domain, particularly at residues predicted to be part of these cis or trans interaction surfaces, can abolish or weaken these homophilic bonds.Unlike the core-destabilizing mutations that trigger the UPR, these surface variants often permit the protein to fold correctly and traffic to the cell surface. However, once there, the mutant protein is functionally incompetent as an adhesion molecule. This results in the formation of a myelin sheath that is poorly compacted, structurally unstable, and prone to lamellar splitting and secondary degeneration over time. This structural failure, rather than cellular toxicity, underlies the pathology. Since a structurally weak myelin sheath may be sufficient for function in early life, the clinical consequences of impaired adhesion often manifest as a more slowly progressive, later-onset neuropathy, characteristic of classic CMT1B or the axonal forms, CMT2I/J.2

Haploinsufficiency and Loss-of-Function Mechanisms

The third pathogenic mechanism is haploinsufficiency, a classic loss-of-function scenario. This occurs when one of the two MPZ alleles is rendered non-functional, for instance, by a nonsense mutation that introduces a premature stop codon or a frameshift mutation, that lead to the degradation of the mutant mRNA transcript through a cellular surveillance pathway known as nonsense-mediated decay[94]. The consequence is that the Schwann cell produces functional, wild-type MPZ protein from only one allele, resulting in an approximately 50% reduction in the total amount of the protein.

This 50% dosage of MPZ appears to be largely sufficient for the initial process of developmental myelination, allowing for the formation of a relatively normal myelin sheath in early life.This stands in stark contrast to the complete absence of MPZ, as seen in homozygous Mpz-knockout mice, which suffer from a severe, congenital failure of myelin compaction. However, while half the normal amount of MPZ can build the sheath, it is often insufficient for its long-term maintenance and structural integrity over the course of a human lifespan. The myelin sheath is a dynamic structure; it requires continuous metabolic support and structural reinforcement from the Schwann cell. A reduced quantity of its primary structural protein renders the sheath more vulnerable to age-related stresses and mechanical wear-and-tear.

This dosage-dependent requirement for long-term stability is strongly supported by preclinical evidence from heterozygous Mpz knockout mice (Mpz+/-). These animals, which produce approximately 50% of the normal level of MPZ, develop a mild, slowly progressive, late-onset neuropathy characterized by demyelination and axonal loss, closely mirroring the human haploinsufficiency phenotype.3 Clinically, human patients with heterozygous null alleles typically present with the mildest end of the MPZ phenotypic spectrum, often with a late-onset neuropathy.3 This mechanism underscores a critical biological principle: the absolute quantity of MPZ is a limiting factor not just for building myelin, but for preserving its integrity and the health of the axon-myelin unit over many decades.

1.4.4 Genotype-Phenotype Correlations

The existence of distinct molecular pathomechanisms provides a powerful framework for understanding the strong genotype-phenotype correlations that are a hallmark of MPZ-related neuropathies. The clinical outcome—be it severe infantile dysmyelination, classic childhood-onset demyelination, or late-onset axonal degeneration—is largely determined by the specific molecular defect caused by the underlying mutation. The location of the mutation within the protein's structure is a key predictor of its pathogenic consequence and, therefore, its clinical phenotype[79]. This has led to the development of a robust model that

categorizes variants as either "destabilizing" or "non-destabilizing," which correlates strongly with disease severity and age of onset.
The prevailing paradigm distinguishes between mutations based on their impact on the structural integrity of the MPZ protein[101].

Destabilizing Core Variants.

Pathogenic missense mutations located within the hydrophobic core of the Ig-like domain tend to be structurally destabilizing. These variants disrupt the intricate network of interactions required for the protein to achieve its correct three-dimensional fold. This leads to protein misfolding, retention in the ER, and chronic activation of the cytotoxic arms of the UPR[101]. This toxic gain-of-function mechanism profoundly disrupts Schwann cell biology during the critical period of developmental myelination. Consequently, these core-destabilizing variants are strongly associated with the most severe, early-onset demyelinating phenotypes, such as DSS and infantile-onset CMT1B[102].

Non-Destabilizing Surface Variants.

In contrast, missense mutations that occur on the surface of the Ig-like domain often do not compromise the overall stability or folding of the protein. Instead, these variants are frequently located at the specific interfaces required for MPZ's homophilic oligomerization—the cis-tetramer or trans-dimer interactions[101]. By altering key residues at these binding surfaces, the mutations impair the protein's adhesive function without triggering a significant UPR. This leads to the formation of a structurally compromised and unstable myelin sheath. The resulting pathology is one of chronic, low-grade demyelination or a failure of long-term axonal support. This mechanism corresponds to the milder, later-onset clinical phenotypes, including classic childhood-onset CMT1B and the adult-onset axonal forms, CMT2I/J[103].

This model provides a clear, structure-based rationale for the clinical spectrum. Mutations inside the protein cause a toxic folding problem leading to early, severe

disease, while mutations on the surface of the protein cause a structural adhesion problem leading to later, milder disease.

Further supporting this correlation, computational tools can be used to predict the impact of a novel missense variant on the thermodynamic stability of the MPZ protein. These in silico methods calculate the change in Gibbs free energy of folding caused by the amino acid substitution[104,105]. Studies have shown that a more negative value, which indicates greater structural destabilization, significantly correlates with an earlier age of onset and greater clinical severity as measured by standardized clinical scales. While not perfectly predictive for every variant, this quantitative approach provides a valuable tool for prognostic counseling and for stratifying patients in future clinical trials.

However, despite the power of this structure-function model, establishing a definitive genotype-phenotype correlation for every MPZ variant remains a significant challenge. The clinical spectrum is a continuum, and some mutations produce intermediate or atypical phenotypes that do not fit neatly into these categories. Furthermore, the predictive value of in silico tools is not absolute, and exceptions exist where the predicted structural impact does not perfectly align with the observed clinical severity. This highlights the complexity of the underlying pathobiology and suggests that other genetic or environmental modifiers may influence the final clinical outcome. Therefore, a comprehensive understanding of how each specific mutation affects MPZ protein structure, stability, and function is still lacking.

This gap in knowledge underscores the critical need for further experimental investigation into a wider array of pathogenic variants, which is essential for refining predictive models, improving patient counseling, and ultimately developing targeted, mutation-specific therapies.

1.5 Aims of the Thesis

The primary objective of this PhD thesis is to investigate the molecular mechanisms by which point mutations in the MPZ_{ex} lead to CMT disease. This work is principally guided by the identification of the novel D134V mutation, which has been clinically associated with a severe, childhood-onset CMT1B

phenotype. The study is divided into two main parts, followed by a functional investigation.

In the first part of this thesis (Section 3.1), we shall focus on the comprehensive characterization of the novel D134V mutant. We aim to define the specific molecular defects imparted by this mutation, which is hypothesized to be responsible for its severe clinical outcome. To this end, the D134V MPZ_{ex} protein was generated by site-directed mutagenesis, expressed, and purified. The structural integrity of this variant, together with its conformational signatures, and thermodynamic stability will be characterized in detail using a combination of biophysical techniques, including nuclear magnetic resonance, fluorescence spectroscopy, circular dichroism (CD), and dynamic light scattering (DLS), complemented by thermal and chemical denaturation assays.

In the second part of this thesis (Section 3.2), we shall expand our investigation to a broader panel of pathogenic mutations (namely I30M, R36G, H39P, H81Q, H81L, N122S, N131Y and D134E,) to establish a comparative framework. The rationale of this mutagenic analysis is that the selection of CMT-associated point mutations affecting protein positions that exhibit different structural features, such as solvent exposure, secondary structure and/or are associated to different CMT clinical phenotypes, in terms of severity of symptoms and onset, allows the possibility to identify and establish correlations between structural perturbations and pathological phenotype. This panel will be subjected to the same biophysical pipeline used for D134V, so that the results can be quantitatively compared. The final goal of this experimental plan is to compare how different mutations, which lead to varied clinical phenotypes, differentially alter the biophysical and structural properties of the MPZ_{ex} domain relative to both the wild-type protein and the severe D134V variant.

Finally, we will investigate the functional consequences of this entire panel of mutations on MPZ_{ex} molecular interactions. We will employ fluorescence-based assays to quantitatively assess the impact of each mutation on both the homophilic interactions of MPZ_{ex} (critical for myelin compaction) and its heterophilic interactions with PMP22.

The ultimate aim of this work is to correlate specific, mutation-induced alterations in protein stability, folding, and binding affinity with their associated pathological phenotypes. By elucidating the distinct molecular principles governing the etiopathogenesis of different CMT-causing mutations, this research seeks to provide a clearer understanding of the disease and potentially contribute to the prediction of phenotype and disease progression based on genotype.

1.5.1 Rationale for the Selection of Pathogenic MPZ Variants

The purpose of this section is to provide a detailed scientific rationale for the selection of a panel of eight pathogenic MPZ variants (Figure9): I30M, R36G, H39P, H81L, H81Q, N122S, N131Y, and D134E. This panel has been assembled to serve as a comparative framework, for contextualizing the novel D134V variant, which is the main subject of this PhD thesis.

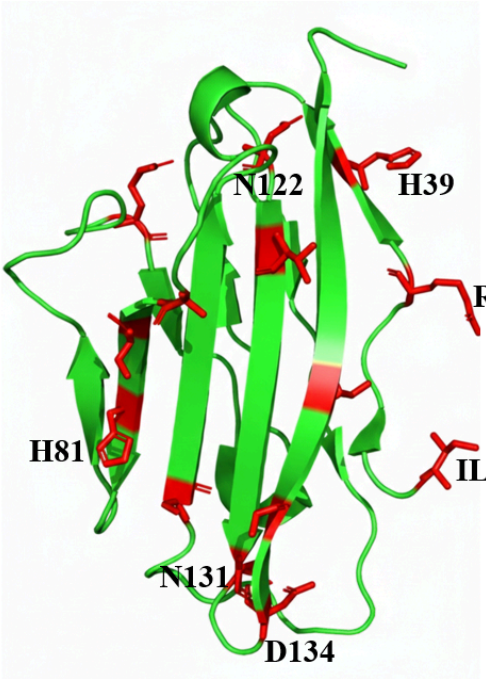

Figure 9. Structural mapping of selected pathogenic MPZ variants.

Below we summarize each mutation's CMT subtype, prevalence, and structural context:

- I30M mutation, located in β-strand B, is associated with severe clinical phenotypes, classified as early-onset CMT1B or DSS. Although rare, it has been

reported in at least two Chinese families with an age of onset under 2 years[106]. Computational studies on the adjacent pathogenic mutation I30T have predicted that alterations at this position induce significant conformational and dynamic changes in the protein[107].

- R36G variant is located in β-strand A and it is associated with a CMT2 with a very late onset, characterized by rapid progression and prominent neuropathic pain[108].This mutation, reported in a single family, shows an intra-familial phenotypic variability with the proband's son showing a predominantly demyelinating picture.
- The H39P pathogenic variant in the MPZ gene has previously been reported in several unrelated individuals with late-onset neuropathy (CMT1B/CMT2)[75,109]. The variant was also identified in a family of ten individuals with hereditary motor and sensory neuropathy and was absent in two hundred control individuals[110]. Functional studies suggest that the H39P variant may result in partial loss of function[52].
- H81Q and H81L are two allelic variants, affecting the same residue 81 in β-strand C'. H81Q is associated with a severe, early-onset demyelinating CMT1B, as documented in a Korean family[111]. H81L, in contrast, is associated with a milder, adult-onset CMT2 phenotype, described in a Chinese family[112].
- N122S is located in the EF loop. Its importance lies in the fact that the substitution of asparagine (N) with serine (S) abolishes the only N-glycosylation site of MPZ. This variant is associated with CMT1B with onset in childhood or adolescence.
- N131Y is located in β-strand F and this variant has been reported in a case of severe, infantile-onset demyelinating neuropathy[113]. The presence of other pathogenic mutations at the same codon, such as N131K, suggests that this residue is structurally or functionally critical, perhaps participating in one of the adhesion interfaces[114].
- D134E is located in the FG loop. This mutation is of strategic importance for this thesis, as it is at the same residue as the variant of interest, D134V. It is associated with early-onset CMT1B. More specific data report two cases with onset at less than 1 and 4 years of age, both with a demyelinating phenotype (CMT1)[115]. Its inclusion is crucial for direct allelic comparison. The D134E substitution is

chemically conservative (an acidic amino acid replaced by another acidic amino acid), while the D134V substitution is non-conservative (an acidic amino acid replaced by a hydrophobic amino acid).

The following table 2 summarizes the clinical, structural, and prevalence characteristics of the selected variants, highlighting the comparative logic behind their choice.

Mutation	**Disease Classification**	**Age of Onset**	**Salient Phenotypic Features**	**Structural Location**	**Prevalence/Reported Cases**
I30M	CMT1B/DSS	Early (<2 years)	Severe, demyelinating	N-terminus, β-strand B	2 families
R36G	CMT2	Late (77 years)	Axonal, rapid progression, painful	N-terminus, β-strand A	1 family
H39P	CMT1B/CMT2	Late	Mixed demyelinating/axonal, hearing loss	N-terminus, β-strand A	Numerous individuals/families
H81L	CMT2	Adult	Axonal, mild	Core, β-strand C'	1 family
H81Q	CMT1B	Early	Severe, demyelinating	Core, β-strand C'	1 family
N122S	CMT1B	Childhood/Adolescence	Demyelinating, loss of glycosylation site	Loop EF	1 reported case

N131Y	CMT1B	Early (2 years)	Severe, demyelinating	β-strand F	1 reported case
D134E	CMT1B	Early (<4 years)	Severe, demyelinating	Loop FG	2 reported cases

Table 2. Clinicopathological and Structural Characteristics of Selected MPZ Variants.

2. Materials and Methods

2.1 General Methods for Protein Production and Basic Characterization

2.1.1 Mutagenesis

All mutants were generated using a previously engineered pQE-30 expression vector (3500 bp), which contains the sequence encoding the wild-type MPZ_{ex}, as a template. This vector provides a Lac promoter for inducible expression, an ampicillin resistance gene for selection, an N-terminal six-histidine (His) tag, and a thrombin cleavage site upstream of the MPZ_{ex} insert.

Site-directed mutagenesis was performed using the Q5 Site-Directed Mutagenesis Kit (New England Biolabs, NEB). Briefly, the wild-type pQE-30-MPZ_{ex} plasmid was first extracted from overnight cultures of XL1-Blue E. coli using the GeneJET Plasmid Miniprep Kit (Thermo Scientific™). The mutagenesis PCR (25 µL total volume) was assembled using 12.5 µL of 2X Q5 Master Mix, 1.0 µL of plasmid template, and 1.25 µL each of the specific forward and reverse primers designed using NEBaseChanger™ (NEB). The thermal cycling protocol was: initial denaturation at 98°C for 30s; followed by 25 cycles of 98°C for 10s, annealing at 62-70°C (primer-dependent) for 30s, and 72°C for 1 min; and a final extension at 72°C for 2 min.

Following amplification, the PCR product was treated with the KDL enzyme mix (5 min at room temperature) to circularize the plasmid. 5 µL of the ligation product was then transformed into NEB 5-alpha competent E. coli via heat shock (42°C for 30s). Cells were recovered in SOC medium (1h at 37°C) and plated on LB-Agar containing 0.1 mg/mL ampicillin. For each mutant, 10 colonies were selected, grown in liquid culture, and the plasmids extracted. The presence of the desired mutations was confirmed by Sanger sequencing (BMR Genomics, Padua, Italy). Finally, sequence-verified mutant plasmids were transformed into XL1-Blue E. coli for protein expression.

2.1.2 Protein expression and purification

Wild-type and mutant MPZ_{ex} proteins were expressed in XL1-Blue E. coli. An overnight starter culture (50 mL LB + ampicillin) was used to inoculate 950 mL of LB medium. Cultures were grown at 37°C with agitation until the optical density at 600 nm reached a value of 0.8. Protein expression was then induced by adding isopropyl-β-D-1-thiogalactopyranoside (IPTG) to a final concentration of 0.5 mM. Expression proceeded for 3 hours at 37°C. After expression, cells were harvested by centrifugation (6790 g, 30 min, 4°C), and the cell pellet was resuspended in 50 mL of PBS (50 mM Na2HPO4, 150 mM NaCl, pH 7.3) and stored at -20°C.

The MPZ_{ex} protein was expressed in inclusion bodies (IBs). The thawed cell suspension was lysed by sonication on ice (4 min total; 20s on, 20s off cycles at 100% amplitude). IBs were pelleted by centrifugation (20,300 g, 30 min, 4°C). The pellet was subjected to three sequential washes (resuspension followed by centrifugation) with:

50 mM Tris-HCl, 1% Triton, pH 8.0

50 mM Tris-HCl, 2 M NaCl, pH 8.0

50 mM Tris-HCl, pH 8.0

The washed IBs were solubilized in 100 mL of Buffer A (50 mM Tris-HCl, 8 M Urea, 0.2 M NaCl, 10 mM imidazole, 1 mM beta-Mercaptoethanol, pH 8.0). The solubilized protein was purified by immobilized metal affinity chromatography (IMAC) using a HisPur™ Ni-NTA column (ThermoFisher Scientific™) equilibrated in Buffer A. The flow-through was applied to the column five times. The column was washed with Buffer B (Buffer A with 25 mM imidazole) to remove impurities, and the His-tagged protein was eluted with Buffer C (Buffer A with 250 mM imidazole).

The purified, denatured protein was refolded by dropwise addition (1:20 dilution ratio, 2 mL/h) into an ice-cold refolding buffer (20 mM Tris-HCl, 200 mM NaCl, 0.6 M GndHCl, 0.4 M arginine, 0.5 M sucrose, 0.1% Triton X-100, 1 mM EDTA, 0.1 mM GSSG, 1 mM GSH, pH 8.0), stirring overnight at 4°C.

The refolded protein solution was concentrated to 50 mL using ultrafiltration (3 kDa MWCO). The concentrated solution was dialyzed overnight at 4°C against 20 mM Tris-HCl (pH 8). A final purification step was performed using anion-exchange chromatography (IEX) on an ÄKTA pure™ FPLC system with a HiTrap™ Q FF 5 mL column. The protein was eluted using a linear gradient of Buffer B (20 mM Tris-HCl pH 8, 1 mM DTT, 1 M NaCl). Fractions containing the protein, identified by monitoring 280 nm UV signal, were pooled, and the final concentration of the refolded protein was determined spectrophotometrically.

2.1.3 Far-UV CD spectroscopy

Prior to each of the following analyses, the MPZ_{ex} sample underwent centrifugation at 18,000× g for 15 minutes at 4 °C, and was then diluted to achieve a final concentration of 0.2 mg/mL. Far-UV CD spectra were collected at 25 °C spanning the range of 190 to 250 nm, utilizing a 0.1 mm path length quartz cuvette. Measurements were conducted on a Jasco J-810 spectropolarimeter (Tokyo, Japan), which was outfitted with a thermostated cell holder linked to a Thermo Haake C25P water bath (Karlsruhe, Germany). Spectral acquisition parameters included a 1 nm data pitch, a scan rate of 20 nm/min, a 2-second response time, and a 1 nm bandwidth. The protein was dissolved in a buffer comprising 20 mM Tris, 100 mM NaCl, and 1 mM DTT, adjusted to pH 8. Subsequent to data collection, spectra were baseline-corrected by subtracting the buffer blank. Data points were excluded when the high tension (HT) signal exceeded 700 V. All spectra were then converted to mean residue ellipticity [θ], according the following formula:

$$[\theta] = \frac{\vartheta \cdot MW}{10 \cdot n \cdot l \cdot c}$$

where ϑ is the signal measured, MW is the molecular weight in g mol^{-1}, n is the number of residues, l is the length of the cuvette in cm and c is the concentration in g/L.

2.1.4 Intrinsic fluorescence spectroscopy

Intrinsic fluorescence spectra of protein samples were acquired using an Agilent Cary Eclipse spectrofluorimeter (Agilent Technologies, Santa Clara, CA, USA).

Proteins were analyzed at a concentration of 0.2 mg/mL in a 3x3 mm quartz cuvette. Measurements were taken at 25 °C, with an excitation wavelength set to 280 nm. Emission spectra were recorded from 300 to 460 nm. Both excitation and emission slits were fixed at 5 nm, and the photomultiplier tube (PMT) voltage was set to 800 V. All spectra were blank-subtracted, using a buffer comprising 20 mM Tris, 100 mM NaCl, and 1 mM DTT, adjusted to pH 8 as blank.

2.1.5 Acrylamide Quenching Experiment

To perform quenching experiments, a solution of protein was prepared at a concentration of 0.02 mg/mL in a buffer containing 20 mM Tris-HCl, 100 mM NaCl, and 1 mM DTT, pH 8. A 2.5 M acrylamide solution was also prepared using the same buffer. One mL of the protein solution was placed in a 1 mL 4x10 mm quartz cuvette, and its intrinsic fluorescence was measured using an Agilent Cary Eclipse spectrofluorimeter (Agilent Technologies, Santa Clara, CA, USA), which was equipped with a thermostated cell holder attached to an Agilent PCB 1500 water Peltier system. The spectrofluorometer settings included an excitation wavelength of 280 nm, an emission range from 300 to 500 nm, excitation and emission slits set to 5 nm, a photomultiplier tube (PMT) voltage of 800 V, and a scan speed of 120 nm/min. For each data point, 3 accumulations were averaged. The fluorescence was monitored at 25 °C. The experiment involved 15 sequential additions of 5 µL acrylamide to the cuvette, with a fluorescence spectrum recorded after each addition. Each spectrum's total fluorescence was adjusted for dilution due to the added acrylamide. Quenching data were subsequently evaluated using the Stern-Volmer equation:

$$\frac{F_0}{F} = 1 + K_{SV} \cdot [Q]$$

In this equation, F_0 and F denote the integrated fluorescence intensities (300–500 nm) in the absence and presence of acrylamide, respectively; K_{SV} is the Stern-Volmer constant; and [Q] is the quencher (acrylamide) molar concentration in the cuvette.

2.1.6 Guanidine Hydrochloride (GndHCl)-Induced Denaturation

For chemical denaturation, twenty samples were prepared, each containing protein at a concentration of 0.1 mg/mL in 20 mM Tris-HCl, 100 mM NaCl, 1 mM DTT, pH 8, with varying concentrations of guanidinium hydrochloride (GndHCl). Far-UV CD signals were then measured at 222 nm for each sample, using a slit of 10 nm. Data were acquired at 25 °C over 360 seconds, with readings taken every 5 seconds. The CD signals were plotted Vs GndHCl concentration, and the resulting denaturation curves were fitted to the model described by Santoro and Bolen (1988), according to the following equation:

$$\vartheta = \frac{\left(\vartheta_F^{H2O} + a_1 \cdot [GndHCl]\right) + \left(\vartheta_U^{H2O} + a_2 \cdot [GndHCl]\right) \cdot exp\left(-\frac{\Delta G_{U-F}^{H2O} - m \cdot [GndHCl]}{R \cdot T}\right)}{1 + exp\left(-\frac{\Delta G_{U-F}^{H2O} - m \cdot [GndHCl]}{R \cdot T}\right)},$$

where $[GndHCl]$ is the concentration of guanidine hydrochloride, ϑ_F^{H2O} and ϑ_U^{H2O} are the CD signals in the absence of denaturant respectively for folded and unfolded protein, a_1 and a_2 are the slopes of the straight lines observed at denaturant concentrations lower and higher than the transition zone, respectively. ΔG_{U-F}^{H2O} represents the free energy change upon denaturation ΔG_{U-F} obtained in the absence of denaturant, m is the dependence of ΔG_{U-F} on the denaturant concentration. Best fits of experimental data to this equation give a quantitative measurement of ΔG_{U-F}^{H2O} and m. Furthermore, using the fit output, one can calculate the concentration of middle denaturation C_m as the denaturant concentration value at which $K_U = \frac{[U]}{[F]} = 1$ and, consequently, in a two-state model, $\Delta G_{U-F} = 0$. That is, from the equation above, we obtain that

$$C_m = \frac{\Delta G_{U-F}^{H2O}}{m}.$$

When necessary for our analysis, the equilibrium denaturation curves obtained experimentally were also normalised to the fraction of folded protein ff, calculated as follows:

$$ff = \frac{[F]}{[F]+[U]} = \frac{\vartheta - \left(\vartheta_U^{H2O} + a_2 \cdot [GndHCl]\right)}{\left(\vartheta_F^{H2O} + a_1 \cdot [GndHCl]\right) - \left(\vartheta_U^{H2O} + a_2 \cdot [GndHCl]\right)}$$

2.1.7 Differential Scanning Fluorimetry (DSF)

DSF experiments were carried out using a Bio-Rad CFX 7500 Real-Time PCR system, employing the fluorescein amidite filter for signal detection. Protein samples were prepared at a final concentration of 0.2 mg/mL in a buffer composed of 20 mM Tris-HCl, 100 mM NaCl, 1 mM DTT, pH 8. A Sypro Orange fluorescent dye (Thermo Fisher Scientific) was added to a final nominal concentration of 5X. The reaction mixture for each well totaled 50 µL and was dispensed into a 96-well MicroAmp Fast Optical PCR plate, subsequently sealed with a MicroAmp adhesive film (Thermo Fisher Scientific). Thermal denaturation was initiated by a heating ramp, during which Sypro Orange fluorescence was continuously monitored. The temperature protocol began with a 5-minute hold at 25 °C, followed by a linear increase from 15 °C to 95 °C at a ramp rate of 1 °C per minute. All samples were prepared in triplicate. The melting temperature (T_m), representing the temperature value at which half of the protein population has denatured, was subsequently determined from the fraction of unfolded protein at various temperatures was derived by comparing the observed fluorescence signal to the fluorescence of the fully native and fully denatured states, which were established from the initial and final linear baselines of the melting curve.

2.1.8 DLS

The aggregation time course of wild-type and mutant MPZex were monitored by DLS. Measurements were performed using a Zetasizer Nano instrument (Malvern Panalytical). For the analysis, protein stock solutions were diluted to a final concentration of 0.2 mg/mL in 20 mM Tris-HCl, 100 mM NaCl buffer. A 50 µL volume of the protein solution was clarified by filtration through a Whatman® Anotop® syringe filter (0.02 µm pore size) directly into a measurement cuvette. DLS measurements were acquired immediately after filtration (t=0) and subsequently after 24 hours and 48 hours. Between time points, the samples were kept at room temperature.

2.1.9 Heterophilic binding pull down assay

To investigate the heterophilic interaction between MPZ_{ex} and PMP22, a synthetic 14-amino acid peptide corresponding to the second extracellular domain of PMP22 (PMP22ex) was utilized. The peptide's sequence, [-H-Arg-His-Pro-Glu-Trp-His-Leu-Asn-Ser-Asp-Tyr-Ser-Tyr-Gly-OH-], was selected based on prior studies demonstrating its interaction with MPZ_{ex} [116,117].

The PMP22ex peptide was dissolved in a 100 mM bicarbonate buffer, pH 8.0, at a concentration of 1 mg/mL and subsequently labeled with the fluorescent probe Alexa Fluor 594. A 1:10 molar ratio of protein to probe was used to ensure efficient labeling and that each PMP22ex molecule was tagged with Alexa Fluor 594 (PMP22exAlexa594).

For the pulldown assay, 100 µL aliquots of MPZ_{ex} wild-type or its mutants were immobilized separately on 250 µL of HisPur™ Ni-NTA resin in 10 mL columns, at a concentration of 0.1 mg/mL. After immobilization, 1.25 nmol of PMP22exAlexa594 peptide was added to each tube. The samples were incubated for 30 minutes at room temperature to allow for interaction between MPZ_{ex} and the peptide. The resin was then washed five times with 1 mL of 100 mM NaCl, 100 mM Na2HPO4 buffer, pH 7.5, to remove unbound peptide. Finally, MPZ_{ex} was eluted with 500 µL of the same buffer containing 200 mM imidazole. A control column containing only the resin, subjected to the identical procedure but without immobilized protein, was included in each experiment to confirm that PMP22exAlexa594 did not bind non-specifically to the resin. Each experiment was performed in triplicate for every mutant.

Fluorescence spectra were acquired using a Cary Eclipse fluorimeter, with an excitation wavelength (λexc) of 535 nm, corresponding to the maximum absorption of the Alexa Fluor 594 probe. Emission was recorded over the range of 600-700 nm. Both excitation and emission slits were set to 5 nm, and the PMT voltage was fixed at 800V.

Data were processed calculating the total emitted fluorescence of each sample and subtracting the control signal, obtained for the sample with no immobilized protein, from the signal obtained from the sample under scrutiny.

2.1.10 Homophilic binding pull down assay

To investigate the homophilic binding of MPZ_{ex}, the HisTag was first removed from MPZ_{ex} wild-type by overnight thrombin digestion at 4 °C with agitation in 20 mM Tris-HCl, 100 mM NaCl buffer. The sample was then centrifuged to remove any aggregates, and the supernatant containing the HisTag-free MPZ_{ex} wild-type was collected. A buffer exchange was subsequently performed by dialysis into 100 mM NaCl, 100 mM Na_2HPO_4 buffer, pH 7.5, to optimize the solution conditions and achieve maximum fluorescent labeling.

The concentration of HisTag-free MPZ_{ex} wild-type was determined spectrophotometrically. The protein was then labeled with the fluorescent probe BODIPY™ at a protein:probe molar ratio of 1:10 to ensure efficient and complete labeling of MPZ_{ex} with BODIPY™ (MPZ_{ex}-BODIPY™).

For the binding assay, 250 µL of HisPur™ Ni-NTA resin was added to 10 mL columns. One hundred microliters of unlabeled MPZ_{ex} wild-type or its mutants were immobilized on separate aliquots of resin at a concentration of 0.1 mg/mL. Subsequently, 500 µL of MPZ_{ex}-BODIPY™ at a concentration of 0.06 mg/mL was added to the tubes and incubated with the resin for 30 minutes at room temperature to allow for protein-protein interaction. Following incubation, the resin was washed five times with 1 mL of 100 mM NaCl, 100 mM Na2HPO4 buffer, pH 7.5, to remove unbound labeled protein. Finally, the immobilized protein was eluted with 500 µL of the same buffer containing 200 mM imidazole. A control column containing only the resin, subjected to the identical procedure but without immobilized protein, was included in each experiment to confirm that MPZ_{ex}-BODIPY™ did not bind non-specifically to the resin. Each experiment was performed in triplicate for every mutant and the results of the three measurements were averaged.

Fluorescence spectra were acquired using a Cary Eclipse fluorimeter, with an excitation wavelength (λexc) of 540 nm, corresponding to the maximum absorption of the BODIPY™ probe. Emission was recorded over the range of 560-640 nm. Both excitation and emission slits were set to 5 nm, and the PMT voltage was fixed at 800V. Even in this case, data were processed calculating the

total emitted fluorescence of each sample and subtracting the control signal, obtained for the sample with no immobilized protein, from the signal obtained from the sample under scrutiny.

2.2 In-depth Biophysical Characterization of wild-type and D134V

2.2.1 Fourier Transform Infrared (FTIR) Spectroscopy

FTIR spectroscopy was performed on MPZ_{ex} wild-type and D134V protein samples , at a concentration of 0.2 mg/mL in H_2O. A few small drops of the sample solution were placed directly onto the crystal of a QATR-S single-reflection ATR accessory and left to dry to form a thin film.

FTIR spectra were obtained using a Shimadzu IRSpirit Fourier transform infrared spectrophotometer (Shimadzu, Kyoto, Japan) equipped with the ATR accessory. The background signal was acquired from the clean, dry ATR crystal prior to sample application. Spectra were collected in the range from 4000 cm^{-1} to 450 cm^{-1} . For comparative analysis, the resulting spectra were normalized and focused on the Amide I band (1700 cm^{-1} – 1600 cm^{-1}), which is sensitive to the protein secondary structure conformation.

2.2.2 Nuclear Magnetic Resonance Spectroscopy

To prepare samples for NMR analysis, isotopically labeled ^{15}N-MPZ_{ex} (Wild-Type and D134V) was produced. Transformed E. coli XL-Blue cells were grown in M9 minimal medium supplemented with $^{15}NH_4Cl$ (1 g/L; Cambridge Isotope Laboratories) as the sole nitrogen source. Protein expression was induced with 0.5 mM IPTG, and the ^{15}N-labeled protein was purified from inclusion bodies using the affinity chromatography and refolding protocol described in Section 2.2.

For analysis, the final purified protein samples were diluted with 10% (v/v) D_2O for the frequency lock. The final protein concentrations were 77 µM for wild-type and 55 µM for D134V. 500 µL of each sample was transferred to a 5 mm high-precision NMR tube.

[^{1}H, ^{15}N]-HSQC (Heteronuclear Single-Quantum Correlation) spectra were acquired at 277 K (4°C) on a Bruker AVANCE 700 MHz spectrometer. All NMR experiments were performed at the University of Naples Federico II, in collaboration with Prof. Alfonso De Simone. The acquired spectra were analyzed using Sparky (T. D. Goddard and D. G. Kneller, UCSF).

2.2.3 Acid-induced denaturation

To evaluate the pH stability of MPZ_{ex}, samples were prepared at a concentration of 0.1 mg/mL in a series of buffers across a broad pH range. The buffers used, each at a 10 mM concentration with a total ionic strength adjusted to 30 mM using NaCl, included: citrate (pH 2.2-2.8), formate (pH 2.9–3.9), acetate (pH 3.9–5.6), MES (pH 5.6–6.5), phosphate (pH 6.5–7.5), Tris (pH 7.5–8.8), and borate (pH 8.8–10.0). All buffers were purchased from Sigma-Aldrich.

The far-UV CD signal was measured for each sample. Specifically, the CD signal at 222 nm was recorded over 360 seconds, with data points acquired every 5 seconds, using a Jasco J-810 spectropolarimeter. The slit was set to xxx.This wavelength was chosen for its sensitivity to secondary structure changes, as observed in previous denaturation experiments. The resulting CD signals were then plotted as a function of pH.

2.2.4 Light scattering

To assess the aggregation kinetics of wild-type and D134V mutant MPZ_{ex}, Dynamic Light Scattering (DLS) and Nanoparticle Tracking Analysis (NTA) were employed. All buffers and solutions were prepared using ultrapure Milli-Q water. Protein stock solutions were first clarified by centrifugation at 14,000×g for 5 minutes at 4 °C.

For DLS measurements at time zero, protein samples were diluted to a final concentration of 0.2 mg/mL in 20 mM Tris-HCl, 100 mM NaCl, pH 8.0 . The solution was then filtered through a Whatman® Anotop® syringe filter with a 0.02 µm pore size. Immediately following filtration, 50 µL of the sample was loaded into a cuvette, and measurements were performed using a Zetasizer Nano instrument (Malvern Panalytical).

For analysis after 24 hours, the samples prepared as above were incubated at room temperature. The aggregation state was then characterized by NTA using an NS300 instrument (Malvern Panalytical). Prior to measurement, samples were diluted 25- to 100-fold with ultrapure Milli-Q water to reach the optimal particle concentration range for analysis. NTA measurements provided the concentration and size distribution of the protein aggregates.

2.2.5 Size Exclusion Chromatography - Multi-Angle Light Scattering (SEC-MALS)

To determine the absolute molar mass and oligomeric state of the wild-type and D134V MPZ_{ex} variants, SEC-MALS analysis was performed.This analysis was conducted in collaboration with the Department of Biomedicine, University of Bergen, Norway.

The measurements were carried out on previously concentrated and frozen protein samples.The instrumental setup consisted of a Shimadzu Prominence-I LC-2030C HPLC system equipped with a Superdex 75 increase 10/300GL column. The column was maintained at room temperature, while the HPLC sample chamber was thermostatted at 5°C.

The mobile phase, used for both column equilibration and analytical runs, consisted of 20 mM Tris-HCl, 100 mM NaCl, pH 8.0, which was previously 0.1 µm-filtered. For each analysis, 100 µL of the protein sample was injected. The specific concentrations injected were 0.37 mg/mL for MPZ_{ex} wild-type and 0.24 mg/m for the D134V variant. The separation was conducted at a constant flow rate of 0.5 mL/min, with an acquisition time of 50 minutes per run.

Elution signals were monitored in-line using a Wyatt miniDAWN TREOS MALS system and an ERC RefractoMax 520 refractive index (RI) detector. Data analysis was performed by manually aligning the Light Scattering (LS) and RI signals. The RI signal was used as the concentration source for the molar mass calculation.

2.2.6 NMR binding assay

To investigate the heterophilic interaction between MPZ_{ex} and PMP22, NMR binding experiments were performed by monitoring Chemical Shift Perturbations (CSP) in the [^{1}H, ^{15}N]-HSQC spectra of the ^{15}N-labeled proteins upon the addition of an unlabeled PMP22ex peptide.

The PMP22ex was first dialyzed extensively against the NMR buffer (e.g., 20 mM TrisHCl, 100 mM NaCl, pH 8.0) to ensure buffer compatibility.

For the binding assay, the unlabeled PMP22ex was added to the ^{15}N-labeled MPZ_{ex} wild-type (77 µM) and ^{15}N-labeled D134V (55 µM) samples. The peptide was added to a single final concentration representing a 1:10 (protein:peptide) molar ratio.

[^{1}H, ^{15}N]-HSQC spectra were acquired for both samples in the presence of the peptide, using the same parameters and conditions previously described (277 K, Bruker AVANCE 700 MHz spectrometer).

Chapter 3. Biophysical and Structural Characterization of the Novel D134V Mutant

3.1 Results

The first part of the present experimental work involved the biophysical characterization of the D134V mutation of MPZ_{ex}, recently identified and associated with a case of severe, childhood-onset CMT1B phenotype. This point mutation introduces a Asp to Val substitution in a loop of the protein structure. Many other CMT-associated mutations hit this same position, suggesting that it may play a crucial role in the physiological processes mediated by MPZ, thereby rendering this segment less resistant to point mutations. Known CMT-associated mutations include D134N[118], D134G[119], D134E[118,120] and D134H[79], all leading to a CMT1B/DSS pathological phenotype. In the case of the D134V mutation, the substitution of the negatively charged side chain of a solvent exposed aspartic acid with a hydrophobic valine, leads to the generation of a stretch of 5 consecutive hydrophobic residues in a surface segment, as the sequence of the 132-137 segment is Pro132-Pro133-Val134-Ile135-Val136-Gly137 (figure 10). This enhanced hydrophobicity may alter aggregation propensity and stability of the protein. In order to assess experimentally what are the structural features affected by the D134V mutation, we will assess its structure, conformational stability, binding capacities and aggregation propensity, comparing in all cases the results with those obtained on the wild-type protein.

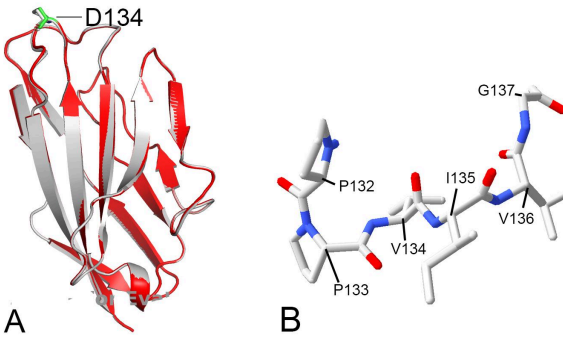

Figure 10. AlphaFold Predicted Structures of wild-type and D134V MPZ_{ex}. (**A**) Overlay of the predicted wt protein (gray) with the D134V mutant (red), generated using AlphaFold. The side chain of D134 (wt) is shown in sticks. (**B**) Close-up view of the local environment around the V134 (mutant) position in the predicted mutant structure, illustrating key residues (P132, P133, V134, I135, V136, G137) involved in the local fold.

3.1.1 D134V MPZ is globally folded but undergoes structural modifications

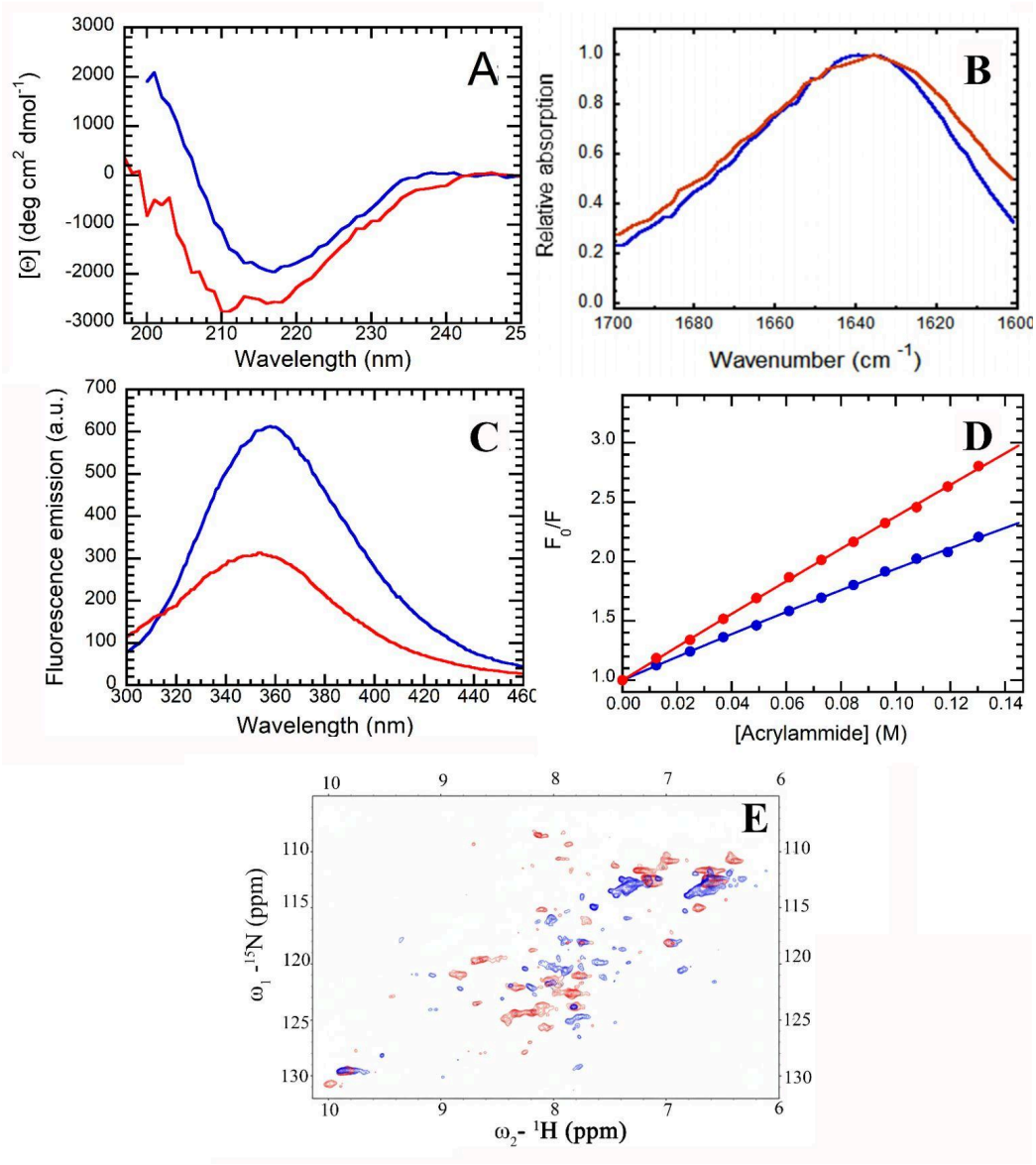

Figure 11. Structural characterization of wild-type and D134V MPZ$_{ex}$. (A) Far-UV CD spectra. (B) Normalized FTIR spectra of the Amide I region. (C) Intrinsic fluorescence emission spectra. (D) Stern-Volmer plots of fluorescence quenching by acrylamide. (E) Overlay of [^{1}H, ^{15}N]-HSQC NMR spectra. In all panels, data corresponding to wild-type MPZ$_{ex}$ are shown in blue and data for D134V MPZ$_{ex}$ are shown in red.

The structural integrity and conformational properties of the wild-type and D134V MPZ ext domain were thoroughly investigated by applying a battery of complementary biophysical techniques. First, we investigated the secondary structure of both variants by means of Far-UV CD spectroscopy, acquiring spectra between 200 and 250 nm (Figure 11A). This experiment supported the overall folded nature of both wild-type and D134V variants, showing typical β-sheet

characteristics, consistent with the expected immunoglobulin-like fold of MPZ. Indeed, the acquired spectra revealed a single negative band located ca. at 216-218 nm, corresponding to the $n \rightarrow \pi^*$ transition. Notwithstanding that, while the overall secondary structure content appeared to be similar, minor differences in the signal below 210 nm suggest localized conformational adjustments in the D134V mutant. Such adjustments probably correspond to an increase in unfolded residues, with respect to the wild-type protein

This scenario was further confirmed by FTIR spectroscopy (Figure 11B). The normalized spectra for both wild-type (blue trace) and D134V (red trace) are dominated by a major peak in the Amide I region centered at around 1640 cm^{-1}, characteristic of β-sheet content. The spectra are nearly superimposable, indicating that the mutation does not induce a significant change in the bulk secondary structure, consistent with the CD data.

Intrinsic fluorescence emission spectra (Figure 11C) of wild-type (blue trace) and D134V (red trace) revealed unexpected spectroscopic signatures of the MPZ structure. Indeed, while CD and FTIR show that these two variants are globally folded, wild-type MPZ shows a fluorescence emission peak located at 357 nm, a value usually found in globular proteins only when they populated an unfolded state. However, the structure of MPZ possesses 5 tryptophan residues, located at positions 53, 57, 66, 101 and 107. Among them, tryptophans 53, 57 and 107 are exposed to the solvent even in the folded state, and this may explain a significantly red-shifted emission. Notwithstanding that, a noticeable blue shift in the emission maximum was observed for the D134V variant, with its center of mass calculated at 356.8 nm, significantly lower than the 361.4 nm recorded for the wild-type protein. This suggests a more buried environment for the tryptophan residues in D134V, possibly indicating subtle structural modifications involving tryptophans: for example tryptophans 53 and 57 are positioned in two loops located in the same region of D134, with distances between the alpha carbons equal to 10.3 and 10.1 Å, respectively, and may consequently undergo small perturbations due to the D134V substitution. Alternatively, it is possible that the mutated protein is more prone to self-assemble, and that the indole moieties of tryptophan sidechains are buried in the aggregate.

Solvent accessibility, assessed by fluorescence quenching using acrylamide as quencher, showed that both proteins retain a folded state (Figure 11D). The K_{SV} constant for the wild-type protein was determined to be 9.38±0.47 M^{-1}, whereas for the D134V variant, it was significantly higher, reaching a value of 13.79±0.69 M^{-1}. This increased K_{SV}value for D134V suggests enhanced accessibility of fluorophores to the quencher, reinforcing the notion of structural alterations that expose more hydrophobic regions or introduce greater conformational flexibility compared to the wild-type protein.

In addition to the spectroscopic methods described above, the tertiary structure of the wild-type and D134V MPZex domain was investigated via ^{15}N-HSQC NMR spectroscopy. The NMR data (Figure 11E) provided further confirmation that both protein constructs maintain a well-defined and compact global fold in solution. In particular, the spectra showed a good dispersion of proton signals between 6 and 10 ppm, a distinctive characteristic of a well-folded protein, confirming that the mutation does not induce a large-scale unfolding or a transition across the major unfolding energy barrier to an unstructured state. However, an overlay of the wild-type and D134V spectra revealed a broad perturbation in the chemical shifts for numerous resonance signals. While a structural assignment of the observed resonances is not yet available and could not obtained in the present work, the notable shifts at various points of the spectrum indicate that the D134V mutation, while not compromising global structural integrity, induces subtle but extensive conformational reorganizations that propagate to different regions of the protein. Noticeably, perturbations involve also the side chains of lysines, located in the top left side of Figure 11E and the indole moieties of tryptophans, located in the bottom left corner of the same spectra, lending further support to the conclusions drawn from fluorescence emission spectroscopy. This evidence of increased structural dynamics and a subtly altered fold aligns perfectly with the increased solvent accessibility observed in the fluorescence quenching experiments.

3.1.2 The D134V mutation induces alterations of stability

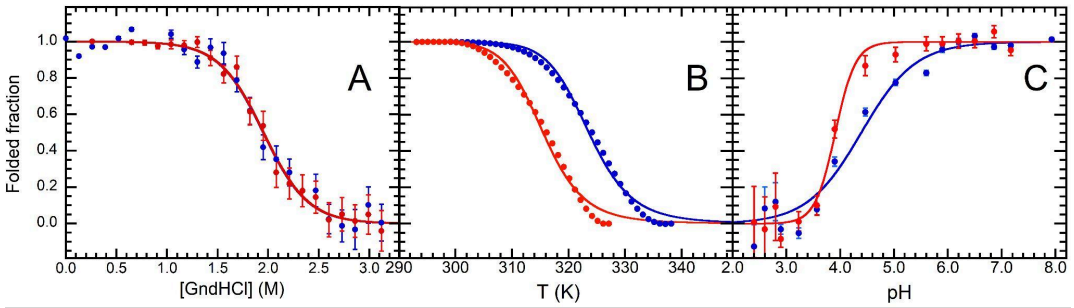

Figure 12. Conformational stability of wild-type and D134V MPZ$_{ex}$. GndHCl-induced denaturation curves (**A**), thermal denaturation curves (**B**) and pH-induced denaturation curves (**C**). Data are normalized to the fraction of folded domain as a function of GndHCl concentration (**A**) temperature (**B**) or pH (**C**) of wild-type (blue) and D134V (red) MPZ$_{ex}$.

The stability of the MPZ$_{ex}$ domains were assessed through GndHCl-induced unfolding, with protein denaturation monitored by changes in the far-UV CD signal at 222 nm. The resulting unfolding curves, displayed in Figure 12A, were fitted to a two-state model to derive the thermodynamic parameters, as reported in the Methods section and then normalized to the fraction of folded protein. The free energy of unfolding in the absence of denaturant (ΔG^{H2O}_{U-F}) was calculated to be 26100±1000 J mol^{-1} for the wild-type protein and 26200±1000 J mol^{-1} for the D134V mutant. The midpoint concentration of denaturation (C_m) was found to be 2.33±0.10 M for the wild-type and 2.34±0.10 M for the D134V mutant. Thus, these results illustrate that, while altering the structure of the protein, the D134V mutation does not significantly alter its thermodynamic stability.

The thermal stability of the MPZ$_{ex}$ domains were evaluated using DSF. As shown in Figure 12B, both the wild-type and the D134V mutant proteins exhibited a cooperative, two-state thermal unfolding transition, characterized by a sigmoidal increase in the fluorescence of the Sypro Orange dye as the proteins denature. The melting temperature (T_m), which represents the temperature at which half of the protein population is unfolded, was determined from the first derivative of the melting curves. The wild-type protein displayed a T_m of 323.5±0.02K. The D134V mutant showed a significantly lower T_m of 317.5±0.02 K. This represents

a decrease of approximately 6 K in thermal stability for the mutant, indicating a compromise of the protein's native folded state.

A reduction in T_m of this magnitude points to a significant weakening of the intramolecular forces that stabilize the protein's core fold. The substitution of a negatively charged, polar aspartate residue (D) with a non-polar, hydrophobic valine (V) at a crucial position within the Ig-like domain likely disrupts a critical hydrogen bond or a stabilizing salt bridge, making the protein more susceptible to thermal fluctuations.A comparison between the pieces of information obtained with chemical and thermal denaturation leads to a key finding, as these two experiments seem to give conflicting results. However, chemical denaturation reports on the thermodynamic stability of proteins, whereas thermal denaturation investigates thermal resistance: similar at first glance, these two concepts are fundamentally different[121]. Indeed, the similar ΔG_{U-F}^{H2O} and C_m values obtained with chemical denaturation indicate that the overall free energy difference between the native and fully unfolded states is conserved between the wild-type and mutant protein. This apparent discrepancy can be reconciled by considering the different mechanisms of thermal and chemical unfolding. While thermal unfolding is driven by the cooperative disruption of hydrophobic interactions, chemical unfolding with GndHCl is primarily mediated by the direct binding of the denaturant to the protein backbone, which preferentially solvates the unfolded state. The unchanged ΔG_{U-F}^{H2O} at 25 °C suggests that the mutation does not significantly alter the energy change upon denaturation at that temperature, i.e. it alters folded and unfolded states' energies at the same extent. However, increasing temperature seems to destabilize more the mutant than the wild-type and the native state of D134V becomes highly sensitive to thermal energy, as demonstrated by the lower T_m; however, it still requires a comparable concentration of GndHCl to achieve full denaturation into a random coil. Another way to interpret these results involves the model for thermal denaturation proposed by Privalov in 1990[122]. According to this model, the dependence of ΔG_{U-F} on the temperature T can be calculated as follows:

$$\Delta G_{U-F} = \Delta H_m \cdot \left(1 - \frac{T}{T_m}\right) + \Delta C_p \cdot \left[\left(T - T_m\right) - T \cdot ln\left(\frac{T}{T_m}\right)\right],$$

where again ΔG_{U-F} is the free energy change upon denaturation at a temperature equal to T, ΔH_m and ΔC_p correspond to the enthalpy and heat capacity change upon denaturation at T_m. The concomitant observations that $\Delta G_{U-F}^{H2O}(298\,K,\, wt) \simeq \Delta G_{U-F}^{H2O}(298\,K,\, D134V)$ and $T_m(wt) > T_m(D134V)$ can be explained if $\Delta C_p(wt) > \Delta C_p(D134V)$, i.e. if denaturation at T_m involves a higher change in C_p for the wild-type than it does for the D134V variant. As ΔC_p correlates to the amount of surface exposed to solvent upon unfolding[123], these data point towards a less compact unfolded state in the case of the D134V mutant. Furthermore, the two-state model may not fully capture the complexity of the unfolding pathway, which could include a non-cooperative pre-transition state that lowers the protein's thermal resilience but does not alter the overall free energy landscape measured by chemical denaturants.

To further probe the stability of the proteins, pH-induced unfolding was monitored by tracking changes in the CD signal at 222 nm across a broad pH range. As depicted in Figure 12C, both the wild-type and D134V proteins exhibit a sigmoidal unfolding transition as the pH decreases. The wild-type protein maintains its folded structure until a pH of approximately 3.5, at which point a cooperative unfolding transition is initiated. In contrast, the D134V mutant begins to unfold at a higher pH, with the unfolding transition beginning closer to pH 4.0. This indicates that the D134V mutant is less stable under acidic conditions than its wild-type counterpart.

Protein stability at low pH is dependent on the protonation of acidic residues such as aspartate and glutamate, which eliminates key stabilizing salt bridges. The substitution of the negatively charged aspartate at position 134 with a neutral valine permanently removes a potentially stabilizing ionic interaction. The finding that the mutant is less stable at low pH suggests that Asp134 is not merely a source of charge repulsion but is an active participant in a crucial stabilizing interaction, likely a salt bridge with a nearby basic residue (such as, for example,

K138). The permanent loss of this stabilizing bridge in the D134V mutant predisposes the protein to unfold under more moderate acidic stress. This observation adds important details to the findings obtained from the thermal denaturation data: the D134V mutation fundamentally weakens the protein's native fold, making it susceptible to multiple forms of environmental stress.

3.1.3 The D134V mutant has a higher propensity to undergo aggregation with respect to the wild protein

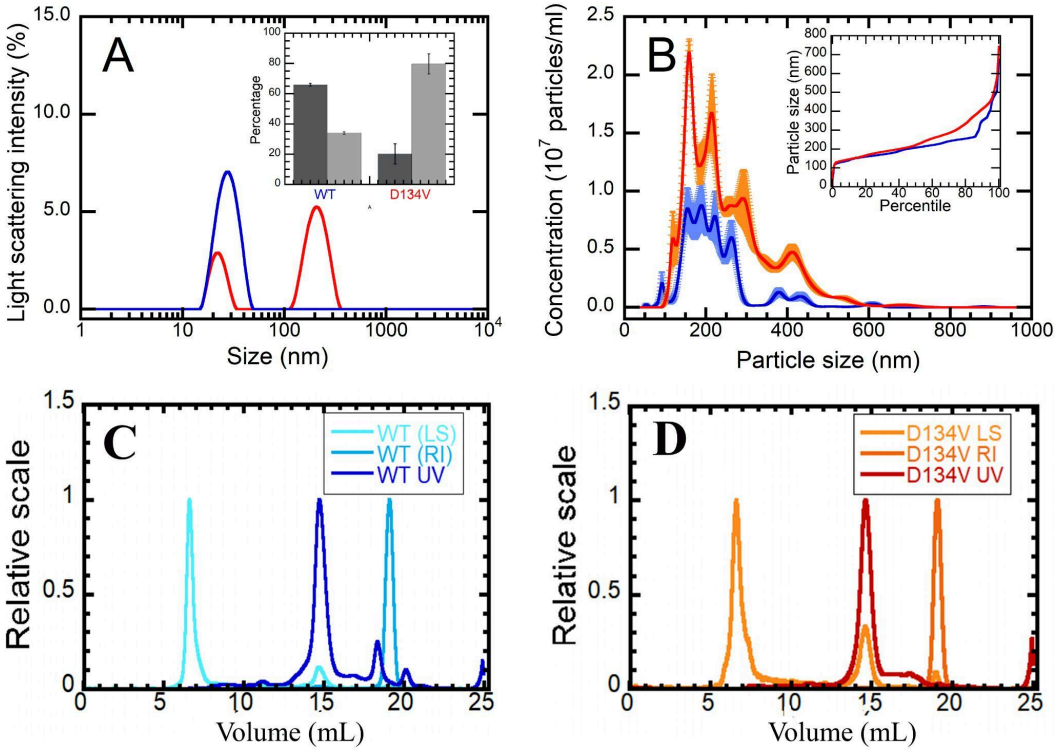

Figure 13. Light scattering experiments on wild-type and D134V variants of MPZ_{ex}. (A) Representative light scattering intensity distribution versus size, measured immediately after centrifugation and filtration with 20 nm filters of the wild-type (blue) and D134V (red) protein samples. The inset shows the distribution of the signal below (dark grey) and above (light grey) 30 nm of size. Error bars correspond to s.e.m. over measurements of 5 different samples (n=5). (B) Distributions of particle concentration versus particle size after 24 h since centrifugation and filtration with 20 nm filters of the wild-type (blue) and D134V (red) protein samples. The inset shows the ECDF plot (percentile plot). The shaded areas indicate the standard error of the mean (s.e.m.). (C-D) SEC-MALS chromatograms for (C) wild-type MPZ_{ex} and (D) D134V MPZ_{ex} on a Superdex 75 increase column. The traces show the normalized signals from Light Scattering (LS, light blue/orange), Refractive Index (RI, medium blue/red), and UV absorbance (UV, dark blue/dark red), plotted against the elution volume.

Immediately after its purification, the D134V protein variant exhibited a strongly enhanced tendency to precipitate and assemble into aggregates. In our hands, this mutant partially precipitates if subjected to a freezing and thawing cycle and tends to aggregate if left untouched for a few days at 4 °C. In order to quantify such tendency to self-assemble, we set out to compare the results of light-scattering measurements on the mutated and wild-type proteins. First, we collected dynamic light scattering intensity distributions immediately after centrifugation for 5 minutes at 14,000 x g and filtration with anotop® 20 nm filters, a procedure that should in principle be able to remove aggregated material. Within the dead-time of the experiment, due to the time intercurring between filtration and acquisition, both the wild-type and D134V variant exhibited a significant tendency to form high molecular weight assemblies and the signal of the aggregates masks the light scattered by monomers (fig. 13A). This implies that, at least in our experimental setting, MPZ_{ex} tends inherently to form small amounts of aggregates, even in the short time intercurring between sample filtration and data acquisition (ca. 2 minutes). Despite that, D134V has a markedly enhanced propensity to form assemblies of higher sizes. We analyzed the distributions obtained, splitting the signal between light scattered by particles having a diameter lower or bigger than 30 nm (fig. 13A inset). The results reveal that for the wild-type 34.0 ± 1.2 % of the light is scattered by aggregates with a diameter higher than 30 nm; this percentage increases to 79.8 ± 11.5 % in the D134V. Next, we repeated the measurement after 24 h since centrifugation and filtration, this time using the Malvern NS-300 machine, able to directly track and measure the particle concentration, rather than measure the scattered light (fig. 13B). While the instrument is unable to assess the concentration of particles with diameters below 10 nm, even in this case the data confirm a higher tendency to precipitate for the D134V variant. We measured a total number of $(117.5 \pm 26.7) \cdot 10^7$ and $(299.2 \pm 40.1) \cdot 10^7$ particles / ml for wild-type and D134V, respectively. The empirical cumulative distribution function (ECDF) (fig. 13B inset) shows that, for example, the third quartile (i.e. 75% of the aggregates) have diameters up to 249 and 305 nm, respectively, for wild-type and D134V. This implies a tendency to form higher molecular order assemblies for the mutant.

The experiments described so far failed, however, to detect the monomer. Consequently, we sought to determine the oligomeric state of the proteins in solution immediately following purification, before aggregation takes place. We performed SEC-MALS analysis on the purified stock solutions (Figure 13C, D). The elution profile for wild-type MPZ_{ex} (Figure 13C) shows a single, symmetrical peak eluting at approximately 14.5 mL, where the LS, RI, and UV signals are coincident. This profile confirms the protein is predominantly a monodisperse monomer. The D134V variant (Figure 13D) exhibited an identical elution profile, confirming it is also predominantly monomeric in its purified, non-aggregated state.

Taken together, these data show and quantify that, while both proteins exist as monomers in solution (as shown by SEC-MALS), MPZ_{ex} has an inherent tendency to self-assemble into high order insoluble molecular assemblies, as detected by means of light scattering. However, the same light scattering measurements indicate that the D134V has a higher tendency to aggregate and to form aggregates of larger size. This difference may become irrelevant once the protein is expressed on the outer side of the membrane, but it may prove crucial after translation, while the protein undergoes the different post-translational modifications that lead to protein maturation.

3.1.4 D134V exhibits altered binding capacities

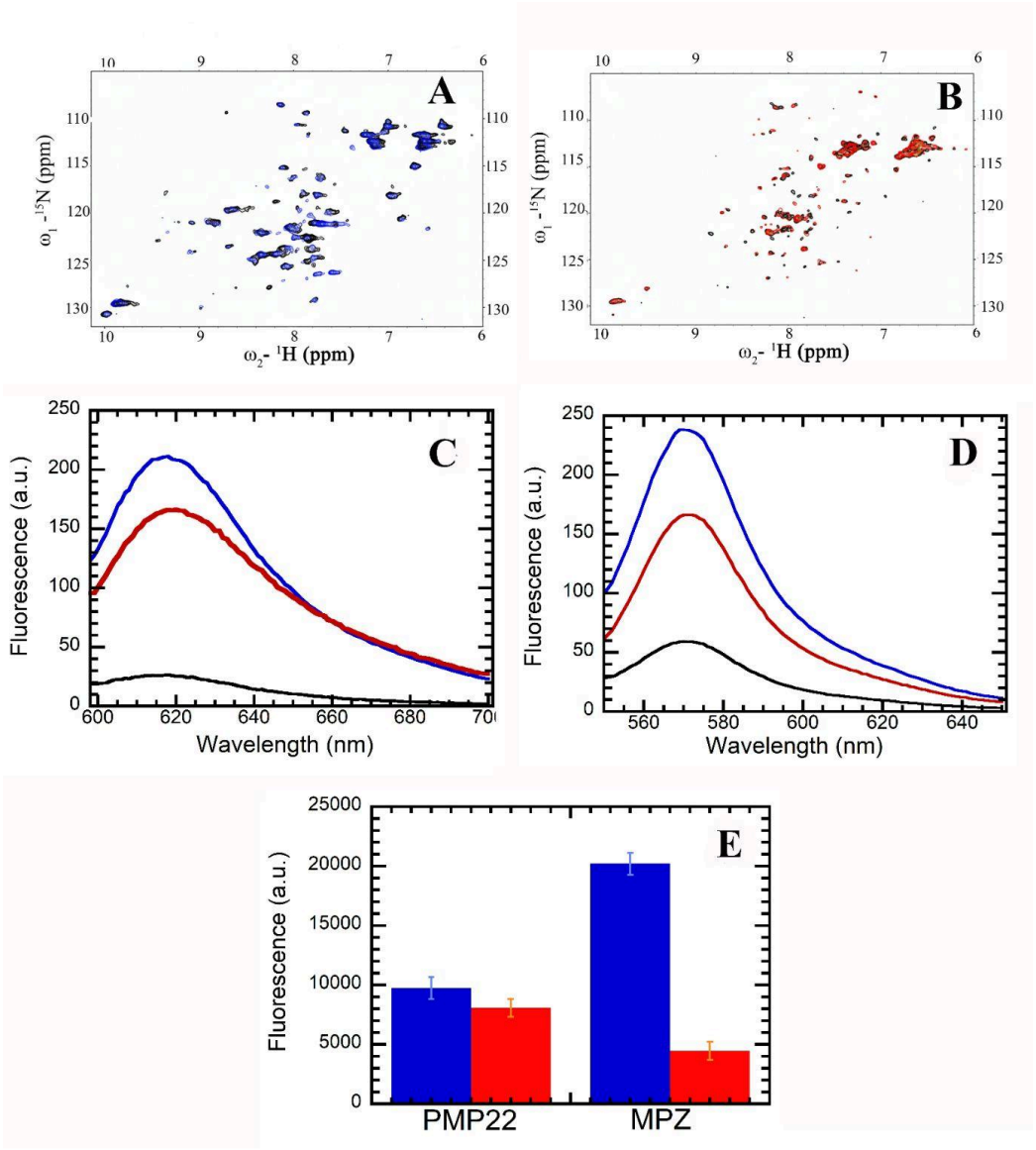

Figure 14. Intermolecular interactions of wild-type and D134V. (A) [^{1}H, ^{15}N]-HSQC NMR overlay of ^{15}N-labelled wild-type MPZ_{ex} in the absence (blue) and presence (black) of unlabelled PMP22ex. (B) [^{1}H, ^{15}N]-HSQC NMR overlay of ^{15}N-labelled D134V MPZ_{ex} in the absence (red) and presence (black) of unlabelled PMP22ex. (C) Representative fluorescence spectra for the heterophilic binding assay (labelled PMP22ex bound to a non-fluorescent MPZ_{ex} molecule). The black trace represents the blank in the absence of MPZ_{ex}. (D) Representative fluorescence spectra for the homophilic binding assay (labelled MPZ_{ex} bound to a non-fluorescent MPZ_{ex} counterpart). The black trace represents the blank. (E) Summary of the fluorescence data. The analysis reveals a non-significant difference between wild-type (blue bar) and D134V (red bar) for PMP22ex heterophilic interactions (PMP22 group) and a significant reduction of homophilic MPZ_{ex} interactions (MPZ group) in D134V relative to wild-type. Error bars represent s.d..

To investigate the effect of the D134V mutation on the binding properties of the MPZ_{ex} domain, we examined its intermolecular interactions with PMP22. We first performed NMR experiments to exploit CSP and structurally detect the heterotypic interaction with PMP22ex, a peptide carrying the sequence of the second extracellular loop of PMP22 (see the Methods section). The overlay of the 15N-labeled wild-type MPZex domain in the absence (blue trace, Figure 14A) and presence (black trace, Figure 14A) of unlabeled PMP22ex showed that, while the general fingerprint of the protein backbone is maintained upon addition of the ligand, numerous peaks undergo significant CSPs, providing direct evidence of a specific interaction. The same experiment was repeated for the mutant protein. A titration of the 15N-labeled D134V mutant with the PMP22 peptide also resulted in noticeable CSPs, confirming that the mutant protein retains the ability to bind to PMP22 (Figure 14B). Given the different binding profiles of the two protein variants, a direct quantitative comparison of the interaction affinity via NMR was not feasible. Thus, fluorescence-based binding assays were employed to quantitatively compare the binding capacities of the wild-type and D134V variants. Analysis of heterotypic interactions PMP22ex (Figure 14C, 14D) revealed that both wild-type and D134V MPZex bind to PMP22ex, with a non-significant difference in their binding capacities. Indeed, when we calculated the total fluorescence emitted by the different samples we obtained signals of 9748.5 ± 938 and 8079.8 ± 755.4 a.u. for the wild-type and the mutant, respectively.

The fluorescence spectra presented in Figure 14D provide a qualitative and semi-quantitative overview of the homophilic binding interactions of MPZ. The spectra were acquired with an excitation wavelength of 540 nm, corresponding to the maximum absorption of the BODIPY™ probe, and the emission was recorded over the range of 560-640 nm.

The blue curve in Figure 14D represents the fluorescence spectrum of the eluted protein from the pull-down assay using the wild-type MPZex domain as an immobilized bait. The spectrum shows a distinct and strong peak at approximately 575 nm, corresponding to the emission maximum of the BODIPY™ probe. The high intensity of this signal directly indicates that a

significant amount of fluorescently labeled MPZ_{ex}-BODIPY™ was captured by the unlabeled, immobilized wild-type MPZ_{ex}. This finding provides clear visual evidence of a strong homophilic interaction between MPZ wild-type domains.

In contrast, the red curve, which corresponds to the MPZ mutant, exhibits a substantially lower peak intensity. The total fluorescence values obtained from a statistical analysis of the experiments led to values of 20200 ± 740.6 and 4462.5 ± 1504.1 a.u. for wild-type and mutant protein, respectively. This attenuated fluorescence signal indicates that a significantly reduced amount of labeled mutated protein was bound and subsequently eluted from the resin, with respect to what we observed for the wild-type protein. This provides qualitative evidence that the mutation within the MPZ_{ex} domain impairs the homophilic binding capability, a property that is essential for its function.

In both figures 14C and 14D, the black curve represents the fluorescence spectrum of the negative control, which contains only resin and no immobilized protein. The fluorescence signal for this sample is negligible, which confirms that the His-tag-free MPZ_{ex}-BODIPY™ does not bind non-specifically to the Ni-NTA resin.

The qualitative findings from the fluorescence spectra were further corroborated and quantified using the bar chart in Figure 14E, which displays the mean fluorescence intensity values for each sample. The data for the MPZ_{ex} domain reveals a difference between the wild-type e and the mutant.

The blue bar, representing the wild-type MPZ, shows a mean fluorescence intensity of approximately 20,000 arbitrary units (a.u.). This high value quantitatively confirms the strong homophilic binding observed in the fluorescence spectra. The successful capture and elution of a large quantity of labeled protein validate that the extracellular domain of MPZ is capable of self-association.

In contrast, the red bar for the MPZ mutant exhibits a significantly lower mean fluorescence intensity, measuring at approximately 4,000 a.u.. This reduction in fluorescence demonstrates that the mutation has a profound negative impact on the protein's ability to engage in homophilic interactions.

3.2 Discussion

In this section, we reported the identification of a novel D134V mutation in the MPZ protein, providing a contribution to the understanding of the molecular pathogenesis of CMT1B. The D134 position emerges as a crucial structural hotspot in the MPZ extracellular domain: multiple disease-causing mutations at this site (D134N, D134G, D134E, D134H) have been reported, all leading to severe demyelinating phenotypes. In our analysis, a susceptibility plot reveals a distinct peak of sensitivity within the region spanning residues 130-140, indicating that this protein segment, corresponding structurally to a loop, is under substantial evolutionary pressure and that alterations here are highly likely to be pathogenic (fig.15E). This finding aligns with the work of Ptak et al., who mapped CMT-causing variants to spatially distinct regions of the MPZ_{ex}, correlating variants that destabilize the core Ig-fold with severe, early-onset demyelinating disease. We performed an analysis of the protein frustration[124]. This parameter describes the energetic conflicts present in a certain protein structure: if a given residue is not the optimum for protein stability, protein evolution must have selected it for other purposes, be them catalysis, binding, allosterism or other functions. Our frustration analysis on the MPZ structure indicates that MPZ possesses high levels of frustration in the apical and basal regions, containing the loops that connect the strands, while the secondary structure regions have evolved in order to maximize structural stability. Thus, the loop regions contain many energetically unfavorable contacts, highlighted in red in Figure 13A and 12B. Substituting Asp with Val at this position introduces alterations of these contacts (Figure 15C), but in general, the frustration index of the loop connecting strands E and F undergoes a significant increase (Figure 15D). In essence, D134 appears to act as a functionally important residue that introduces frustration to MPZ. Its substitution with a valine, however, exacerbates frustration, while probably compromising function.

Our biophysical characterization demonstrates that D134V MPZ retains a folded Ig-like type V architecture but is markedly less stable and more dynamic than the wild-type protein. FTIR, far-UV CD and NMR spectra indicate that the mutant preserves the overall β-sheet rich immunoglobulin fold, suggesting no major unfolding transitions. However, subtle conformational perturbations are evident:

for example, the intrinsic tryptophan fluorescence of D134V is blue-shifted relative to wild-type, suggesting a slightly altered tertiary packing around solvent-exposed loops near residue 134, or an increased tendency to aggregate. Most strikingly, D134V shows a significant decrease in stability under various stress conditions. Differential scanning fluorimetry revealed a melting temperature (T_m) ~6 K lower for D134V (~317.5 K) than for wild-type (~323.5 K), highlighting compromised thermal resistance. The mutant is also less tolerant of acidic pH, unfolding at a higher pH (~4.0) compared to wild-type (~3.5). In contrast, chemical denaturation (GndHCl) experiments yielded virtually identical unfolding free energies for D134V and wild-type at 25 °C, with the same midpoint denaturant concentration. At first glance this is a paradox – the mutant unfolds more readily with heat or low pH, yet its equilibrium stability against chemical unfolding appears unchanged. We interpret this as evidence that D134V introduces distortion to the folded state and/or alters the accessible to solvent area of the unfolded state. The mutation may also lead to a metastable native conformation: in this case the overall free energy difference between folded and completely unfolded states is preserved, but the protein has an increased tendency to sample partially unfolded or loosened conformations at elevated temperature. In other words, D134V may lower the kinetic or cooperative barrier to unfolding without greatly altering the final unfolded state's energetics. This metastability means that the mutant domain is exquisitely sensitive to environmental stressors – a ticking time bomb where even mild thermal or pH stress can tip it into unfolding. Such a state is a well-known precursor to protein misfolding and aggregation, and indeed many destabilizing MPZ mutations are known to trigger quality-control mechanisms in cells[52].

Consistent with its compromised stability, the D134V variant exhibits a markedly enhanced tendency to misassemble into aggregates. Immediately after purification, both wild-type and D134V MPZ_{ex} are monomeric in solution as shown by SEC–MALS (each showing a single monodisperse peak of ~14.5 mL elution volume corresponding to the monomer). This indicates that the D134V mutation does not constitutively form oligomers when freshly folded. However, light-scattering assays revealed that MPZ is inherently prone to self-assemble. Moreover, D134V rapidly self-associates into high-molecular-weight species to a

much greater extent than the wild-type protein. In DLS measurements performed just minutes after filtering out any pre-formed aggregates, the mutant sample showed a dominant light-scattering signal from large particles that dwarfed the monomer signal. Quantitatively, the fraction of scattering intensity arising from particles >30 nm in diameter was ~80% for D134V, compared to only ~34% for wild-type under the same conditions. This indicates that even on a very short timescale, D134V monomers begin nucleating into sizable aggregates more efficiently. After 24 hours, nanoparticle tracking analysis revealed significantly higher particle counts and larger aggregate size distributions in the mutant sample relative to wild-type. For instance, the total particle concentration for D134V was roughly 2.5-fold higher than for wild-type, and the median aggregate size of the mutant shifted to larger diameters (the 75th percentile of aggregate size was ~305 nm for D134V vs. ~249 nm for wild-type). Taken together, these data demonstrate that, while MPZ_{ex} has an inherent tendency to self-associate even in its wild-type form, the D134V mutation greatly accelerates and amplifies aggregation propensity. The mutant remains a monomer initially, but its fold is fragile enough and monomers readily misfold and cluster into insoluble oligomers/aggregates over time or upon slight perturbations. In a cellular context, this behavior implies that D134V MPZ may be prone to precipitation or degradation during biosynthesis and trafficking, potentially overwhelming the proteostasis machinery.

The structural instability of D134V MPZ provides a direct mechanistic explanation for its loss of biological function in myelin. MPZ's physiological role is to serve as the adhesive glue of the myelin sheath, mediating homophilic binding between extracellular domains on adjacent membrane layers[56]. This adhesion is achieved by a well-organized assembly of MPZ Ig domains: each MPZ can form lateral cis-oligomers in the same membrane and trans-dimers with MPZ molecules on the apposing membrane. Two complementary models have been proposed for this architecture. In the "cis-tetramer" model (elaborated from the crystal packing of rat MPZ), MPZ monomers first assemble into tetramers in the plane of the membrane; these tetramers then interact across the intraperiod gap via antiparallel dimers, effectively zipping together the two membranes[56]. In contrast, the "trans-zipper" model (supported by cryo-EM analysis of full-length

MPZ) posits that the fundamental adhesive unit is an antiparallel Ig-domain dimer bridging the two membranes, without requiring higher-order cis-oligomers[41]. Regardless of the exact arrangement, all the models proposed so far demand a properly folded, structurally rigid MPZ Ig domain to engage in binding. Our findings indicate that D134V MPZ_{ex} is structurally compromised – it fluctuates more, unfolds more easily, and aggregates more. One can liken a D134V monomer to a "defective part" in the adhesion machinery. In the cis-tetramer scenario, an unstable D134V subunit would act as a "poisoned subunit" that could destabilize the entire tetramer, preventing it from forming or from binding to its counterpart on the adjacent membrane. In the trans-dimer scenario, a D134V monomer is akin to a broken tooth in a zipper, failing to lock into its opposing partner and thus weakening the overall adhesion between membranes. In either case, the loss of robust homophilic interaction would translate to impaired myelin compaction. The dramatic reduction we observed in homophilic binding affinity for the D134V mutant (an ~4–5 fold lower binding signal in our MPZ–MPZ pull-down assay compared to wild-type) reinforces that the mutation largely abolishes the self-adhesive function of MPZ. This is entirely consistent with the severe demyelinating phenotype seen in patients: if MPZ molecules cannot stick membranes together, the myelin sheath cannot form stable compact myelin, leading to the conduction block and neuropathy characteristic of CMT1B.

Interestingly, our assays did not find a significant difference between D134V and wild-type MPZ in their ability to bind a PMP22-derived peptide. Interestingly, early studies had suggested that MPZ might form a complex with PMP22 in myelin, based on co-immunoprecipitation experiments[116]. In our NMR titration experiments, both wild-type and D134V MPZ_{ex} showed CSP upon addition of the PMP22 second loop peptide, indicating that the mutant still recognizes and interacts with PMP22's extracellular loop to a similar extent as the wild-type protein. Consistently, a fluorescence-based heterophilic binding assay showed no statistically significant difference between mutant and wild-type MPZ_{ex} in binding to the PMP22 loop in vitro. While this suggests that the D134V mutation does not abolish MPZ's heterophilic interaction with PMP22 when these two proteins are located in apposing membranes, it is crucial to note that the physiologically relevant MPZ–PMP22 interaction occurs also within their transmembrane

domains, not only via the extracellular Ig domain. Recent work by Pashkova et al. demonstrated that MPZ and PMP22 form a specific complex through interfaces in their transmembrane helices, and disrupting this TM–TM interface (for example, by a PMP22-A67T mutation) causes a demyelinating phenotype[61]. Our assay, lacking the transmembrane regions, does not replicate the complete native binding mode but investigates one of the inter-leaflet interactions between MPZ and PMP22. Therefore, the present experiments are not sufficient to conclude that the D134V mutation leaves MPZ–PMP22 interactions unaffected in the myelin membrane. Rather, they suggest that the mutation alters MPZ-PMP22 interactions that occur between apposing membranes. In fact, given D134V's propensity for misfolding, one could speculate that the mutant MPZ might not fold or integrate into the membrane correctly enough to even present the proper interface to PMP22. It is conceivable that D134V could indirectly impair the MPZ–PMP22 complex by misaligning MPZ's transmembrane segment or causing mislocalization. Ultimately, the dominant pathogenic mechanism of D134V appears to be a "toxic loss of function": the mutant MPZ loses its homophilic adhesive capacity due to structural instability and aggregation, and this alone is sufficient to produce a severe hypomyelinating neuropathy. Any effect on MPZ's other interactions (such as with PMP22) would only be secondary.

In summary, the D134V mutation renders MPZ a structurally unstable and aggregation-prone protein, abolishing its essential adhesion function in myelin. While the mutant maintains a native-like fold, it exists in an unstable state with a lowered threshold for unfolding. This leads to metastability of the extracellular domain – it can no longer reliably serve as a building block for the ordered oligomers that knit the myelin layers together. The consequence is two-fold and self-reinforcing: loss of adhesive function (because the protein cannot engage in or maintain the required homophilic bonds) and gain of misfolding toxicity (as the unstable protein aggregates, likely eliciting cellular stress responses). The D134V variant thus behaves as a severe, toxic mutation, in line with the clinical phenotype of early-onset CMT1B. By studying this mutant, we underscore the general principle that even single-point mutations in structurally critical residues can tip the balance of a protein from a functional state to a deleterious, disease-causing state. Our results on D134V MPZ_{ex} provide a concrete

biophysical basis for the neuropathy observed in patients, and they highlight the importance of maintaining the stability of the MPZ Ig domain for peripheral myelin integrity.

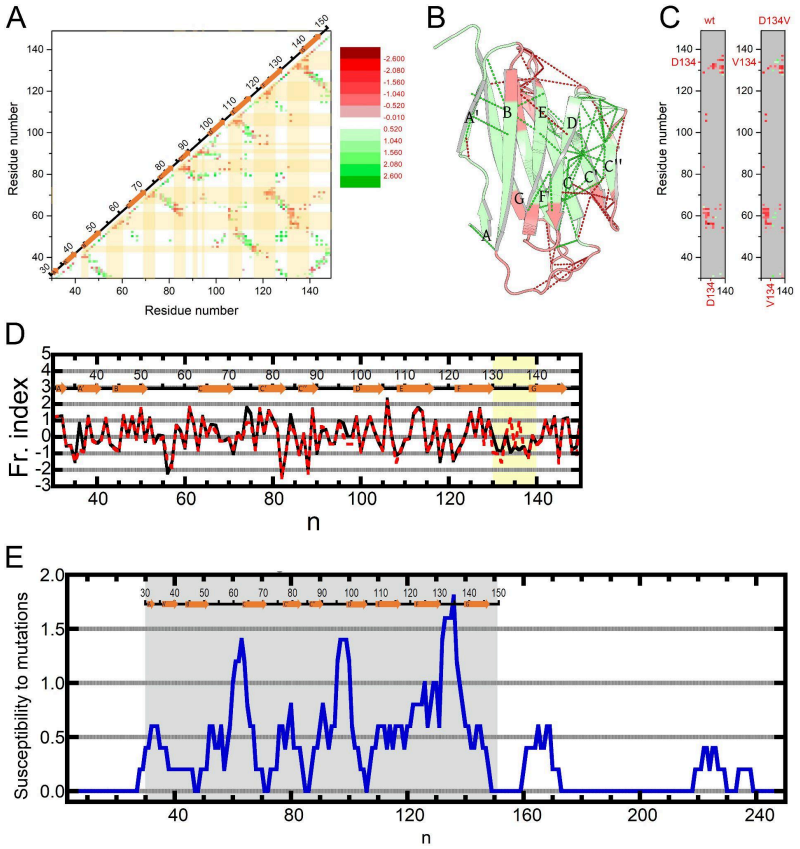

Figure 15 (**A**) Frustration map of wild-type MPZ_{ex}, highlighting contacts of high and low energetic conflict, termed frustration, within the structure. The map is color coded to highlight regions with low (green) or high (red) frustration. (**B**) Structure of MPZ_{ex} showing the localization of the frustrated (red) or poorly frustrated (green) contacts. (**C**) Difference in the frustration map induced by the D134V mutation of MPZex. Colours as in panel B (**D**) Plot of the frustration index versus amino acid residue number in wild-type (black) and D134V MPZex; the plot shows the secondary structure of the protein on the top. (**E**) Number of known disease linked mutations versus amino acid residue number for MPZex; the plot shows the secondary structure of the protein on the top.

Chapter 4 Comparative Analysis of a Panel of Pathogenic MPZ_{ex} Variants

4.1 Results

4.1.1 Mutagenesis and Purification

MPZ_{ex} mutants (I30M, R36G, H39P, H81L, H81Q, N122S, N131Y, D134E, and D134V) were successfully generated using the Q5 Site-Directed Mutagenesis Kit (NEB), employing the previously engineered pQE-30 vector encoding the wild-type MPZ_{ex} as a template, following the protocol detailed in section 2.1.1. Following amplification and ligation, all mutant plasmids were verified by Sanger sequencing (BMR Genomics, Padua, Italy) to confirm the successful introduction of the desired single amino acid substitutions, as shown in the representative chromatograms in Figure 16. The sequence-verified plasmids were then transformed into XL1-Blue E. coli for protein expression. Following induction, all protein variants accumulated as IBs. The IBs were harvested, washed, solubilized under denaturing conditions (8 M Urea), and purified according to the protocol described in section 2.1.2. This multi-step process involved ion mobility affinity chromatography, a controlled refolding step via dropwise dilution into a refolding buffer, and a final polishing step using IEX. This comprehensive purification strategy yielded approximately 1 mg of protein per liter of bacterial culture for all variants. Analysis of the final purified fractions by SDS-PAGE confirmed a high degree of homogeneity, estimated to be at least 95% pure (not shown).

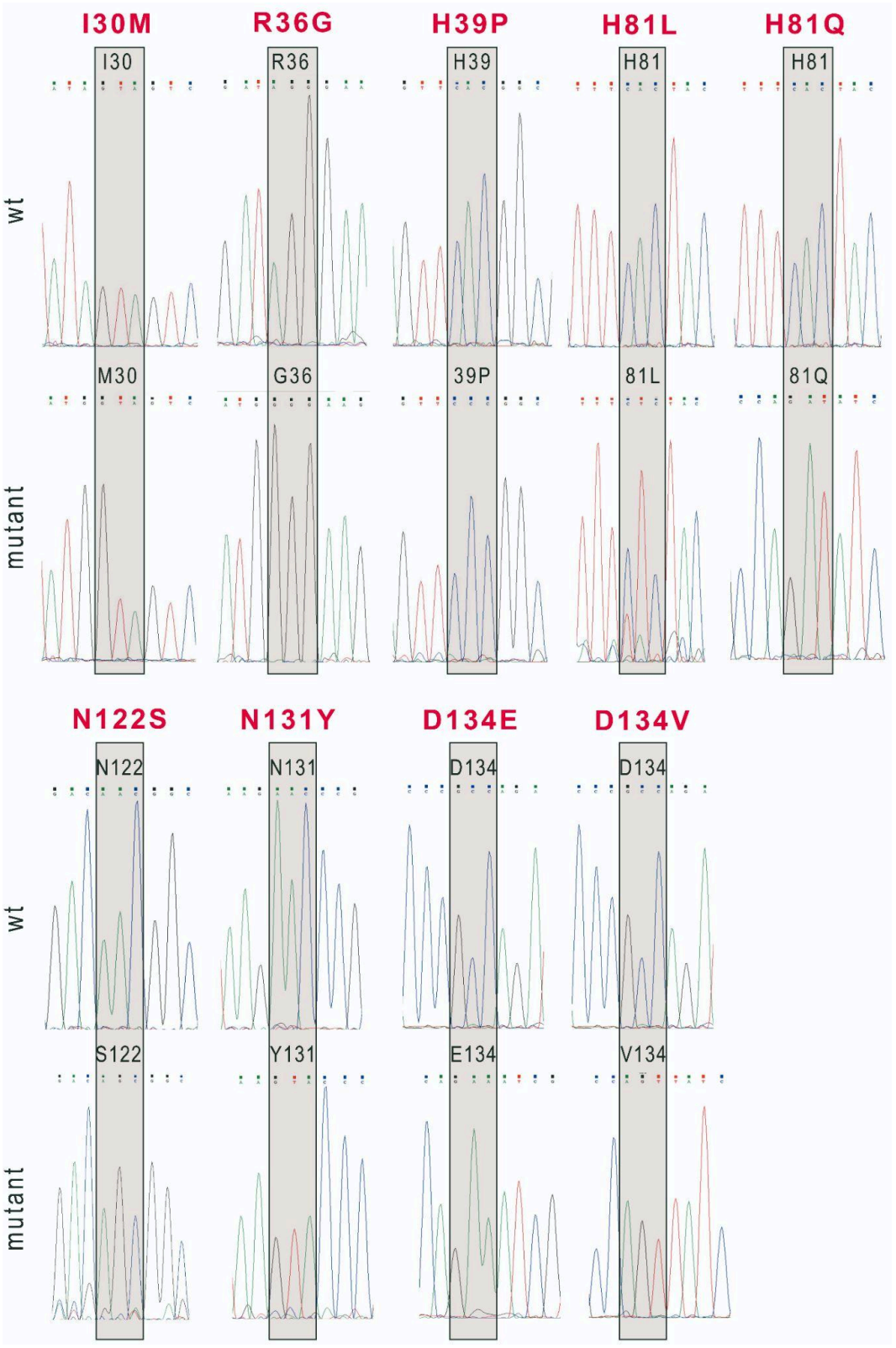

Figure 16. Chromatogram resulting from Sanger sequencing of the plasmids successfully carrying the desired mutation. The rectangle highlights the wild-type codon and the corresponding successful mutant codon for each variant

4.1.2 Far-UV CD

To assess the impact of mutations on the secondary structure of the MPZ extracellular domain, Far-UV CD spectra were recorded for the wild-type protein and the nine variants (Figure 17)

The far-UV CD spectra (200–250 nm) of the MPZ_{ex} wild-type and all nine mutants are overall similar in shape, each exhibiting a broad negative ellipticity band in the ~210–220 nm region, but clear differences in band intensity and subtle shifts are observed for each variant relative to wild-type. The wild-type spectrum is characterized by a distinct negative minimum around 217 nm with strong ellipticity magnitude. The I30M mutant produces a CD trace virtually superimposable on the wild-type, with an identical negative-band position (~217 nm) and only a very slight decrease in ellipticity. Similarly, R36G shows only minimal spectral changes, retaining the wild-type's overall profile and band position with a marginal reduction in negative ellipticity. In contrast, H39P exhibits the most pronounced deviation: its negative band near 217 nm is markedly diminished in intensity, and the spectrum is notably flattened, with the ellipticity becoming much less negative across the range (the trace lacks a well-defined minimum and trends toward higher ellipticity at ~200 nm compared to wild-type. The spectra of H81L and H81Q remain similar in shape to wild-type – both mutants preserve the characteristic negative band near 217 nm – but each shows a moderate decrease in ellipticity magnitude (with H81L displaying a slightly larger reduction than H81Q). The N122S variant yields a spectrum almost indistinguishable from wild-type, showing no significant change in the position or intensity of the negative band. In the case of N131Y, the main negative band around 217 nm is retained but with noticeably lower ellipticity, giving a shallower trough relative to wild-type. Finally, the D134E and D134V mutants present differing degrees of change: D134E's CD spectrum is only slightly attenuated (a small drop in negative ellipticity intensity at 217 nm, otherwise closely matching the wild-typetrace), whereas D134V shows a substantial reduction in the amplitude of the negative band (the ellipticity at ~217 nm is greatly decreased) while still maintaining a broadly wild-type-like spectral contour. Overall, each mutant's far-UV CD spectrum spans 200–250 nm with the same general shape as wild-type but with the above variations in negative band position and ellipticity

intensity, highlighting the individual effects of each point mutation on the secondary-structure signature of the protein.

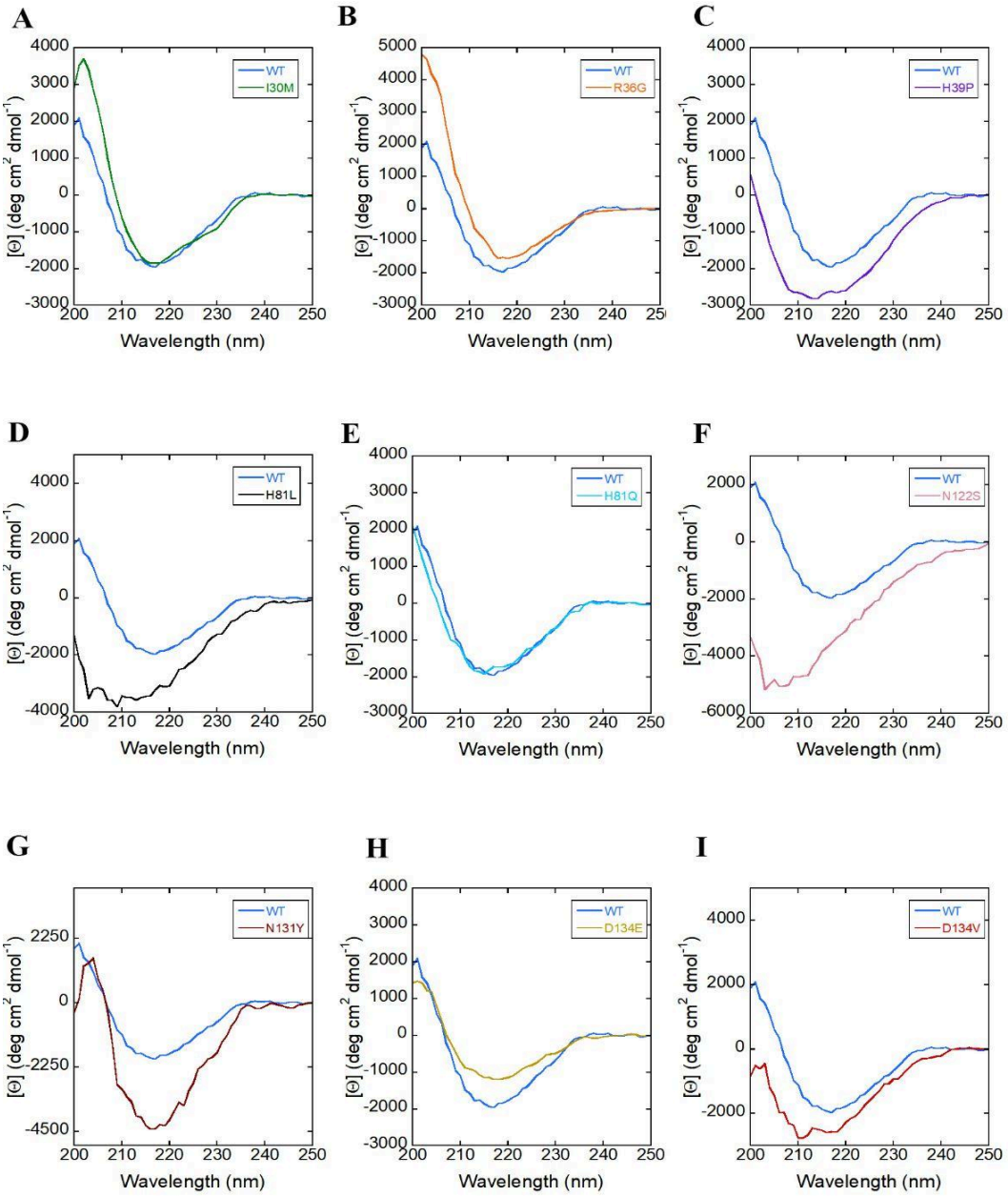

Figure 17. Far-UV Circular Dichroism spectra of wild-type and MPZ$_{ex}$ variants. Spectra were recorded from 200 to 250 nm at 25 °C. Data are expressed as mean residue molar ellipticity ϑ in units of deg cm² dmol⁻¹. In each panel, the spectrum of the wild-type MPZ domain is shown as a blue trace for comparison.

4.1.3 Intrinsic fluorescence spectroscopy

Here we report the intrinsic tryptophan fluorescence of MPZ_{ex} wild-type and all variants (Figure 18A–I), with the calculated COM (λ_{CM}) and maximum intensity summarized in the overview plot (Figure 18L). The wild-type protein, blue trace in all panels, showed λ_{CM} = 363.83 nm and I_max = 47,735 a.u., used as the reference.

D134V (Figure 16I) displayed the most pronounced alteration, with a strong blue shift to 357.51 nm and the lowest intensity (26,349 a.u.). A large blue shift was also observed for H39P (Figure 18C), 355.38 nm, while its intensity (46,821 a.u.) remained comparable to wild-type. A second group—I30M (Figure 18A; 361.49 nm, 70,607 a.u.), H81L (Figure 18D; 363.38 nm, 72,760 a.u.), D134E (Figure 18H; 362.63 nm, 71,664 a.u.), and N122S (Figure 18F; 366.16 nm, 70,012 a.u.)—showed markedly higher fluorescence; N122S was the only variant with a slight red shift. The remaining variants, R36G (Figure 18B; 361.44 nm, 42,931 a.u.), H81Q (Figure 18E; 362.10 nm, 36,900 a.u.), and N131Y (Figure 18G; 361.37 nm, 47,772 a.u.)—exhibited modest blue shifts and intensities close to wild-type.

Overall, most variants display a modest blue shift compared with wild-type; H39P and D134V show the largest spectral displacements, while I30M, H81L, N122S, and D134E exhibit markedly higher fluorescence intensities.

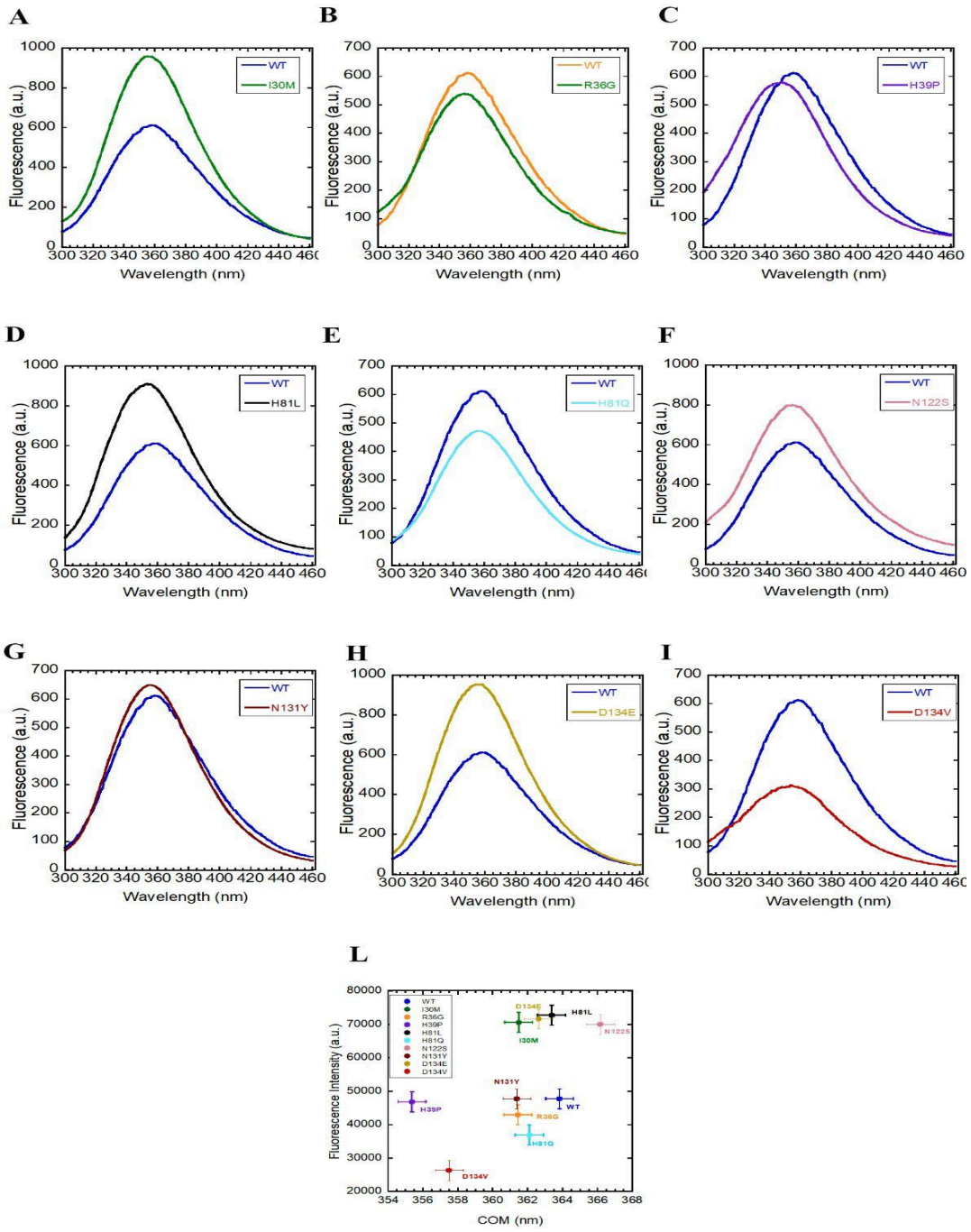

Figure 18. Comparative Analysis of Intrinsic Tryptophan Fluorescence for MPZ_{ex} Variants.(A-I) Fluorescence emission spectra comparing each MPZ_{ex} mutant (colored traces) to the wild-type (wild-type, blue trace). The specific mutants shown are: (A) I30M, (B) R36G, (C) H39P, (D) H81L, (E) H81Q, (F) N122S, (G) N131Y, (H) D134E, and (I) D134V.(L) Summary plot of the Center of Mass (CM) wavelength versus maximum fluorescence intensity for wild-type (blue square) and all mutant variants (colored data points with error bars.

4.1.4 Acrylamide Quenching Experiment

To probe solvent exposure of the Trp residues, we performed acrylamide quenching on MPZ_{ex} wild-type and all variants. The Stern–Volmer plots were linear over the explored range (0–0.125 M), consistent with predominantly dynamic quenching (Figure 19A–I). The wild-type exhibited a K_{SV} of 9.38 ± 0.47 M^{-1}. Markedly higher values—indicative of increased fluorophore accessibility—were measured for N122S (25.05 ± 1.25), N131Y (20.02 ± 1.00), and I30M (18.17 ± 0.91). Moderate increases were observed for H81Q (14.10 ± 0.71), D134V (14.38 ± 0.72), D134E (13.25 ± 0.66), and R36G (12.66 ± 0.63). In contrast, H81L (6.36 ± 0.32) and H39P (8.13 ± 0.41) quenched less efficiently than wild-type, suggesting a more buried or less flexible Trp environment. Together with the emission analysis (Figure 18), these data indicate mutation-specific rearrangements of the local tryptophan environment rather than a uniform unfolding effect.

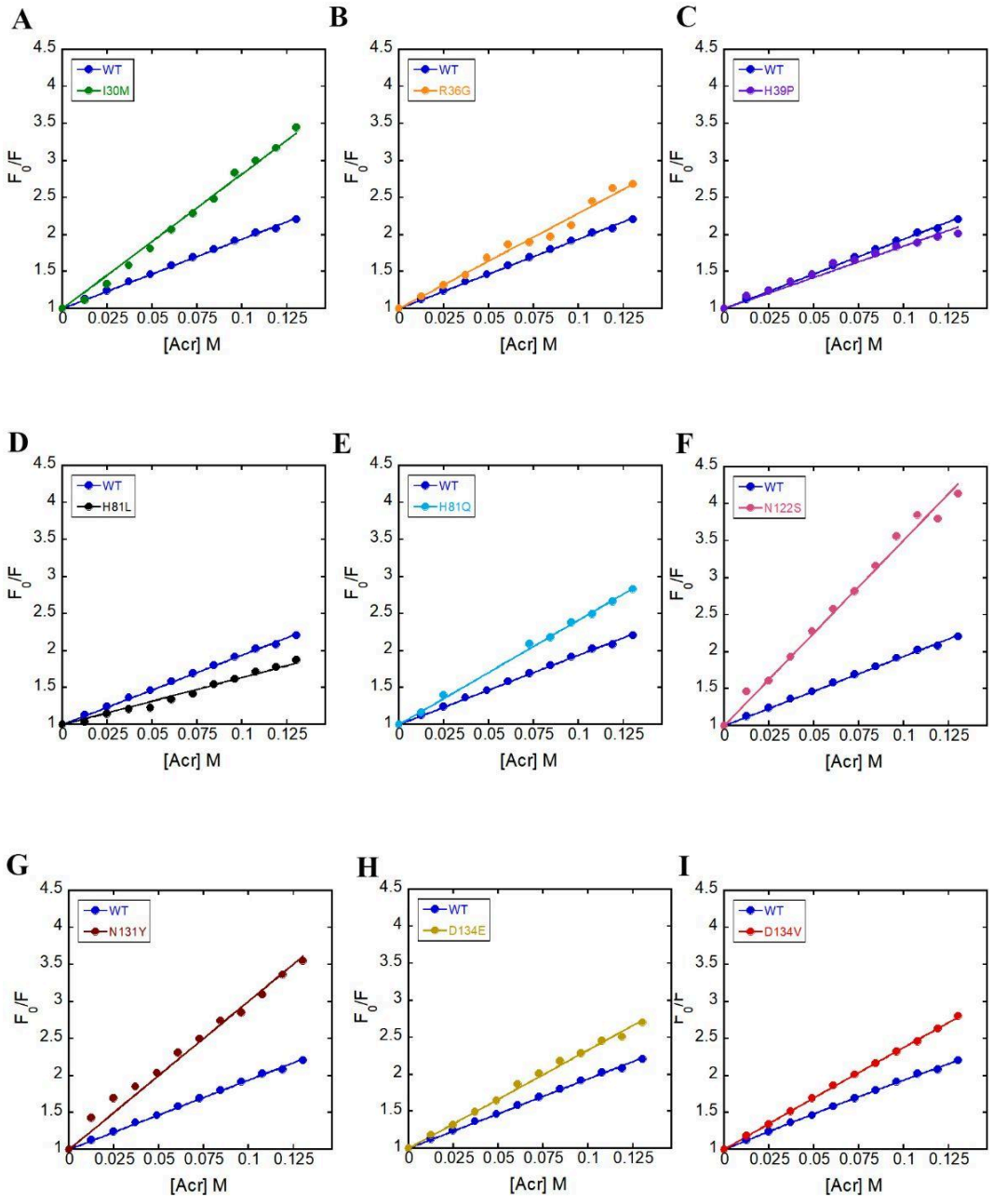

Figure 19. Acrylamide Stern–Volmer quenching of MPZ_{ex}.
(A–I) Stern–Volmer plots (F_0/F vs [Acrylamide] for wild-type (blue) and each variant with linear fits; the slope yields K_{SV}

4.1.5 DLS

DlS was used to quantitatively investigate the propensity to form aggregates. Measurements were performed on samples maintained at room temperature at three discrete time points: immediately following sample clarification through a 0.022 μm pore size filter (t=0), and after 24 and 48 hours of incubation.To quantitatively compare the aggregation kinetics of the different protein variants, a standardized data processing pipeline was applied to the DLS measurements. The signal corresponding to species with a hydrodynamic diameter (Dh) below 3 nm was excluded, as this is smaller than the theoretical size of monomeric MPZ_{ex} (~4.5 nm with simulation in Cryosol). The remaining signal was normalized and partitioned into three size classes: small species (3-30 nm), intermediate aggregates (30-300 nm), and large aggregates (>300 nm). We can observe that at t=0 the complete absence of the small species class for all variants, indicating that the monomeric form is highly unstable and rapidly self-associates into intermediate aggregates. The wild-type protein (Figure 20A) shows that the population is initially dominated by intermediate aggregates. Over the 48-hour time course, the relative population of intermediate aggregates decreases between the 24-hour and 48-hour time points, which is mirrored by a concomitant and significant increase in the fraction of large aggregates (>10000 nm). Variants I30M, R36G, and H81L, H81Q, N22S (panels C, E, F and G of Figure 20) showed a continuous and rapid accumulation of large aggregates that exceeded the wild-type. The D134V (panel L) variant exhibited a lag phase for the first 24 hours followed by a conversion to large aggregates by 48 hours. H39P, N131Y and D134E (panel D, H and I) rapidly formed a substantial population of large aggregates by 24 hours, only for this population to markedly decrease at the 48-hour time point, suggesting that the aggregates it forms are kinetically unstable and may be fragmenting or precipitating out of solution. A comparative analysis at the 24-hour (panek M) confirm these differences: while wild-type and D134V showed formation of less aggregates, nearly all other mutants had already converted a significant fraction of their population into large species, with H81L, N131Y, and D134E showing a particularly profound aggregation propensity at this intermediate time point.

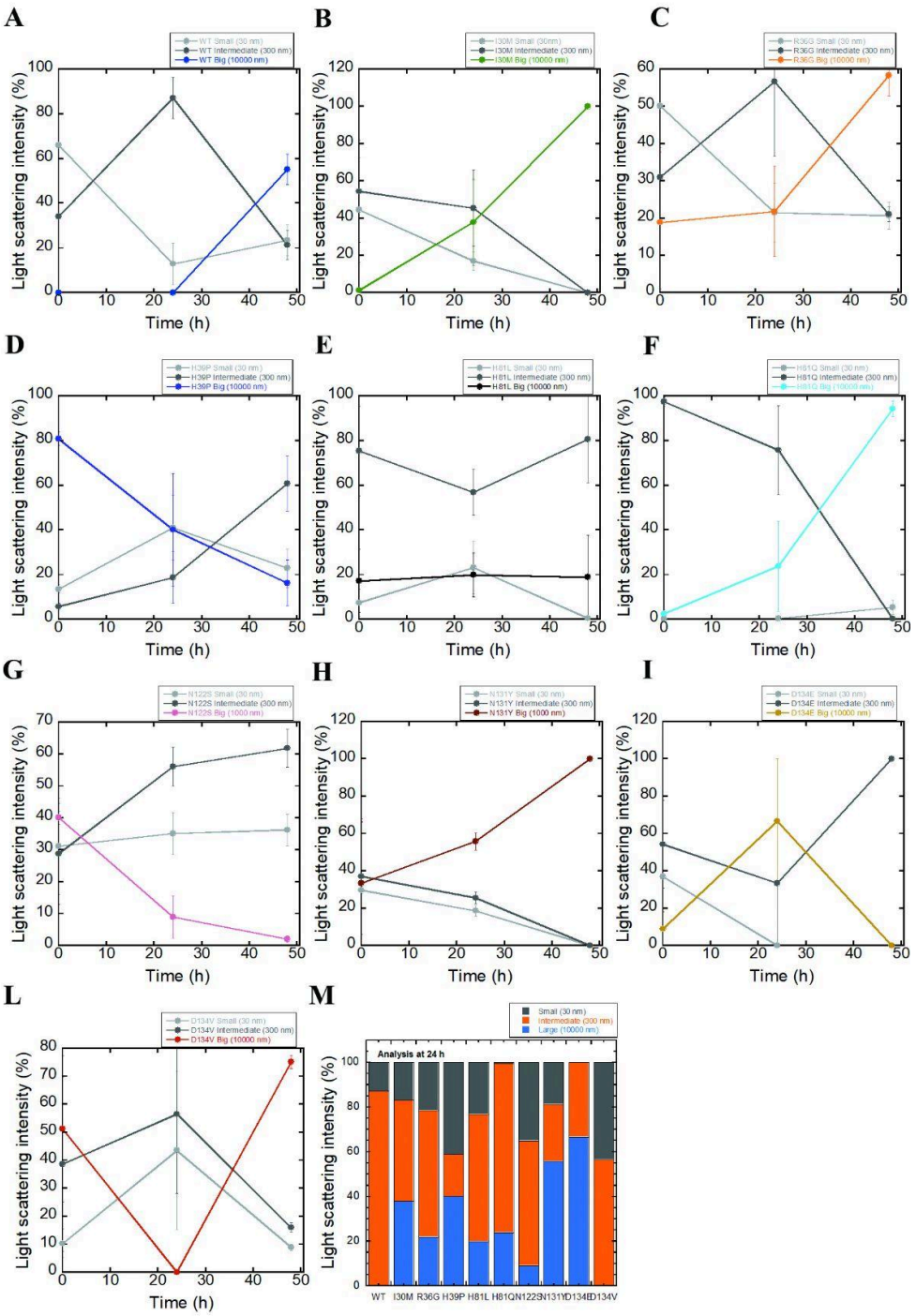

Figure 20. Time-course analysis of the aggregation of wild-type and mutant MPZ_{ex} by DLS. (A-L) Time-course evolution of the relative populations of different-sized species for wild-type MPZ_{ex} (A) and the indicated mutants (B-L). DLS measurements was taken at t=0, 24 h, and 48 h. The scattered light intensity signal was categorized into three populations based on D_h: Small Species (3-30 nm; grey), Intermediate Aggregates (30-300 nm;black), and Large Aggregates (>300;color-coded for each variant;). Data points represent the mean ± standard deviation of three independent measurements. (M) Comparative analysis of the aggregation state at the 24-hour time point. The stacked bar chart shows the percentage of the total scattered light intensity contributed by each of the three size classes for the wild-type protein and all investigated mutants.

4.1.6 (GndHCl)-Induced Denaturation

The stability of the MPZ_{ex} domains was assessed through GndHCl-induced unfolding, with protein denaturation monitored by changes in the far-UV CD signal at 222 nm. The resulting unfolding curves, displayed in Figure 21, were fitted to a two-state model to derive the key thermodynamic parameters: the ΔG_{U-F}^{H2O} and the midpoint denaturant concentration (C_m).

The results from the chemical denaturation experiments revealed significant differences in the stability profile of several CMT-associated mutants compared to the wild-type domain (Table 3).

The ΔG_{U-F}^{H2O} for the wild-type protein was determined to be 21875 ± 1094 J*mol^{-1} with a C_m of 1.95 M. The majority of the mutants displayed a severe loss of thermodynamic stability. I30M and H81Q exhibited the greatest destabilization, showing ΔG_{U-F}^{H2O} values of 11775 ± 589J *mol^{-1} , respectively. This substantial decrease in ΔG_{U-F}^{H2O} and indicate that these two substitutions compromise the overall structural integrity of the MPZ_{ex}.

R36G, H39P, H81L, N122S, and N131Y also showed reduced stability ,ranging from 9441 J*mol^{-1} to 10938 J*mol^{-1}. Conversely, the D134V mutant showed a ΔG_{U-F}^{H2O} of 21893 J*mol^{-1} and a C_m of 1.96 M, nearly identical to the wild-type protein, suggesting that this particular substitution does not significantly affect the equilibrium free energy difference between the native and fully unfolded states.

MPZ Variant	ΔG_{U-F}^{H2O} (J · mol^{-1})	*Cm* (M)
wild-type	21875±1094	1.95±0.10
I30M	11775±589	1.05±0.05
R36G	10697±535	0.96±0.05
H39P	9903±495	0.88±0.04
H81L	10432±522	0.93±0.05
H81Q	12204±610	1.09±0.05
N122S	12083±604	1.08±0.05
N131Y	10938±547	0.98±0.05
D134E	9441±472	0.84±0.04
D134V	21893±1095	1.96±0.10

Table 3. Wild-type and variants ΔG_{U-F}^{H2O} and C_m values ± standard error (**σ**).

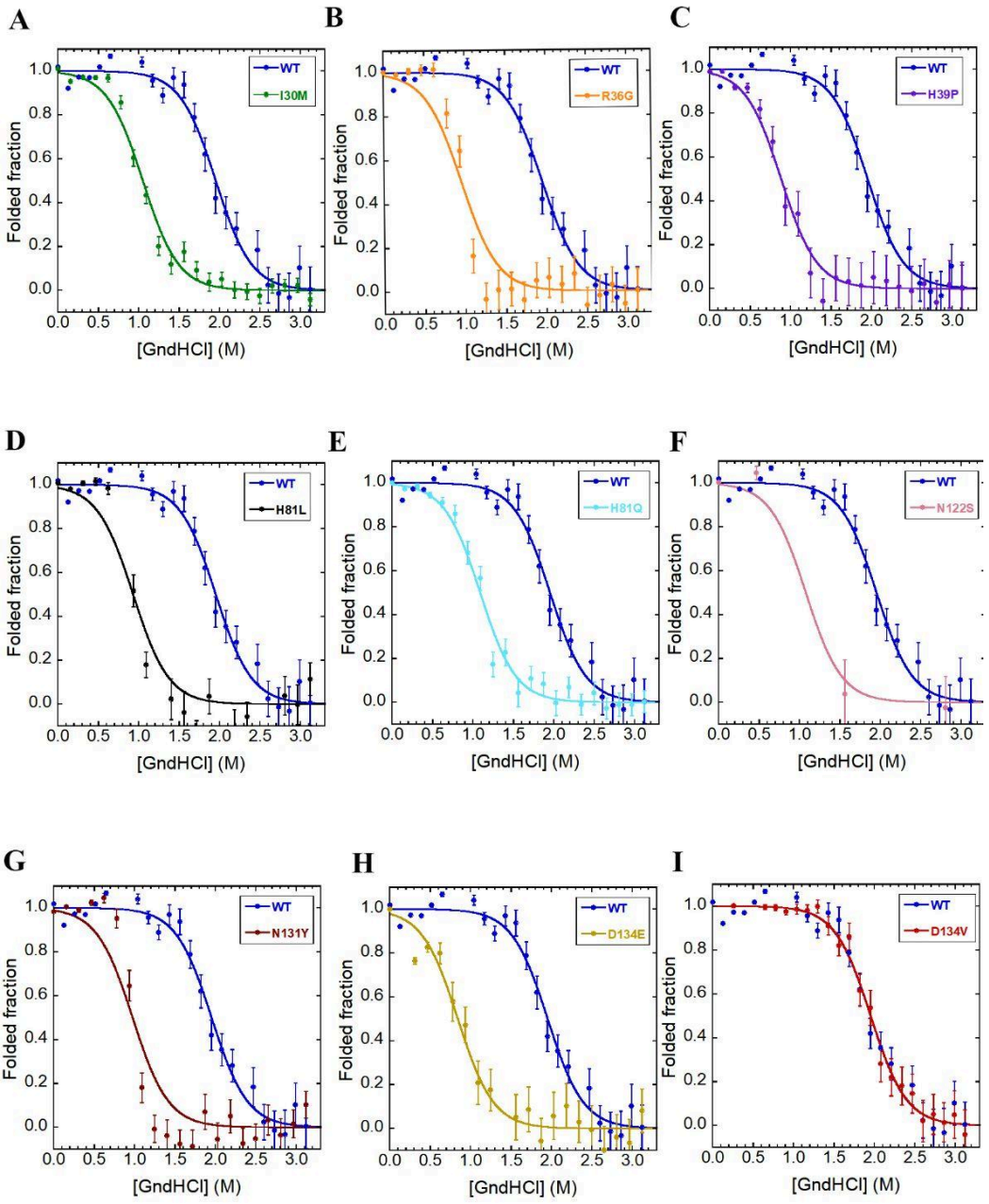

Figure 21. GndHCl-induced equilibrium unfolding of MPZ_{ex} domains monitored by far-UV circular dichroism at 222 nm. The data points were fitted using a two-state model to determine the thermodynamic parameters reported in Table 4. The blue line represents the fit for the wild-type protein in all plots.

4.1.7 DSF

To obtain a more comprehensive understanding of protein stability, investigated the thermal denaturation profiles of the MPZ_{ex} wild-type and its pathogenic variants using DSF. As shown in Figure 22, the fraction of folded protein was monitored as a function of temperature for each variant, allowing for the determination of the T_m, the point at which half of the protein population is unfolded. All variants displayed a cooperative, two-state thermal unfolding transition, characterized by a sigmoidal melting curve. The wild-type protein exhibited a T_m of 323.50 ± 0.20 K. In striking contrast to all other variants, the I30M mutant showed a significant increase in thermal stability, with a T_m of 328.30 ± 0.30 K, approximately 4.8 K higher than the wild-type. Conversely, all other mutants were significantly destabilized. The D134V, R36G, H81Q, and N122S variants showed a moderate decrease in stability, with T_m values of 317.50 K, 316.50 K, 316.60 K, and 315.61 K, respectively, corresponding to a destabilization (ΔT_m) ranging from -6.0 K to -7.9 K. A more severe destabilization was observed for H39P, H81L, and N131Y, which displayed ΔT_mvalues of approximately -9.7 K, -10.7 K, and -10.9 K. The D134E mutant was the most profoundly affected, with a T_m of 306.51 ± 0.20 K, representing a dramatic thermal destabilization of nearly 17 K. These results are only partially in agreement with data from chemical denaturation, providing complementary insights. For example, the I30M mutant, which is significantly stabilized thermally, was previously observed to be thermodynamically destabilized. Conversely, the D134V mutant shows a significant thermal destabilization (ΔT_m = -6.0 K) but previously exhibited a conformational stability comparable to the wild-type. Therefore, these thermal denaturation data are essential for a complete stability profile, demonstrating that thermodynamic stability and thermal resistance are not always directly correlated for these MPZ_{ex} variants.

MPZ Variant	T_m (K)
wild-type	323.50±0.20
I30M	328.30±0.30
R36G	316.50±0.10
H39P	313.80±0.90
H81L	312.84±1.13
H81Q	316.60±0.20
N122S	315.61±1.57
N131Y	312.58±0.18
D134E	306.51±0.20
D134V	317.50±0.20

Table 4. Wildtype and varians T_m (K) ± σ

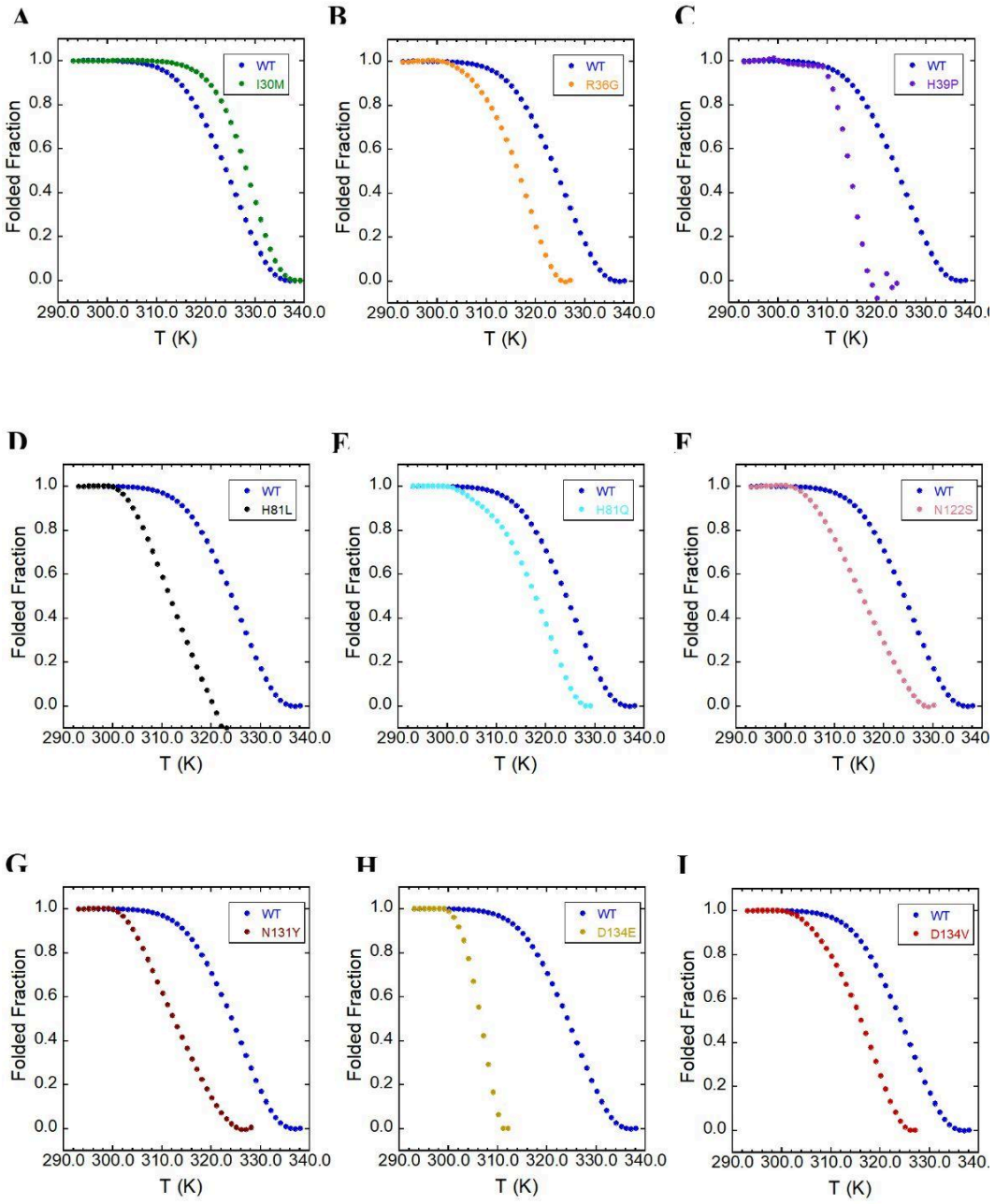

Figure 22. Thermal denaturation profiles of MPZ_{ex} variants. Thermal stability of the wild-type (wild-type) MPZex and the indicated mutants was assessed by Differential Scanning Fluorimetry (DSF). The fraction of folded protein is plotted as a function of temperature (K). Each panel (A-I) shows the cooperative, sigmoidal unfolding transition for a specific mutant (colored dots) overlaid with the curve for the wild-type protein (blue dots) for direct comparison.

4.1.8 Heterophilic binding pull down assay

To further dissect the functional consequences of the pathogenic mutations, the heterophilic binding capacity of MPZ_{ex} was evaluated. This was achieved by quantifying its interaction with a fluorescently labeled $PMP22_{ex}$-Alexa594, a known binding partner. Following a pull-down assay where MPZ_{ex} variants served as the immobilized bait, the fluorescence of the eluted $PMP22_{ex}$ peptide was measured. The resulting emission spectra (Figure 23, A-I) qualitatively demonstrate that all mutations lead to a reduction in binding affinity compared to the wild-type protein, which exhibits a robust fluorescence signal..

Quantitative analysis of the mean fluorescence intensity (Figure 23L) allowed for a precise classification of the functional impairment caused by each mutation. The wild-type protein established the baseline for effective binding with a fluorescence intensity of 9748.53 ± 938.04 a.u. The D134V and H81Q variants displayed only a modest reduction in binding, with intensities of 8079.83 ± 755.41 a.u. and 6746.57 ± 467.10 a.u., respectively. A more pronounced impairment was observed for the R36G mutant, which showed a nearly 50% decrease in binding capacity (4915.40 ± 15.80 a.u.). The most severe loss of binding was identified in a large group of mutants, including D134E, N122S, N131Y, H81L, I30M, and H39P, which all exhibited a dramatic reduction in fluorescence, with values ranging from ~4018 down to ~964 a.u.

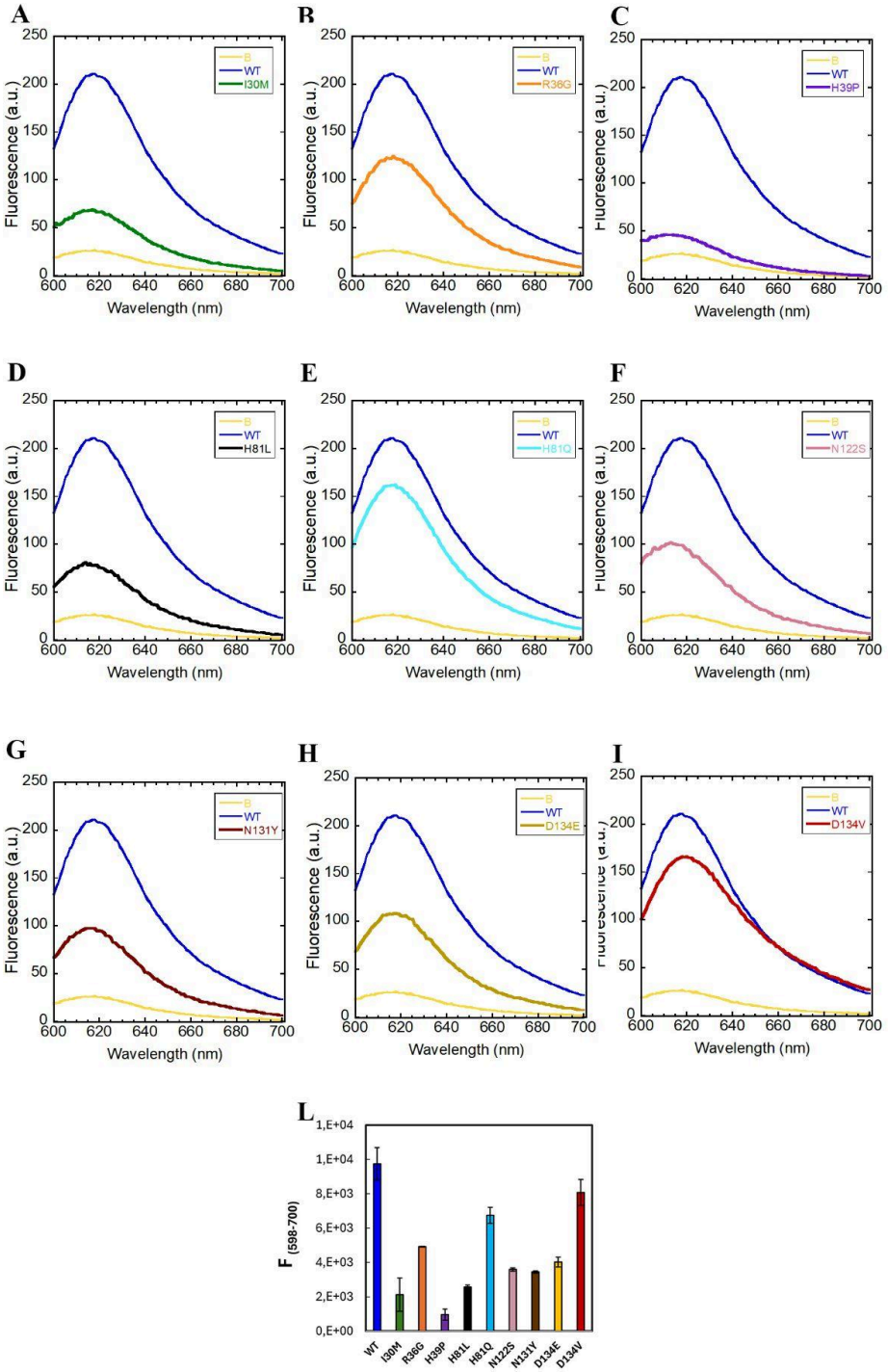

Figure 23. Heterophilic Interaction of MPZex Variants with PMP22ex Peptide. (A-I) Representative fluorescence emission spectra of eluted Alexa Fluor 594-labeled PMP22ex peptide after incubation with immobilized MPZex variants. Spectra were recorded following excitation at 590 nm. Each panel compares the binding capacity of a specific mutant (colored line) to that of the wild-type protein (blue line), illustrating the varying degrees of binding impairment. (L) Quantitative analysis of the heterophilic interaction. The bar chart displays the mean fluorescence intensity (± standard deviation, n=3) of the eluted PMP22ex peptide for the wild-type and each mutant.

4.1.9 Homophilic binding pull down assay

To investigate the impact of pathogenic mutations on the self-adhesion properties of the MPZ_{ex} domain, a fluorescent pull-down assay was employed to assess homophilic binding. The fluorescence emission spectra of the eluted, BODIPY™-labeled protein provide a qualitative overview of these interactions (Figure 24). The spectra, acquired with an excitation at 540 nm, show a distinct and high-intensity emission peak around 575 nm for the wild-type protein, indicating a strong homophilic interaction that allows the immobilized wild-type bait to capture a significant amount of fluorescent prey. In contrast, the negative control (blank), containing only resin, exhibits a negligible signal, confirming that non-specific binding of the labeled protein to the Ni-NTA resin is minimal. The various mutants display a wide range of signal intensities, suggesting that the mutations have diverse effects on binding affinity.

For a robust quantitative comparison, the mean fluorescence intensity of the eluted fraction for each variant was measured and corrected by subtracting the signal from the blank control (Figure 24L). The wild-type protein, with a mean fluorescence of approximately 20,204 a.u., serves as the benchmark for strong self-association. The I30M mutant exhibited a slightly enhanced binding affinity (~21,196 a.u.) compared to the wild-type. A second group of mutants, including H81Q (~18,965 a.u.), N122S (~16,544 a.u.), and H81L (~14,817 a.u.), retained substantial binding capability, showing fluorescence intensities comparable to the wild-type. However, a third group of mutants demonstrated a profound loss of binding. The R36G, H39P, N131Y, D134V, and D134E variants all displayed a severe impairment in homophilic binding, with mean fluorescence intensities dramatically reduced to approximately 4,643, 4,200, 3,708, 4,463, and 7,260 a.u., respectively. This represents a 60-80% reduction in binding compared to the wild-type.

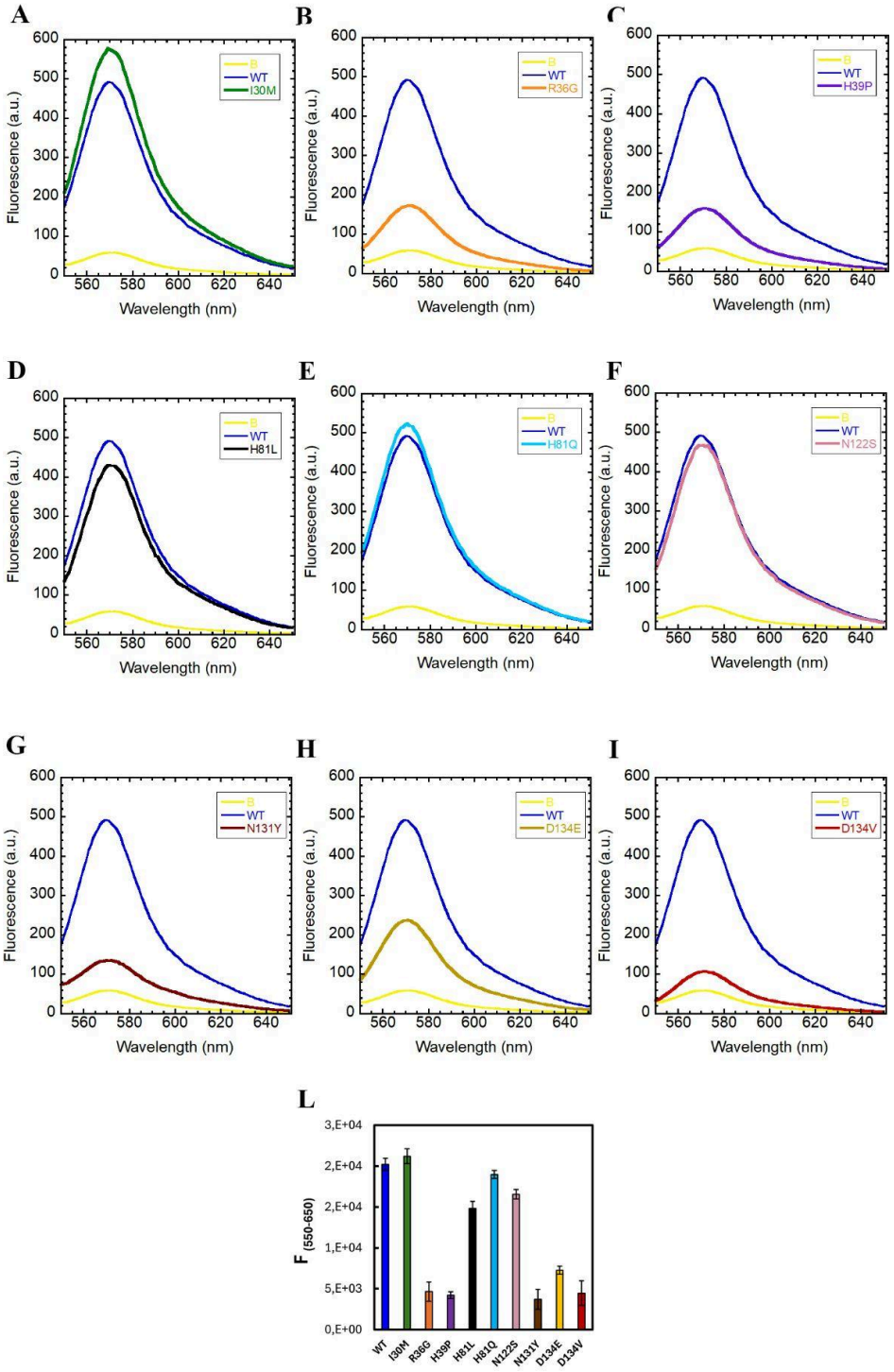

Figure 24. Homophilic Binding Affinity of MPZex Variants Assessed by a Fluorescent Pull-Down Assay. (A) Representative fluorescence emission spectra of eluted MPZex-BODIPY™ prey. Spectra were recorded from 560 to 640 nm (excitation at 540 nm). The high signal for the wild-type indicates strong binding, while the negligible signal for the blank (resin only) confirms low non-specific interaction. Spectra for various mutants show a range of binding capacities. (B) Quantitative analysis of homophilic binding. The bar chart displays the background-subtracted mean fluorescence intensity (± standard deviation, n=3) of the eluted protein for the wild-type and each mutant, providing a direct comparison of their relative binding affinities.

4.2 Discussion

MPZ is the most abundant protein in the PNS myelin sheath, where it functions as the primary molecular adhesive responsible for compacting adjacent membrane layers[17]. This essential role is mediated by the homophilic interactions of its extracellular Ig domain, which forms a dense, quasi-crystalline lattice that constitutes the IPL visible in electron micrographs[38]. The precise molecular architecture of this adhesive interface remains an area of active investigation, with competing models proposing either a "zipper-like" framework of trans-dimers[54] or higher-order assemblies built from cis-tetrameric units [55,56]. Regardless of the specific arrangement, the structural integrity of the MPZ_{ex} monomer is paramount for generating the robust adhesive force required for myelin formation and maintenance[37]. Consequently, over 100 pathogenic mutations in the MPZ gene have been identified as a cause of CMT disease, giving rise to a remarkably broad spectrum of clinical phenotypes[79]. The molecular basis for this heterogeneity is understood to arise from at least three distinct pathomechanisms[69]. The most severe, early-onset demyelinating neuropathies are often attributed to a toxic gain-of-function mechanism, whereby misfolded MPZ variants are retained in the ER, triggering a chronic UPR that leads to Schwann cell apoptosis[57,100]. A second mechanism involves a primary structural failure, where mutations on the protein surface impair adhesive function without causing gross misfolding, resulting in an unstable myelin sheath[52,56] . The third, haploinsufficiency, arises from null alleles and leads to a milder, late-onset neuropathy due to an insufficient dosage of functional protein for long-term myelin maintenance [62].

The present study leverages a comprehensive biophysical and functional analysis of a panel of nine pathogenic MPZ_{ex} variants, including the novel D134V mutation, to move beyond these discrete categories. A foundational requirement for MPZ function is its ability to adopt and maintain a stable Ig-like fold [38]. Far-UV CD spectra showed that most mutants retain the overall β-sheet secondary structure characteristic of the MPZ_{ex} Ig-fold. However, clear mutation-specific alterations in CD signal intensity indicate subtle conformational changes for each variant. Notably, H39P had the most bad effect on secondary structure, producing a greatly diminished and flattened CD spectrum lacking a defined 217 nm minimum. This suggests a ructural perturbation, which is expected since replacing

a β-strand residue with proline breaks normal backbone hydrogen bonding and can distort the Ig scaffold. The severity of H39P's structural disruption is consistent with clinical reports that H39P causes a neuropathy (CMT1B/CMT2) despite relatively late onset– the variant yields a partially folded protein (functional studies classify it as a partial loss-of-function) that likely only marginally supports myelin stability [52,110]. By contrast, I30M and R36G – both in the N-terminal β-sheet – showed CD spectra virtually superimposable on wild-type, indicating that their Ig-domain secondary structure remains intact. This aligns with predictions from molecular dynamics that mutations at Ile^30 induce more dynamic subtle changes rather than wholesale unfolding[107]. Nonetheless, the preservation of secondary structure in I30M and R36G belies significant underlying instability (discussed below). The two mutants at residue 81 (H81Q and H81L, in β-strand C′) likewise retained a wild-type-like CD profile with only moderate reductions in ellipticity, suggesting the Ig fold remains largely intact. This is somewhat surprising given that His^81 lies in the hydrophobic core; evidently, both a polar glutamine and a hydrophobic leucine can be accommodated in the core without completely disrupting secondary structure, although each causes subtle shifts in packing or flexibility. Meanwhile, the glycosylation-site mutant N122S had essentially no change in CD, implying that in the absence of glycosylation (our bacterially expressed proteins are non-glycosylated), the Asn→Ser substitution does not alter the secondary structure – the Ig scaffold remains intact. The conserved fold of N122S in vitro suggests that the pathogenicity of this variant (CMT1B, childhood-onset) likely arises from other factors such as impaired folding in the cell or loss of the stabilizing N-linked glycan in vivo, rather than an inherent inability to form the β-sheet structure. N131Y (β-strand F) and D134V (FG loop) both showed the characteristic 217 nm minimum but with reduced magnitude, indicating a slight loss of ordered secondary structure content or increased disorder. The conservative D134E mutation had only a minor CD attenuation, whereas the nonconservative D134V caused a larger decrease in ellipticity despite maintaining a broadly similar spectral shape. This trend confirms that even in the absence of large secondary structure rearrangements, D134V induces more pronounced structural perturbations than D134E – consistent with the idea that D134 is a key structural hotspot under evolutionary pressure. Overall, the CD analysis

demonstrates that each mutant spans a continuum from near-native secondary structure (e.g. I30M, N122S) to markedly altered (H39P, D134V), mirroring how some mutants preserve the Ig-fold architecture while others destabilize it.

Fluorescence spectroscopy and tryptophan quenching experiments further highlighted mutation-specific conformational effects, especially on the local environment and dynamics of MPZ's aromatic core. Wild-type MPZ_{ex} has intrinsic tryptophan fluorescence with a center-of-mass emission around 364 nm, typical of a partially solvent-exposed Trp environment. Most mutants exhibited modest blue-shifts in emission (λ_{cm}~ 355–363 nm), indicating their Trp residues are in a slightly more buried or rigid environment compared to wild-type. The largest blue shifts were observed for H39P and D134V (both ~6–8 nm), suggesting these mutations induce a significant rearrangement that shields Trp fluorescence from solvent – likely due to altered tertiary packing or aggregation. Indeed, H39P's fluorescence intensity remained similar to wild-type even as its peak shifted blue, implying that the Trp residues became buried without drastic quenching. In contrast, D134V showed not only a blue-shift but also the most drastic drop in fluorescence intensity (almost halved). This quenching of Trp fluorescence in D134V is consistent with formation of non-native contacts or higher-order aggregates that statically quench fluorescence – a hallmark of its metastable, aggregation-prone state. A subset of mutants (I30M, H81L, D134E, N122S) exhibited increased fluorescence intensity (1.5-fold higher than wild-type) alongside slight blue or even red shifts. For example, I30M and H81L had higher intensity and small blue-shifts (~361–363 nm), whereas N122S uniquely showed a slight red-shift (~366 nm) coupled with intensity increase. The intensity elevation suggests a less quenched Trp environment – possibly a more rigid structure preventing non-radiative decay, or altered side-chain interactions that reduce quenching. The subtle red-shift for N122S indicates Trp becomes marginally more solvent-exposed or polar-environment accessible (consistent with removal of the bulky N-glycan perhaps creating a local cavity accessible to water). Meanwhile, R36G, H81Q, and N131Y displayed fluorescence spectra very close to wild-type (only minor blue-shifts of ~1–3 nm and intensities within ±20% of wild-type). This suggests these three mutants cause relatively small perturbations in the Trp environment at equilibrium – consistent with their

near-native CD spectra (R36G, N131Y) or only moderate changes (H81Q). To probe Trp exposure quantitatively, we performed acrylamide quenching, which supported the fluorescence findings. The Stern–Volmer quenching constant (K_{sv}) for wild-type was ~9.4 M^{-1}. Several mutants showed dramatically higher K_{sv} N122S, N131Y, and I30M – indicating that acrylamide can access the Trp residues much more readily in these variants. Such high quenching efficiency reveals a more solvent-exposed or dynamically flexible Trp environment, consistent with these mutations destabilizing local structure. In particular, the loss of glycosylation in N122S appears to have rendered Trp(s) far more accessible, supporting the notion that the glycan normally shields or structurally supports part of the Trp region in MPZ_{ex}. Likewise, I30M's high K_{sv} suggests that even though its CD spectrum was native-like, the protein likely samples an "open" or flexible conformation exposing interior residues – an insight aligned with its thermodynamic instability discussed below (and indeed in silico studies on I30T/M predicted increased structural fluctuation[107]). In contrast, H81L and H39P had lower quenching than wild-type (K_{sv} ~6.4 and 8.1, respectively), indicating their Trp residues are less accessible – likely buried in aggregates or in a tightened hydrophobic core. This correlates with the pronounced blue-shift for H39P (Trp trapped in a hydrophobic pocket) and suggests H81L may induce a rigid core packing that limits solvent penetration. The remaining mutants (H81Q, D134V, D134E, R36G) showed moderately elevated K_{sv} values, signifying somewhat increased Trp exposure relative to wild-type. Together, the fluorescence and quenching data paint a picture of mutation-specific rearrangements of the MPZ_{ex} tertiary structure: for some, a loosening and exposure of the hydrophobic core (e.g. N122S, I30M); for others, aberrant burial or aggregation of core residues (H39P, D134V); and for yet others, relatively minor local perturbations (R36G, H81Q). Importantly, these changes are not uniform unfolding but rather distinct conformational shifts unique to each variant, reinforcing that each mutation perturbs MPZ_{ex} in its own way.

Despite many mutants maintaining a folded secondary structure, equilibrium chemical denaturation exposed significant instabilities. GndHCl unfolding experiments revealed that most disease-linked variants have a substantially

reduced free energy of unfolding (ΔG_{U-F}^{H2O}) compared to wild-type (~21.9 kJ/mol). In fact, all mutants except D134V showed ΔG_{U-F}^{H2O}values roughly half of wild-type or even less. The greatest destabilization was seen with I30M (ΔG_{U-F}^{H2O} ~11.8 kJ/mol) and H81Q (~12.2 kJ/mol), indicating these two substitutions drastically compromise the thermodynamic stability of the Ig domain. This is mechanistically consistent with their locations in crucial β-strands: Ile^30 anchors strand B in the hydrophobic core, and replacing it with a slightly bulkier hydrophobic side chain may introduce packing strain that destabilizes the folded state[107]. Likewise, His^81 in strand C′ normally forms hydrogen bonds and hydrophobic contacts; H81Q likely alters those interactions (introducing an unpaired polar side chain in the core) and H81L removes a potential hydrogen bond donor. The severe ΔG_{U-F}^{H2O} drop for H81Q suggests that even though its folded state can form, it is much less energetically favorable – likely causing a fraction of H81Q proteins to misfold or aggregate in vivo, which would explain its association with early-onset demyelinating CMT1B. Other mutants exhibited significant but somewhat smaller stability losses: R36G (~10.7 kJ/mol), H39P (~9.9), H81L (~10.4), N122S (~12.1), N131Y (~10.9), and D134E (~9.4 kJ/mol). These values (all roughly 40–55% of wild-type stability) demonstrate that each of these pathogenic mutations renders MPZex substantially less stable, which in a cellular context likely means a propensity to misfold or unfold under physiological stress. The case of D134E is particularly telling – substituting Asp for a structurally conservative Glu still cut the stability by more than half, underscoring how critical the D134 position is. Asp^134 sits at the juncture of the FG loop with the β-sandwich core and likely forms specific contacts (electrostatic or hydrogen bonds) that Glu cannot maintain due to its extra methylene; the result is a destabilized native state. Intriguingly, one mutant did not follow the trend: D134V had ΔG_{U-F}^{H2O} (~21.9 kJ/mol) and midpoint (1.96 M) essentially identical to wild-type. This paradox, suggests that D134V's deleterious effect lies not in the thermodynamic difference between folded and unfolded states, but rather in folding kinetics or in the protein's response to perturbations, as already discussed in chapter 3.2. Indeed, when we examine thermal denaturation, a very different

picture emerges. DSF showed that all mutants except I30M have reduced T_m relative to wild-type (323.5 K). The magnitude of decrease correlated broadly with instability: H39P, H81L, and N131Y had some of the largest ΔT_m (−9.7, −10.7, −10.9 K, respectively), reflecting their severe destabilization of the folded structure – in line with their significantly lowered ΔG_{U-F}^{H2O}. D134E was the most extreme, with T_m ~306.5 K (a whopping ~17 K drop), consistent with it having the lowest ΔG_{U-F}^{H2O} of the panel. More moderate T_m losses (~6–8 K) were seen for D134V, R36G, H81Q, and N122S, again roughly matching their moderate ΔG_{U-F}^{H2O} deficits. The most remarkable outlier was I30M: it increased the thermal stability, with T_m = 328.3 K (~4.8 K higher than wild-type). This result indicates that I30M's folded state is unusually resistant to thermal unfolding – perhaps due to enhanced hydrophobic packing by Met which raises the kinetic barrier for unfolding. Yet paradoxically, I30M had one of the lowest equilibrium stabilities (ΔG_{U-F}^{H2O} ~11.8 kJ/mol). In summary, our stability analyses reveal two important points: (i) most pathogenic MPZ mutations significantly destabilize the Ig domain, reducing the energetic favorability of the properly folded state – a unifying theme for how they cause disease (by failing to maintain a stable adhesive conformation); and (ii) certain mutations introduce discrepancies between thermodynamic and kinetic stability (exemplified by I30M and D134V), highlighting that protein stability is multi-dimensional.

Consistent with their destabilization, many variants showed enhanced tendency to aggregate. The mutants aggregated faster or more extensively. By 24 h, most variants had already accumulated a higher fraction of large aggregates than wild-type. In particular, I30M, R36G, H81L, H81Q, and N122S showed a "continuous and rapid" increase in large aggregate population from t=0 to 24 h (and further by 48 h). H39P, N131Y, and D134E each formed a substantial large-aggregate population already by 24 h, but then that population decreased by 48 h. This transient aggregation suggests that the large aggregates they form are not stable – they may precipitate out of solution or fragment into smaller species over time. A plausible interpretation is that these three mutations cause such misfolded conformations that the aggregates coalesce and then fall out of solution

(precipitation), effectively reducing measurable large particles at later time points. Mutants that are highly destabilized (e.g. D134E, N131Y, H39P) aggregate very rapidly (but possibly into insoluble precipitates), whereas those with intermediate stability deficits (I30M, H81 variants, N122S, R36G) still aggregate faster than wild-type over time. These tendencies correlate with the clinical picture: the most aggregation-prone variants correspond to severe demyelinating CMT1B (which can involve toxic gain-of-function via protein aggregation in Schwann cells[57]), whereas milder CMT2 mutants, while still aggregation-prone in vitro, may aggregate less in vivo or on a longer timescale (hence later onset of pathology).

Ultimately, MPZ's biological role is to mediate adhesion – both homophilic (MPZ–MPZ) and potentially heterophilic (MPZ with other myelin proteins). We assessed these interactions using pull-down assays with fluorescently labeled binding partners. In the heterophilic assay, we tested binding of MPZ_{ex} variants to a peptide from PMP22's extracellular loop. The wild-type MPZ_{ex} showed robust binding to PMP22ex peptide, consistent with early reports that MPZ and PMP22 can form a complex in peripheral myelin[116,117]. All mutations caused some reduction in PMP22 peptide binding signal, but there was a gradation. D134V and H81Q retained the highest binding (fluorescence only modestly reduced relative to wild-type. R36G showed an intermediate ~50% loss of binding. The majority of mutants – including I30M, H39P, H81L, N122S, N131Y, and D134E – exhibited a drastic loss of peptide binding (only ~10–40% of wild-type signal). This severe reduction implies significant structural distortion or occlusion of the binding interface in these variants. However, it is critical to interpret these in vitro results with caution: subsequent studies have shown that the physiologically relevant MPZ–PMP22 interaction occurs via their transmembrane domains, not the extracellular domains[61] . Thus, the heterophilic binding assay here is probing a non-native interaction – essentially the ability of a mutant MPZ_{ex} to nonspecifically bind a PMP22 peptide. The dramatic loss of binding in many mutants probably reflects overall misfolding. The relatively preserved binding by D134V and H81Q could mean these mutants, while unstable, still transiently populate a native-like conformation capable of interacting with PMP22ex in vitro. Importantly, since MPZ–PMP22 adhesion in myelin is predominantly via TMs,

even mutants that bind the peptide here might still fail in vivo if their extracellular instability allosterically affects transmembrane alignment.

The homophilic binding assay directly tested the ability of mutant MPZ_{ex} to adhere to wild-type MPZ_{ex}. The wild-type protein, by this assay, has strong self-association (set as 100% reference). The variants exhibited three tiers of behavior. First, remarkably, I30M showed slightly enhanced homophilic binding (~105% of wild-type). This suggests that when properly folded, I30M MPZ might form adhesive contacts as well as or even better than the native protein – possibly the Met^30 side chain promotes tighter hydrophobic inter-molecular contacts in the dimer interface. The second group of mutants retained substantial homophilic binding, albeit somewhat reduced: H81Q (~94% of wild-type), N122S (~82%), and H81L (~73%). Functionally, these proteins can still engage in homophilic adhesion nearly as well as the wild-type in vitro. Finally, a third group of mutations exhibited a drastic loss of homophilic binding capacity (only ~20–40% of wild-type): these include R36G, H39P, N131Y, D134V, and D134E. In these cases, the mutant MPZex cannot effectively engage in self-adhesion. This finding correlates strongly with the severe demyelinating phenotypes of these mutations. For instance, H39P and N131Y both cause early or severe neuropathy, and here we see they fail to homodimerize – structurally, H39P's distorted Ig domain and N131Y's alteration of a likely adhesion interface residue (Asn^131 is thought to participate in the trans-binding interface) mean that these proteins cannot fulfill their primary role as myelin glue. The D134 substitutions likewise severely impair adhesion: D134E retains only ~36% binding and D134V ~22%. We surmise that residue 134, located in the FG loop, is directly or indirectly involved in the homophilic binding interface or required for maintaining the Ig-domain alignment during adhesion ([56]Ptak et al., 2023 noted that many pathogenic mutations in this region abrogate MPZ's homomeric interactions).

Principal Component Analysis (PCA) of Mutant Profiles:

To integrate the complex biophysical dataset and visualize the relationships between protein defects and clinical outcomes, a Principal Component Analysis (PCA) was performed. This analysis provides a powerful framework for decoding the clinical heterogeneity of MPZ-related neuropathies by revealing how each

mutation imparts a distinct "biophysical signature." An analysis focused on stability and aggregation (Figure 25A) showed that the first principal component (PC1), capturing ~74% of the variance, acts as a "stability vs. aggregation" axis. Variants with high positive scores, such as D134E, are characterized by low stability and high aggregation, correlating with severe, early-onset demyelinating phenotypes. Conversely, variants with negative scores, like D134V and wild-type, exhibit higher thermodynamic stability. A second PCA focused on functional parameters (Figure 25B) revealed that its PC1, explaining ~44% of the variance, is strongly influenced by homophilic binding and tryptophan exposure (K_{sv}). Variants like I30M, N122S, and N131Y cluster with negative PC1 scores, indicating a severe loss of homophilic adhesion and a more open conformation.

The final, holistic PCA incorporating all experimental variables (Figure 25C) provides the most integrated view, with PC1 and PC2 explaining approximately 47% and 23% of the variance, respectively. The distribution of variants in this space allows for their classification into pathogenic trends that correlate strongly with clinical outcomes. Variants associated with severe, early-onset demyelinating phenotypes (e.g., D134E, N131Y) are positioned towards the extremes of the plot, driven by their profound instability and functional loss. This is consistent with a Severe Misfolding and Aggregation mechanism, where a toxic gain-of-function overwhelms the UPR, causing a developmental failure of myelination[114,115,125] . In contrast, late-onset axonal variants (R36G, H81L) occupy a more central position, reflecting their milder biophysical defects and a mechanism of instability and mixed pathogenesis, which allows for initial myelination but leads to slow degeneration of the axon-myelin unit over decades[108,112]. The unique position of D134V as an outlier in all analyses underscores its distinct pathogenic mechanism.

This work, therefore, provides a structure-based framework for decoding the clinical heterogeneity of MPZ neuropathies. By establishing correlations between specific molecular defects and clinical phenotypes, this model has significant implications for diagnostics and therapeutics. Subjecting novel MPZ variants to this biophysical analysis could enable the prediction of disease severity, while the elucidation of distinct pathogenic trends underscores the need for

mechanism-based therapies. The unique profile of D134V, in particular, highlights that a one-size-fits-all approach is unlikely to succeed, paving the way for a future of personalized medicine in Charcot-Marie-Tooth disease.

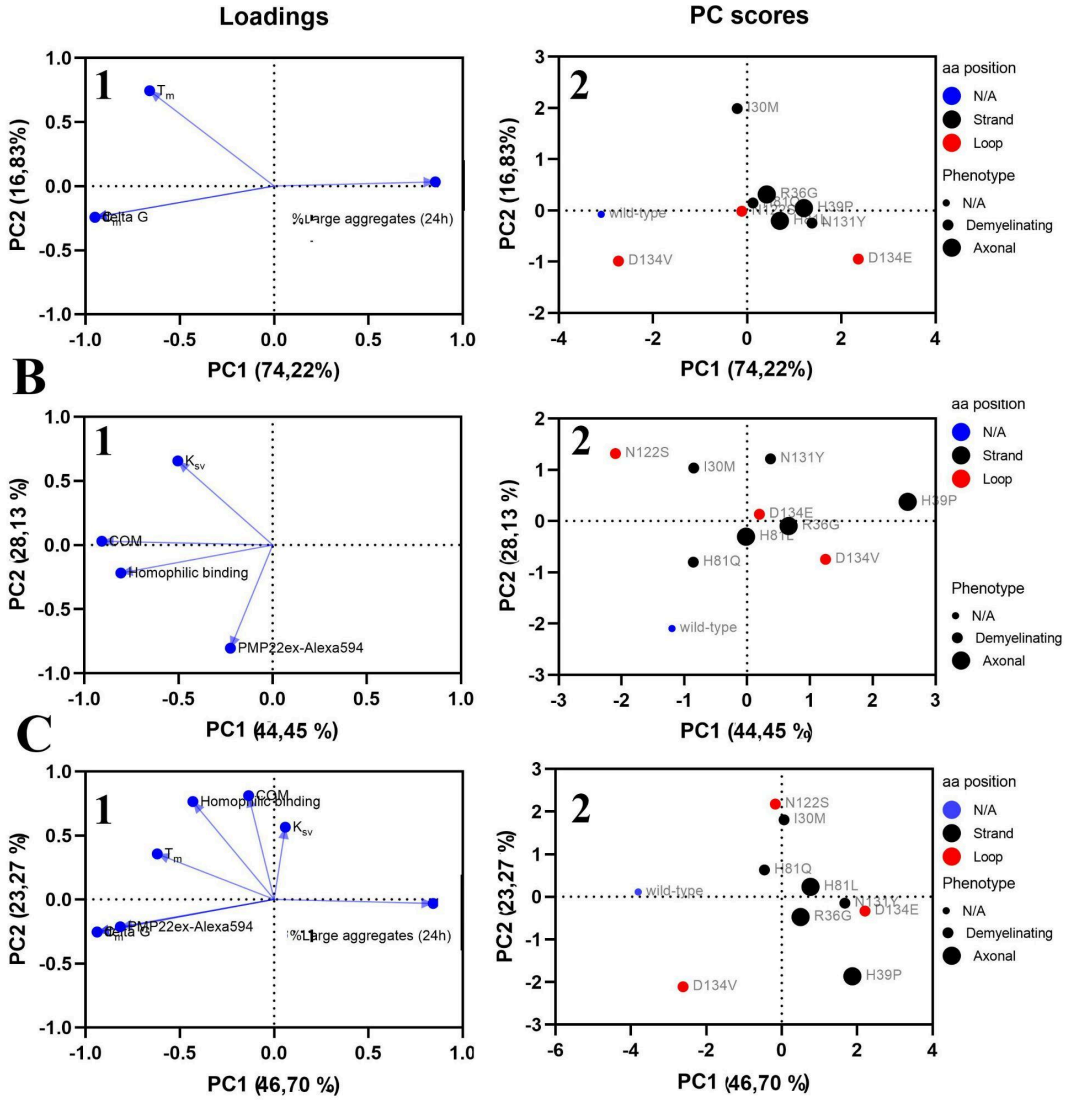

Figure 25. PCA of Biophysical and Functional Parameters for MPZex Variants. The figure shows three distinct PCAs, each with a loadings plot (left panels, 1) showing the contribution of each variable to the principal components, and a corresponding scores plot (right panels, 2) showing the distribution of the wild-type and mutant variants.(A)PCA focused on stability and aggregation parameters (T_m, ΔG, and % large aggregates at 24h) (B)PCA focused on functional parameters, including homophilic and heterophilic binding, and tryptophan solvent exposure (Ksv, COM).C PCA incorporating all experimental variables. .In all scores plots, variants are color-coded by their structural location (blue for β-strand, red for loop) and shape-coded by their clinical phenotype (circle for demyelinating, diamond for axonal). The wild-type protein is shown as a black circle.

References

1. Le Pichon, C. E. & Chesler, A. T. The functional and anatomical dissection of somatosensory subpopulations using mouse genetics. *Front. Neuroanat.* **8**, (2014).

2. Stifani, N. Motor neurons and the generation of spinal motor neurons diversity. *Front. Cell. Neurosci.* **8**, (2014).

3. LeBouef, T., Yaker, Z. & Whited, L. Physiology, Autonomic Nervous System. in *StatPearls* (StatPearls Publishing, Treasure Island (FL), 2025).

4. Murtazina, A. & Adameyko, I. The peripheral nervous system. *Development* **150**, dev201164 (2023).

5. Maroto-Gómez, M., Castro-González, Á., Malfaz, M., Fernández-Rodicio, E. & Salichs, M. Á. Modeling Neuroendocrine Autonomic Responses in Embodied Autonomous Robots. *Adv. Intell. Syst.* **5**, 2200288 (2023).

6. Andreeva, D., Murashova, L., Burzak, N. & Dyachuk, V. Satellite Glial Cells: Morphology, functional heterogeneity, and role in pain. *Front. Cell. Neurosci.* **16**, (2022).

7. Morell, P. & Quarles, R. H. The Myelin Sheath. in *Basic Neurochemistry: Molecular, Cellular and Medical Aspects. 6th edition* (Lippincott-Raven, 1999).

8. Alhamdi, A. A., Mackie, S., Trueman, R. P. & Rayner, M. L. D. Pharmacologically targeting Schwann cells to improve regeneration following nerve damage. *Front. Cell Dev. Biol.* **13**, (2025).

9. Murtazina, A. & Adameyko, I. The peripheral nervous system. *Dev. Camb. Engl.* **150**, dev201164 (2023).

10. Zalc, B. & Colman, D. R. Origins of vertebrate success. *Science* **288**, 271–272 (2000).

11. Rasband, M. N. & Peles, E. Mechanisms of node of Ranvier assembly. *Nat. Rev. Neurosci.* **22**, 7–20 (2021).

12. Pereira, J. A., Lebrun-Julien, F. & Suter, U. Molecular mechanisms regulating myelination in the peripheral nervous system. *Trends Neurosci.* **35**, 123–134 (2012).

13. Jessen, K. R. & Mirsky, R. The Success and Failure of the Schwann Cell Response to Nerve Injury. *Front. Cell. Neurosci.* **13**, 33 (2019).

14. Hartline, D. K. & Colman, D. R. Rapid conduction and the evolution of giant axons and myelinated fibers. *Curr. Biol. CB* **17**, R29-35 (2007).

15. Laura, F. M., Yannick, P. & Carlo, P. S. How Schwann Cells Sort Axons: New Concepts. *Neurosci. Rev. J. Bringing Neurobiol. Neurol. Psychiatry* **22**, 252–265 (2016).

16. Monk, K. R., Feltri, M. L. & Taveggia, C. New insights on schwann cell development. *Glia* **63**, 1376–1393 (2015).

17. Salzer, J. L. Schwann cell myelination. *Cold Spring Harb. Perspect. Biol.* **7**, a020529 (2015).

18. Court, F. A., Wrabetz, L. & Feltri, M. L. Basal lamina: Schwann cells wrap to the rhythm of space-time. *Curr. Opin. Neurobiol.* **16**, 501–507 (2006).

19. Court, F. A. *et al.* Restricted growth of Schwann cells lacking Cajal bands slows conduction in myelinated nerves. *Nature* **431**, 191–195 (2004).

20. Chang, K.-J., Redmond, S. A. & Chan, J. R. Remodeling myelination: implications for mechanisms of neural plasticity. *Nat. Neurosci.* **19**, 190–197 (2016).

21. Feltri, M. L. & Wrabetz, L. Laminins and their receptors in Schwann cells and hereditary neuropathies. *J. Peripher. Nerv. Syst.* **10**, 128–143 (2005).

22. Stassart, R. M., Möbius, W., Nave, K.-A. & Edgar, J. M. The Axon-Myelin Unit in Development and Degenerative Disease. *Front. Neurosci.* **12**, (2018).

23. Nave, K.-A. & Werner, H. B. Myelination of the Nervous System: Mechanisms and Functions. *Annu. Rev. Cell Dev. Biol.* **30**, 503–533 (2014).

24. Bouçanova, F. & Chrast, R. Metabolic Interaction Between Schwann Cells and Axons Under Physiological and Disease Conditions. *Front. Cell. Neurosci.* **14**, 148 (2020).

25. Viader, A. *et al.* Schwann Cell Mitochondrial Metabolism Supports Long-Term Axonal Survival and Peripheral Nerve Function. *J. Neurosci.* **31**, 10128–10140 (2011).

26. Tricaud, N., Perrin-Tricaud, C., Brusés, J. L. & Rutishauser, U. Adherens Junctions in Myelinating Schwann Cells Stabilize Schmidt-Lanterman Incisures via Recruitment of p120 Catenin to E-Cadherin. *J. Neurosci.* **25**, 3259–3269 (2005).

27. Kister, A. & Kister, I. Overview of myelin, major myelin lipids, and myelin-associated proteins. *Front. Chem.* **10**, (2023).

28. Corin, K. & Bowie, J. U. How physical forces drive the process of helical membrane protein folding. *EMBO Rep.* **23**, e53025 (2022).

29. Stoffel, W. & Bosio, A. Myelin glycolipids and their functions. *Curr. Opin. Neurobiol.* **7**, 654–661 (1997).

30. Bosio, A., Binczek, E., Haupt, W. F. & Stoffel, W. Composition and Biophysical Properties of Myelin Lipid Define the Neurological Defects in Galactocerebroside- and Sulfatide-Deficient Mice. *J. Neurochem.* **70**, 308–315 (1998).

31. Siems, S. B. *et al.* Proteome profile of peripheral myelin in healthy mice and in a neuropathy model. *eLife* **9**, e51406 (2020).

32. Gillespie, C. S., Sherman, D. L., Blair, G. E. & Brophy, P. J. Periaxin, a novel protein of myelinating schwann cells with a possible role in axonal ensheathment. *Neuron* **12**, 497–508 (1994).

33. Sherman, D. L., Wu, L. M. N., Grove, M., Gillespie, C. S. & Brophy, P. J. Drp2 and periaxin form Cajal bands with dystroglycan but have distinct roles in Schwann cell growth. *J. Neurosci. Off. J. Soc. Neurosci.* **32**, 9419–9428 (2012).

34. Yang, Y. & Shi, Y. L-periaxin interacts with S-periaxin through its PDZ domain. *Neurosci. Lett.* **609**, 23–29 (2015).

35. Patzig, J. *et al.* Quantitative and integrative proteome analysis of peripheral nerve myelin identifies novel myelin proteins and candidate neuropathy loci. *J. Neurosci. Off. J. Soc. Neurosci.* **31**, 16369–16386 (2011).

36. Quarles, R. H. Myelin-associated glycoprotein (MAG): past, present and beyond. *J. Neurochem.* **100**, 1431–1448 (2007).

37. Filbin, M. T. & Tennekoon, G. I. Homophilic adhesion of the myelin P0 protein requires glycosylation of both molecules in the homophilic pair. *J. Cell Biol.* **122**, 451–459 (1993).

38. Shapiro, Lawrence et al. Crystal structure of the extracellular domain from P0, the major structural protein of peripheral nerve myelin - PubMed. *Neuron* **17**, 435–449.

39. Dahme, M. *et al.* Disruption of the mouse L1 gene leads to malformations of the nervous system. *Nat. Genet.* **17**, 346–349 (1997).

40. Raasakka, A. & Kursula, P. How Does Protein Zero Assemble Compact Myelin? *Cells* **9**, 1832 (2020).

41. Raasakka, A. *et al.* Molecular structure and function of myelin protein P0 in membrane stacking | Scientific Reports. *Sci. Rep.* **9**, 642 (2019).

42. Wells, C. A., Saavedra, R. A., Inouye, H. & Kirschner, D. A. Myelin P0-glycoprotein: predicted structure and interactions of extracellular domain. *J. Neurochem.* **61**, 1987–1995 (1993).

43. Voshol, H., van Zuylen, C. W., Orberger, G., Vliegenthart, J. F. & Schachner, M. Structure of the HNK-1 carbohydrate epitope on bovine peripheral myelin glycoprotein P0. *J. Biol. Chem.* **271**, 22957–22960 (1996).

44. Okamoto, Y. & Takashima, H. The Current State of Charcot–Marie–Tooth Disease Treatment. *Genes* **14**, 1391 (2023).

45. Plotkowski, M. L. *et al.* Transmembrane Domain of Myelin Protein Zero Can Form Dimers: Possible Implications for Myelin Construction. *Biochemistry* **46**, 12164–12173 (2007).

46. Bizzozero, O. A., Fridal, K. & Pastuszyn, A. Identification of the palmitoylation site in rat myelin P0 glycoprotein. *J. Neurochem.* **62**, 1163–1171 (1994).

47. Bharadwaj, M. & Bizzozero, O. A. Myelin P0 glycoprotein and a synthetic peptide containing the palmitoylation site are both autoacylated. *J. Neurochem.* **65**, 1805–1815 (1995).

48. Gao, Y., Li, W. & Filbin, M. T. Acylation of myelin Po protein is required for adhesion. *J. Neurosci. Res.* **60**, 704–713 (2000).

49. Hilmi, S., Fournier, M., Valeins, H., Gandar, J. C. & Bonnet, J. Myelin P0 glycoprotein: identification of the site phosphorylated in vitro and in vivo by endogenous protein kinases. *J. Neurochem.* **64**, 902–907 (1995).

50. Xu, W. *et al.* Mutations in the cytoplasmic domain of P0 reveal a role for PKC-mediated phosphorylation in adhesion and myelination. *J. Cell Biol.* **155**, 439–446 (2001).

51. Gaboreanu, A.-M. *et al.* Myelin protein zero/P0 phosphorylation and function require an adaptor protein linking it to RACK1 and PKCα. *J. Cell Biol.* **177**, 707–716 (2007).

52. Grandis, M. *et al.* Different cellular and molecular mechanisms for early and late-onset myelin protein zero mutations. *Hum. Mol. Genet.* **17**, 1877–1889 (2008).

53. Yamaguchi, Y. *et al.* L-MPZ, a novel isoform of myelin P0, is produced by stop codon readthrough. *J. Biol. Chem.* **287**, 17765–17776 (2012).

54. Raasakka, A. & Kursula, P. How Does Protein Zero Assemble Compact Myelin? *Cells* **9**, 1832 (2020).

55. Sakakura, M., Tanabe, M., Mori, M., Takahashi, H. & Mio, K. Structural bases for the Charcot-Marie-Tooth disease induced by single amino acid substitutions of myelin protein zero. *Struct. Lond. Engl. 1993* **31**, 1452-1462.e4 (2023).

56. Ptak, C. P. *et al.* Homomeric interactions of the MPZ Ig domain and their relation to Charcot-Marie-Tooth disease. *Brain J. Neurol.* **146**, 5110–5123 (2023).

57. Wrabetz, L. *et al.* Different intracellular pathomechanisms produce diverse Myelin Protein Zero neuropathies in transgenic mice. *J. Neurosci. Off. J. Soc. Neurosci.* **26**, 2358–2368 (2006).

58. Auer-Grumbach, M., Strasser-Fuchs, S., Robl, T., Windpassinger, C. & Wagner, K. Late onset Charcot-Marie-Tooth 2 syndrome caused by two novel mutations in the MPZ gene. *Neurology* **61**, 1435–1437 (2003).

59. Inouye, H., Tsuruta, H., Sedzik, J., Uyemura, K. & Kirschner, D. A. Tetrameric assembly of full-sequence protein zero myelin glycoprotein by synchrotron x-ray scattering. *Biophys. J.* **76**, 423–437 (1999).

60. Krokengen, O. C. *et al.* On the synergy between myelin proteins P0, MBP, and P2 in peripheral nerve major dense line formation. *Febs J.* **292**, 3960–3985 (2025).

61. Pashkova, N. *et al.* PMP22 associates with MPZ via their transmembrane domains and disrupting this interaction causes a loss-of-function phenotype similar to hereditary neuropathy associated with liability to pressure palsies (HNPP). *BioRxiv Prepr. Serv. Biol.* 2023.12.24.573255 (2023) doi:10.1101/2023.12.24.573255.

62. Giese, K. P., Martini, R., Lemke, G., Soriano, P. & Schachner, M. Mouse P0 gene disruption leads to hypomyelination, abnormal expression of recognition molecules, and degeneration of myelin and axons. *Cell* **71**, 565–576 (1992).

63. Wrabetz, L. *et al.* P(0) glycoprotein overexpression causes congenital hypomyelination of peripheral nerves. *J. Cell Biol.* **148**, 1021–1034 (2000).

64. Charcot-Marie-Tooth Hereditary Neuropathy Overview - GeneReviews® - NCBI Bookshelf. https://www.ncbi.nlm.nih.gov/books/NBK1358/.

65. Nagappa, M., Sharma, S. & Taly, A. B. Charcot-Marie-Tooth Disease. in *StatPearls* (StatPearls Publishing, Treasure Island (FL), 2025).

66. Fridman, V. *et al.* CMT subtypes and disease burden in patients enrolled in the Inherited Neuropathies Consortium natural history study: a cross-sectional analysis. *J. Neurol. Neurosurg. Psychiatry* **86**, 873–878 (2015).

67. Hoebeke, C. *et al.* Retrospective study of 75 children with peripheral inherited neuropathy: Genotype-phenotype correlations. *Arch. Pediatr. Organe Off. Soc. Francaise Pediatr.* **25**, 452–458 (2018).

68. Stojkovic, T. Hereditary neuropathies: An update. *Rev. Neurol. (Paris)* **172**, 775–778 (2016).

69. Bird, T. D. Charcot-Marie-Tooth Hereditary Neuropathy Overview. in *GeneReviews®* (eds Adam, M. P. et al.) (University of Washington, Seattle, Seattle (WA), 1993).

70. Timmerman, V. *et al.* The peripheral myelin protein gene PMP–22 is contained within the Charcot–Marie–Tooth disease type 1A duplication. *Nat. Genet.* **1**, 171–175 (1992).

71. Raeymaekers, P. *et al.* Duplication in chromosome 17p11.2 in Charcot-Marie-Tooth neuropathy type 1a (CMT 1a). The HMSN Collaborative Research Group. *Neuromuscul. Disord. NMD* **1**, 93–97 (1991).

72. Nelis, E., Haites, N. & Van Broeckhoven, C. Mutations in the peripheral myelin genes and associated genes in inherited peripheral neuropathies. *Hum. Mutat.* **13**, 11–28 (1999).

73. Feely, S. *et al.* MFN2 mutations cause severe phenotypes in most patients with CMT2A. *Neurology* **76**, 1690–6 (2011).

74. Li, Y.-J. *et al.* Structural insights of human mitofusin-2 into mitochondrial fusion and CMT2A onset. *Nat. Commun.* **10**, 4914 (2019).

75. Shy, M. E. *et al.* CMT1X phenotypes represent loss of GJB1 gene function. *Neurology* **68**, 849–855 (2007).

76. Qi, C. *et al.* Structures of wild-type and selected CMT1X mutant connexin 32 gap junction channels and hemichannels. *Sci. Adv.* **9**, eadh4890 (2023).

77. Szigeti, K. & Lupski, J. R. Charcot–Marie–Tooth disease. *Eur. J. Hum. Genet.* **17**, 703–710 (2009).

78. Mandich, P. *et al.* Clinical features and molecular modelling of novel MPZ mutations in demyelinating and axonal neuropathies. https://doi.org/10.1038/ejhg.2009.37 (2009) doi:10.1038/ejhg.2009.37.

79. Sanmaneechai, O. *et al.* Genotype–phenotype characteristics and baseline natural history of heritable neuropathies caused by mutations in the MPZ gene. *Brain* **138**, 3180–3192 (2015).

80. Hobbelink, S. M. R. *et al.* Dejerine–Sottas disease in childhood—Genetic and sonographic heterogeneity. *Brain Behav.* **8**, e00919 (2018).

81. McMillan, H. J. *et al.* Novel MPZ mutations and congenital hypomyelinating neuropathy. *Neuromuscul. Disord. NMD* **20**, 725–729 (2010).

82. Ravikumar, S., Devi, U., Balakrishnan, U. & Chandrasekaran, A. Diagnosis of a floppy neonate with misleading clues: unraveled as congenital hypomyelinating neuropathy. *BMJ Case Rep.* **15**, e247555 (2022).

83. Tomaselli, P. J. *et al.* Intermediate conduction velocity in two cases of Charcot−Marie−Tooth disease type 1A. *Eur. J. Neurol.* **31**, e16199 (2024).

84. Fridman, V. & Saporta, M. A. Mechanisms and Treatments in Demyelinating CMT. *Neurother. J. Am. Soc. Exp. Neurother.* **18**, 2236–2268 (2021).

85. Patzkó, Á. & Shy, M. E. Update on Charcot-Marie-Tooth Disease. *Curr. Neurol. Neurosci. Rep.* **11**, 78–88 (2011).

86. Misra, U. K., Kalita, J. & Nair, P. P. Diagnostic approach to peripheral neuropathy. *Ann. Indian Acad. Neurol.* **11**, 89–97 (2008).

87. Bai, Y., Patzko, A. & Shy, M. E. Unfolded protein response, treatment and CMT1B. *Rare Dis.* **1**, e24049 (2013).

88. Touvier, T. *et al.* Activation of XBP1s attenuates disease severity in models of proteotoxic Charcot–Marie–Tooth type 1B. *Brain* **148**, 1978–1993 (2025).

89. Malhotra, J. D. & Kaufman, R. J. Endoplasmic reticulum stress and oxidative stress: a vicious cycle or a double-edged sword? *Antioxid. Redox Signal.* **9**, 2277–2293 (2007).

90. Harding, H. P., Zhang, Y., Bertolotti, A., Zeng, H. & Ron, D. Perk is essential for translational regulation and cell survival during the unfolded protein response. *Mol. Cell* **5**, 897–904 (2000).

91. Wek, R. C. Role of eIF2α Kinases in Translational Control and Adaptation to Cellular Stress. *Cold Spring Harb. Perspect. Biol.* **10**, a032870 (2018).

92. Lu, T. *et al.* Gene regulation and DNA damage in the ageing human brain. *Nature* **429**, 883–891 (2004).

93. Baird, T. D. *et al.* Selective mRNA translation during eIF2 phosphorylation induces expression of IBTKα. *Mol. Biol. Cell* **25**, 1686–1697 (2014).

94. Adams, C. J., Kopp, M. C., Larburu, N., Nowak, P. R. & Ali, M. M. U. Structure and Molecular Mechanism of ER Stress Signaling by the Unfolded Protein Response Signal Activator IRE1. *Front. Mol. Biosci.* **6**, 11 (2019).

95. Pennuto, M. *et al.* Ablation of the UPR-mediator CHOP restores motor function and reduces demyelination in Charcot-Marie-Tooth 1B mice. *Neuron* **57**, 393–405 (2008).

96. Yoshida, K. *et al.* A key role of starburst amacrine cells in originating retinal directional selectivity and optokinetic eye movement. *Neuron* **30**, 771–780 (2001).

97. Calfon, M. *et al.* IRE1 couples endoplasmic reticulum load to secretory capacity by processing the XBP-1 mRNA. *Nature* **415**, 92–96 (2002).

98. Hetz, C. The unfolded protein response: controlling cell fate decisions under ER stress and beyond. *Nat. Rev. Mol. Cell Biol.* **13**, 89–102 (2012).

99. Ye, J. *et al.* ER stress induces cleavage of membrane-bound ATF6 by the same proteases that process SREBPs. *Mol. Cell* **6**, 1355–1364 (2000).

100. McCulloch, M. K., Mehryab, F. & Rashnonejad, A. Navigating the Landscape of CMT1B: Understanding Genetic Pathways, Disease Models, and Potential Therapeutic Approaches. *Int. J. Mol. Sci.* **25**, 9227 (2024).

101. Laurini, C. *et al.* Phenotype-Genotype Correlations in Early-Onset Myelin Protein Zero–Related Neuropathies. *Neurol. Genet.* **11**, e200314 (2025).

102. Shy, M. E. *et al.* Phenotypic clustering in MPZ mutations. *Brain* **127**, 371–384 (2004).

103. Gemignani, F. *et al.* Charcot–Marie–Tooth Disease with Myelin Protein Zero Mutation Presenting as Painful, Predominant Small-Fiber Neuropathy. *Int. J. Mol. Sci.* **25**, 1654 (2024).

104. Ghanavatinejad, F. *et al.* In silico and in vitro effects of the I30T mutation on myelin protein zero instability in the cell membrane. *Cell Biol. Int.* **44**, 671–683 (2020).

105. Brožková, D., Mazanec, R., Haberlová, J., Sakmaryová, I. & Seeman, P. Clinical and in silico evidence for and against pathogenicity of 11 new mutations in the MPZ gene. *Clin. Genet.* **78**, 81–87 (2010).

106. Xu, J.-L. *et al.* [A genotyping study of 13 cases of early-onset Charcot-Marie-Tooth disease]. *Zhongguo Dang Dai Er Ke Za Zhi Chin. J. Contemp. Pediatr.* **21**, 670–675 (2019).

107. Agrahari, A. & George Priya Doss, C. Impact of I30T and I30M substitution in MPZ gene associated with Dejerine-Sottas syndrome type B (DSSB): A molecular modeling and dynamics. *J. Theor. Biol.* **382**, 23–33 (2015).

108. Shimizu, H. *et al.* Late-onset CMT2 associated with a novel missense mutation in the cytoplasmic domain of the MPZ gene. *Clin. Neurol. Neurosurg.* **112**, 798–800 (2010).

109. Souayah, N., Seltzer, W. K., Brannagan, T. H., Chin, R. L. & Sander, H. W. Rare myelin protein zero sequence variant in late onset CMT1B. *J. Neurol. Sci.* **263**, 177–179 (2007).

110. Kilfoyle, D. H. *et al.* Myelin protein zero mutation His39Pro: hereditary motor and sensory neuropathy with variable onset, hearing loss, restless legs and multiple sclerosis. *J. Neurol. Neurosurg. Psychiatry* **77**, 963–966 (2006).

111. Choi, B.-O. *et al.* MPZ mutation in an early-onset Charcot-Marie-Tooth disease type 1B family by genome-wide linkage analysis. *Int. J. Mol. Med.* **28**, 389–396 (2011).

112. Liu, L. *et al.* Two novel MPZ mutations in Chinese CMT patients. *J. Peripher. Nerv. Syst. JPNS* **18**, 256–260 (2013).

113. Duchesne, M. *et al.* Nerve Biopsy Is Still Useful in Some Inherited Neuropathies. *J. Neuropathol. Exp. Neurol.* **77**, 88–99 (2018).

114. Vallat, J.-M. *et al.* Diagnostic value of ultrastructural nerve examination in Charcot-Marie-Tooth disease: two CMT 1B cases with pseudo-recessive inheritance. *Acta Neuropathol. (Berl.)* **113**, 443–449 (2007).

115. Bremer, J. *et al.* Myelin protein zero mutation-related hereditary neuropathies: Neuropathological insight from a new nerve biopsy cohort. *Brain Pathol.* **34**, e13200 (2024).

116. D'Urso, D., Ehrhardt, P. & Müller, H. W. Peripheral myelin protein 22 and protein zero: a novel association in peripheral nervous system myelin. *J. Neurosci. Off. J. Soc. Neurosci.* **19**, 3396–3403 (1999).

117. Hasse, B., Bosse, F., Hanenberg, H. & Müller, H. W. Peripheral myelin protein 22 kDa and protein zero: domain specific trans-interactions. *Mol. Cell. Neurosci.* **27**, 370–378 (2004).

118. Nelis, E. *et al.* Rapid screening of myelin genes in CMT1 patients by SSCP analysis: identification of new mutations and polymorphisms in the P0 gene. *Hum. Genet.* **94**, 653–657 (1994).

119. Mersiyanova, I. V. *et al.* Screening for mutations in the peripheral myelin genes PMP22, MPZ and Cx32 (GJB1) in Russian Charcot-Marie-Tooth neuropathy patients. *Hum. Mutat.* **15**, 340–347 (2000).

120. Nelis, E. *et al.* Linkage and mutation analysis in an extended family with Charcot-Marie-Tooth disease type 1B. *J. Med. Genet.* **31**, 811–815 (1994).

121. Sanfelice, D. & Temussi, P. A. Cold denaturation as a tool to measure protein stability. *Biophys. Chem.* **208**, 4–8 (2016).

122. Privalov, P. L. Cold denaturation of proteins. *Crit. Rev. Biochem. Mol. Biol.* **25**, 281–305 (1990).

123. Myers, J. K., Pace, C. N. & Scholtz, J. M. Denaturant m values and heat capacity changes: relation to changes in accessible surface areas of protein unfolding. *Protein Sci. Publ. Protein Soc.* **4**, 2138–2148 (1995).

124. Rausch, A. O. *et al.* FrustratometeR: an R-package to compute local frustration in protein structures, point mutants and MD simulations. *Bioinforma. Oxf. Engl.* **37**, 3038–3040 (2021).

125. Choi, B.-O. *et al.* MPZ mutation in an early-onset Charcot-Marie-Tooth disease type 1B family by genome-wide linkage analysis. *Int. J. Mol. Med.* **28**, 389–396 (2011).